Symmetric instability in the Atlantic Meridional Overturning Circulation

Fraser William Goldsworth

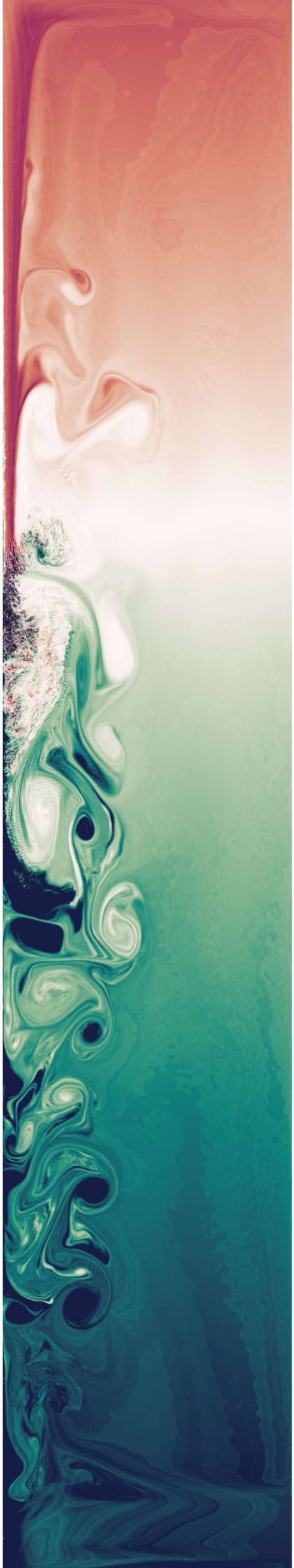
St Anne's College

University of Oxford

A thesis submitted for the degree of

Doctor of Philosophy

Trinity 2022



For potential vorticity enthusiasts everywhere.

Acknowledgements

First off I'd like to thank my wonderful supervisors, David and Helen, for all their guidance and support on my DPhil journey. No matter how busy they've been, they've always found time for me. I couldn't have asked for a better team than them.

I'd also like to thank Elizabeth Yankovsky and three anonymous reviewers for their invaluable feedback on the contents of chapters two, three & four.

For introducing me to the world of OSNAP and her help with chapter five, I'd like to say a huge thanks to Isabela Le Bras.

For taking me to sea and successfully getting me back home when the plague took hold, thanks to the RAPID AMOC team and the crew on board JC192.

Starting out, I hadn't realised the definition of symmetric instability was so contentious, so thanks to Brian Hoskins and James Maddison for reassuring me it really is as simple as $\mathsf{f}Q < 0$.

Thank you to my thesis examiners Tim Palmer and Alberto Naviera Garabato for reading over this manuscript so thoroughly, and for their thought provoking discussions and comments which helped to improve the arguments made herein.

Behind the scenes, I've been supported by some wonderful friends, so in no particular order, I'd like to say a huge thank you to Beth, Nick, Stuart and anyone else I've spent too much time in the AOPP kitchen with, the Oxford Ocean Climate group, Nilani, the Breakfast Club, Simon and the Oxford University Yacht Club, the 2018 cohort of the NERC DTP, and Lilly.

Finally, a heartfelt thanks to my family who've been my biggest supporters throughout.

I am grateful for the financial support of the Natural Environment Research Council (NE/L002612/1). Also, this work used the ARCHER2 UK National Supercomputing Service (*https://www.archer2.ac.uk*).

Abstract

The role of symmetric instability in mixing momentum, buoyancy and potential vorticity is examined in several constituent currents of the Atlantic Meridional Overturning Circulation: the North Brazil Current and its rings, the Deep Western Boundary Current in the Tropical Atlantic, and the East Greenland Current of the Sub-polar North Atlantic.

Linear stability theory predicts the structure and growth rates of overturning cells generated by symmetric instability in cross-equatorial western boundary current systems. Stratification, mixing, and curvature in the velocity field stabilise these symmetrically unstable motions. A measure of the importance of the non-traditional component of the Coriolis force in modifying symmetrically unstable motions is derived.

Idealised models of the North Brazil Current system are used to assess predictions from the linear stability analysis. They show symmetric instability is effective at neutralising negative potential vorticity originating from the Southern Hemisphere, enabling large-scale interhemispheric water exchange. Symmetric instability drives $\sim 4 \times 10^6$ m^3 s^{-1} of water mass transformation between intermediate and deep waters in this system.

Idealised models of the Deep Western Boundary Current demonstrate that symmetric instability remains an efficient mechanism for mixing potential vorticity despite dynamical differences to the North Brazil Current. Overturning cells produced by the instability generate density staircases. These provide a new diagnostic for the detection of symmetric instability.

Finally, an ensemble of idealised models of the East Greenland Current are forced with varying down front winds, which generate Ekman buoyancy fluxes. These fluxes deepen the convectively mixed layer and through the excitement of symmetric instability create a deeper low potential vorticity layer below it. This layer has potential vorticity of approximately zero and near zero stratification.

Symmetric instability is an efficient mechanism for mixing momentum, buoyancy and potential vorticity in both tropical and high-latitude components of the Atlantic's overturning circulation.

Contents

Dedication i

Acknowledgements iii

Abstract v

1 The global mixer 1

2 Symmetric instability 13

2.1 A first look at symmetric instability 14

2.1.1 Cross equatorial symmetric instability 14

2.1.2 Ekman driven symmetric instability 15

2.2 Inviscid symmetric instability of parallel shear flow 16

2.2.1 The instability criterion 20

2.2.2 Orientation of the least stable modes 21

2.2.3 Gravitational & inertial instability as limiting cases of symmetric instability 22

2.2.4 Energetics of the instability 23

2.2.5 The classical and energetic definitions of symmetric instability 24

2.3 Inviscid symmetric instability of axisymmetric flow 25

2.4 Viscous inertial and centrifugal instabilities 27

2.4.1 Viscous inertial instability of parallel shear flow 27

2.4.2 Viscous centrifugal instability of axisymmetric flow 28

2.4.3 Application to the North Brazil Current and its rings 29
2.4.4 Application to the Deep Western Boundary Current 37
2.5 Viscous symmetric instability with the complete Coriolis force 40
2.6 Symmetric instability of an ageostrophic background state 46
2.7 Summary 46

3 Symmetric instability in a cross-equatorial surface current 49
3.1 The North Brazil Current and its rings 50
3.2 Two-dimensional numerical models 53
3.2.1 Methods 53
3.2.2 Results and their relation to the linear stability analysis 56
3.3 Three-dimensional numerical models 59
3.3.1 Methods 60
3.3.2 Results & discussion 63
3.3.3 Correlations between relative and potential vorticity 72
3.3.4 Spectral energy density 75
3.3.5 Transformation of water masses 78
3.4 Summary 84

4 Symmetric instability in a cross-equatorial deep western boundary current 87
4.1 The Deep Western Boundary Current in the Tropical Atlantic 88
4.2 Model configuration 89
4.3 Symmetric instability and staircase formation 92
4.3.1 A very simple model of staircase formation 95
4.3.2 But what is generating the overturning? 96
4.3.3 Estimating at which latitudes symmetric instability occurs . . . 98
4.4 Summary 100

5 Ekman driven symmetric instability in the East Greenland Current 103

5.1 Water mass formation in the Irminger Sea 104
5.2 A two-dimensional model of the East Greenland current 108
5.3 The reference integration 109
5.4 An ensemble of model simulations 118
5.5 Open questions 124
5.5.1 Can the effect of the instability be effectively parameterised? . 124
5.5.2 How do symmetric and baroclinic instabilities interact? 125
5.6 Summary 127

6 Conclusions 131

Software & data 141

List of symbols 143

References 147

Chapter 1

The global mixer

> *The shape of the sea is always the same. Or rather it's always different, but in the same way.*
> Philip Marsden, the Silent Landscape

The Atlantic Meridional Overturning Circulation (AMOC) is a climatically important circulation that spans the entirety of the Atlantic Ocean basin. In its surface limb, it draws water from the Southern Hemisphere northward across the equator, redistributing climatically important tracers such as heat and carbon as it does so (Buckley and Marshall, 2016). At 26°N the AMOC transports around 1.25 PW of heat northward (Bryden et al., 2020), which accounts for around 25% of the meridional transport of heat by the global atmosphere and ocean at this latitude (Srokosz et al., 2012). The AMOC's contribution to poleward heat transport warms North West Europe by around 5°C (Jackson et al., 2015).

The AMOC is driven by buoyancy forcing, wind forcing, and diapycnal mixing (e.g. Munk and Wunsch, 1998; Johnson et al., 2019). In the high-latitude North Atlantic & polar seas, strong buoyancy forcing produces dense North Atlantic Deep Waters, which sink and flow southwards (e.g. Marshall and Schott, 1999). These waters are primarily formed in the Irminger and Iceland basins, and the Nordic Seas, although a small amount of formation occurs in the Labrador Sea too (Lozier

et al., 2019). The formation of deep waters in the North Atlantic is balanced by diapycnal upwelling as waters flow southwards (Munk, 1966; Ferrari et al., 2016; Mashayek et al., 2017; McDougall and Ferrari, 2017; Callies and Ferrari, 2018; Cimoli et al., 2022), and wind-driven Ekman upwelling in the Southern Ocean (Gnanadesikan, 1999; Marshall and Speer, 2012). The circulation is closed by a net northward transport of waters in the Atlantic's upper 1,000 m. Figure 1.1 shows some of the major western boundary current pathways of the AMOC, although interior and gyre circulations also contribute to the overturning.

The AMOC can be represented by a zonally integrated meridional overturning stream function in density space, defined as

$$\psi(y,\rho) = \int_{x'=x_w}^{x_e} \int_{z'=-H}^{z(x',y,\rho)} V(x',y,z')\,dz'\,dx' \ , \tag{1.1}$$

where x is the longitude, x_e and x_w are the Eastern and Western boundaries, y is the latitude, z is the vertical coordinate, H is the depth, ρ is the density and V is the meridional velocity. This naturally leads to a conceptual framework in which the AMOC is viewed as a meridionally coherent and zonally uniform "global conveyor". In recent years, it has become apparent that although this framework can be useful for understanding the zonally integrated overturning cell, its dynamics (Weijer et al., 2019), and its impacts (Little et al., 2019; Zhang et al., 2019), the framework has its limitations. In particular, this world view offers little insight when considering the smaller scale, non-uniform dynamics which generate the diapycnal mixing which is so important in maintaining the circulation, and the mesoscale and submesoscale dynamics which can strongly influence the variability of the currents which contribute to the AMOC (e.g. Thomas et al., 2013). It is now increasingly common to think of the AMOC in relation to its many constituent currents and the gyre circulations which contribute to the net-overturning (Bower et al., 2019).

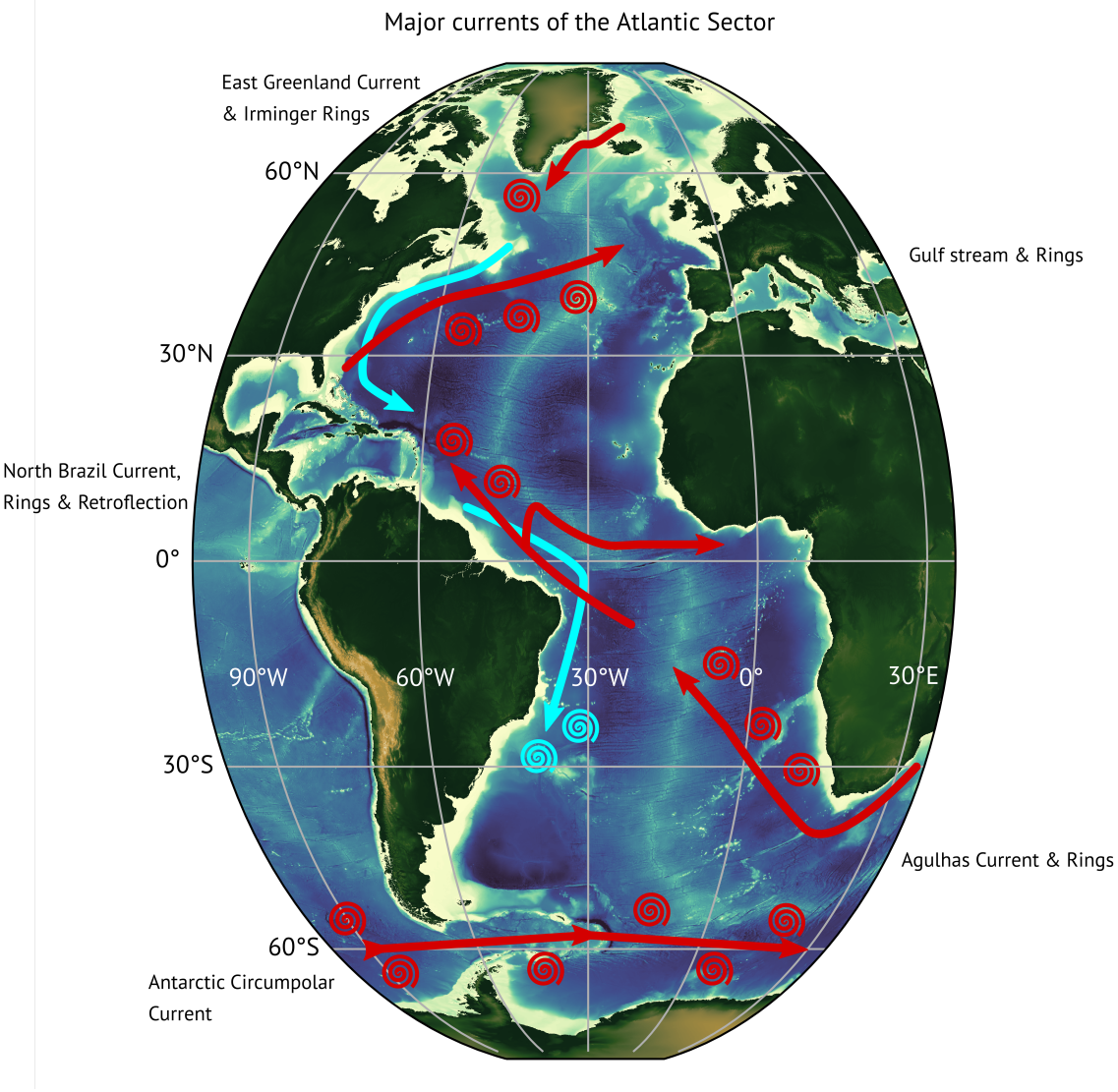


Figure 1.1: Schematic of the major current systems of the Atlantic sector. Currents shown in red are surface currents, and are labelled. Blue currents show Deep Western Boundary Current pathways of North Atlantic Deep Waters. Trajectories of currents are illustrative. Shading is GEBCO Compilation Group (2020) bathymetry data.

This thesis will investigate the role of symmetric instability, a submesoscale instability that generates overturning cells, in producing mixing — be this of buoyancy, momentum, potential vorticity or other tracers of interest — in several western boundary current systems which contribute to the AMOC. Mixing can occur either along isopycnals or across isopycnals. Along isopycnal, or "lateral", mixing is important for fluxing heat and freshwater around the ocean (Abernathey et al., 2022). In turn, freshwater fluxes are known to be an important control on the stability of the AMOC (Rahmstorf and Ganopolski, 1999; Weijer et al., 2019). Across isopycnal, or "diapycnal", mixing is important for balancing buoyancy forced deep water formation in the Sub-polar North Atlantic and Nordic Seas (Munk, 1966). Recent studies suggest diapycnal mixing may also be important in the deep water formation in the Sub-polar region too (Evans et al., 2022).

A further, contrasting, feature of submesoscale instabilities is their ability to restratify the water column (Boccaletti et al., 2007; Fox-Kemper et al., 2008; Fox-Kemper and Ferrari, 2008). Restratification can inhibit mixing and deep water formation (Gelderloos et al., 2011), meaning it isn't necessarily clear whether symmetric instability will act to increase or decrease rates of diapycnal mixing in areas it is active. On top of this the stratification of the Atlantic at the boundaries has primary impacts on meridional mass transports (e.g. Hirschi et al., 2003).

Submesoscale motions, such as those resulting from symmetric instability, are characterised by a Rossby number and a Froude number of order one — i.e. rotation, inertia and stratification are of similar importance (Thomas et al., 2008; McWilliams, 2016; Gula et al., 2022). The submesoscale dynamics of the ocean have only recently started to be explored due to the small length scales (around 100 m to 10 km) and time scales (from hours to weeks) over which they operate making observations difficult and modelling computationally expensive (Thomas et al., 2008). It has, however, become abundantly clear that submesoscale flows

and instabilities may be key in generating diapycnal mixing (Gula et al., 2022), and in cascading energy towards dissipative scales (Muller et al., 2005; Callies and Ferrari, 2013; Yu et al., 2019; Evans et al., 2020). The hyper-local nature of the submesoscale means that we are still building a picture of the spatiotemporal patterns and mechanisms of mixing generated by currents at this scale and their impact on larger-scale circulations. Understanding these mixing patterns is key to understanding how waters are transformed in the constituent currents of the AMOC (Groeskamp et al., 2019).

Due to the small scales at which symmetric instability operates, even state of the art coupled climate models are unable to adequately resolve its effects (Bachman and Taylor, 2014; Bachman et al., 2017). As such, if we want to understand the effects of the instability on the wider climate system and remove biases associated with the inadequate representation of symmetric instabilities we must turn to parameterisations. By studying the behaviour of symmetric instability in idealised models we can build a picture of whether these parameterisations are necessary and what biases they may address.

To understand symmetric instability, it is useful to first introduce the scalar quantities buoyancy and Ertel potential vorticity, the latter of which is a composite formed by combining buoyancy and momentum. Buoyancy is defined as

$$b = -\frac{g}{\rho_0}(\rho - \rho_0) \tag{1.2}$$

where g is the Earth's gravitational acceleration and ρ_0 is a reference density. Ertel potential vorticity, commonly referred to as just potential vorticity, is defined as

$$Q = (\mathbf{f} + \boldsymbol{\nabla} \times \mathbf{u}) \cdot \boldsymbol{\nabla} b \tag{1.3}$$

where $\mathbf{f}$ is the planetary vorticity vector and $\mathbf{u}$ is the velocity field in the rotating

frame of reference. Potential vorticity is materially conserved in the absence of diabatic forcing (Ertel, 1942). One can interpret the potential vorticity as either the component of absolute vorticity normal to isopycnal surfaces and scaled by the isopycnal thickness, or the stratification along a vortex tube and scaled by the absolute vorticity of the vortex, with the former being the most common way of understanding the quantity.

Symmetric instability is intimately linked to potential vorticity: a necessary but not sufficient condition for the excitement of symmetric instability is that the vertical component of planetary vorticity and the potential vorticity of a fluid have opposite signs. Mathematically we require that

$$fQ < 0\,, \tag{1.4}$$

where f is the vertical component of the planetary vorticity vector, also known as the Coriolis parameter[1]. Waters which satisfy this instability criterion are often described as having anomalous potential vorticity.

The overturning cells generated during the excitement of symmetric instability occur in a plane perpendicular to the mean flow and are oriented such that they are parallel to isopycnal surfaces — symmetric instability is often said to produce slantwise convection because of this (e.g. Emanuel, 1994). The overturning motions cause the mixing of waters with anomalous potential vorticity, moving gradients of momentum and buoyancy towards dissipative scales, and producing waters with potential vorticity of approximately zero (Taylor and Ferrari, 2009). This corresponds to the absolute vorticity vector being parallel to isopycnal surfaces.

The North Brazil Current and its rings, and the Deep Western Boundary Current

[1] This criterion is derived in section 2.2.1.

are two of the most important cross-equatorial pathways of the AMOC, accounting for around 70% of the AMOC's surface (Fratantoni et al., 2000) and two thirds of its deep (Richardson and Fratantoni, 1999; Bower et al., 2019) interhemispheric water exchange. The North Brazil Current is an intense northward flowing western boundary current, and its rings are large anticyclonic eddies spun up as a result of barotropic instability (Johns et al., 1998; Castelão and Johns, 2011). The Deep Western Boundary Current is a much slower and deeper boundary current which flows southwards (Schott et al., 2005). Both of these currents are shown schematically in figure 1.1. The role of symmetric instability in mixing anomalous potential vorticity in the North Brazil Current and the Deep Western Boundary Current systems of the Tropical Atlantic is hitherto unclear; however, we have reason to suspect it may play an important role in the region.

Away from the tropics, the planetary contribution to potential vorticity typically dominates, meaning that large-scale currents tend to be stable to symmetric instability — i.e. $fQ \geq 0$. Due to the material conservation of potential vorticity, we would expect waters in the North Brazil Current to have negative potential vorticity and in the Deep Western Boundary Current to have positive potential vorticity, since they originate away from the equator in regions where planetary vorticity will dominate the potential vorticity balance. As these currents advect waters equatorward, we would expect their potential vorticity to remain the same. At the equator itself, planetary vorticity changes sign, meaning that upon crossing the equator, the potential vorticity in these currents renders them unstable to symmetric instability. Edwards and Pedlosky (1998*a*,*b*) suggest that the modification of this anomalous potential vorticity occurs in frictional boundary layers as the currents flow poleward; however, we know that this can only be the case in models, as they employ eddy viscosities several orders of magnitude higher than that of seawater and hence exaggerate the role of friction (Akuetevi and Wirth,

2015).

We suggest an alternative hypothesis: the excitement of symmetric instability generates sufficient mixing of potential vorticity to rid cross-equatorial oceanic currents of their anomalous potential vorticity. A similar hypothesis has been made for western boundary currents in the Martian atmosphere (Joshi, 1994), whereas in the Earth's atmosphere it is thought that friction and diabatic heating are able to dissipate anomalous potential vorticity (Rodwell and Hoskins, 1995). The idea that symmetric instability may be present in oceanic cross-equatorial flows has not previously been entertained due to preconceptions about the smallness of the growth rate of symmetric instability in the vicinity of the equator (Edwards and Pedlosky, 1998*a*; Haine and Marshall, 1998). This thesis will challenge these preconceptions and demonstrate that they are misplaced.

If the excitement of symmetric instability is more efficient at neutralising anomalous potential vorticity in cross-equatorial flows than viscous processes, it is possible that cross-equatorial transport in coarse resolution ocean models (including the ocean components of coupled climate models) are suppressing or enhancing interhemispheric water exchanges. This would have wide-ranging climate impacts, impacting the strength of the AMOC in the tropics, interhemispheric heat exchange and the position of the inter-tropical convergence zone (which is key for correctly predicting rainfall patterns over Brazil and the wider South American continent), to name just a few.

The Sub-polar North Atlantic is another region of fundamental importance to the AMOC. It is here that North Atlantic Deep Waters are formed as a result of buoyancy loss (Marshall and Schott, 1999; Pickart et al., 2003; de Jong and de Steur, 2016; Lozier et al., 2019, e.g.). Observations from the Sub-polar North Atlantic suggest that symmetric instability may also be at play in the East Greenland Current (see figure 1.1) during strong wind events that occur in Winter and

Spring time (Le Bras et al., 2022). These observations raise questions regarding the amount of diapycnal mixing produced by symmetric instability (and secondary instabilities), and the role of this mixing in pre-conditioning the mixed layer such that conditions are conducive to the further formation of dense waters. This thesis will begin to answer some of the questions that observations in the region are not able to answer alone. Missing such pre-conditioning events from climate models may lead to an overly stable stratification in the region and inhibit the subsequent formation of deep waters. This could be a factor in explaining why models show such little deep water formation in the Irminger Sea when compared with observations, and would lead to systematic biases in the response of deep water formation rates (and therefore the AMOC) to atmospheric forcings.

Demonstrating the presence of symmetric instability in the North Brazil Current, Deep Western Boundary Current, and East Greenland Current systems is significant as it highlights regions where coarse-resolution ocean models and climate models may not accurately represent the mixing that is occurring in the ocean. As we have just seen, such small-scale processes are key mediators of the AMOC's dynamics, so it's clear that either resolving or parameterising them accurately is key to accurately representing the AMOC in models. Given the importance of mixing within the AMOC, perhaps it is appropriate to think of the circulation as a *global mixer* connected by along-isopycnal transports, as well as a *global conveyor* connected by mixing?

In summary, this thesis aims to answer:

- What role does symmetric instability play in the dynamics of the AMOC and its constituent currents?
- How is potential vorticity transformed in cross-equatorial western boundary currents?

The former question is broad. We will focus in particular on the aforementioned North Brazil Current, Deep Western Boundary Current and East Greenland Current systems, looking at how symmetric instability alters their potential vorticity dynamics and stratification, and its role in the formation of different water masses. The latter question is much more specific and technically encompassed by the former; however, it is a long-standing question of fundamental importance, hence we have stated it explicitly here. Without adequate potential vorticity modification in the Tropical Atlantic's western boundary current systems, large-scale interhemispheric water exchange is not possible meaning any meridional overturning cells would be confined to a single hemisphere (Csanady, 1985; Nof, 1990; Killworth, 1991; Johnson, 1993). As such explaining the potential vorticity modification mechanism is a foundational problem of AMOC science.

In chapter 2 we will take a closer look at symmetric instability and its "character". We will state several properties of the instability and go on to prove them using linear stability theory. In the latter half of the chapter, we will apply this theory to the North Brazil Current and its rings, the Deep Western Boundary Current in the Tropical Atlantic, and the East Greenland Current, in order to make predictions about the symmetric instabilities we may expect to see in them.

We will then move away from theory and towards using idealised numerical models to investigate the effect of symmetric instability in generating mixing in components of the AMOC. In chapter 3 we will focus on the North Brazil Current, and use a hierarchy of models to demonstrate the presence of symmetric instability. We will show that the excitement of the instability produces sufficient mixing to neutralise "wrong-signed" potential vorticity, which begins to address the second of our aims. We will then quantify the water mass formation and transformation rates in the model and examine the limitations of these calculations.

Next, we will look at the generation of symmetric instability in the Deep Western Boundary Current of the Tropical Atlantic (chapter 4). Symmetric instability here is generated by a similar mechanism to that which causes instability in the North Brazil Current. We will show that, again, symmetric instability is excited and we will examine the differences in the spatiotemporal characteristics of the instability relative to the North Brazil Current. We will also show that symmetric instability is capable of generating so-called "density staircases" — regions of low stratification separated by high stratification filaments. These staircases have secondary impacts on diapycnal mixing, although we will not attempt to quantify these effects here (Schmitt et al., 2005).

We will then head to the Sub-polar North Atlantic where we will look at how wind-forcing over the East Greenland Current can lead to the excitement of symmetric instability (chapter 5). We will use an ensemble of large eddy simulations to investigate how the rates of water mass formation vary with the strength and duration of the wind events. We also examine the effect of these events on the mixed layer depth. Calculations such as these could form the foundations of a simple parameterisation of symmetric instability in the region.

Concluding remarks are made, and the main findings of the thesis summarised in chapter 6.

Chapter 2

Symmetric instability

In real life there is no algebra

Audrey Horne, Twin Peaks

In this chapter, we will explore the mathematical theory that underpins the study of symmetric instability. In section 2.1, we will state some properties of symmetric instability, and consider ways in which it can be excited. We will then go on to derive some of the previously stated properties from the Boussinesq equations of motion for a fluid, starting in section 2.2, where we consider the classical problem of the stability of an inviscid, symmetric, parallel shear flow. In section 2.3 we review how the properties of symmetric instability change in an axisymmetric flow. Next, in section 2.4, we examine the special case of symmetric instability in flows free of vertical shear, performing linear stability analyses and looking at how the results apply to currents such as the North Brazil Current and its rings and the Deep Western Boundary Current. Section 2.5 examines how symmetric instability changes under the inclusion of the complete Coriolis force[1].

Sections 2.1 to 2.3 primarily review well-studied properties of symmetric instability, whereas the analysis and calculations presented in sections 2.4 and 2.5

[1] This is the component of the Coriolis force that acts on flows moving zonally and vertically as a result of the earth's rotation about its local meridional axis.

break new ground. They are based on extracts from a paper published in the Journal of Physical Oceanography which I took a leading role in authoring (Goldsworth et al., 2021).

2.1 A first look at symmetric instability

In the previous chapter we stated (without proof) that a necessary but not sufficient criterion for the excitement of symmetric instability in a flow is that its planetary vorticity and potential vorticity must have opposite signs (equation 1.4). Consider a fluid initially stable to symmetric instability (so $fQ \geq 0$). For it to become symmetrically unstable we must make the quantity fQ negative. There are two distinct ways to generate symmetric instability in such a flow: the first is to change the sign of the planetary vorticity, and the second is to change the sign of its potential vorticity. We will now explore these mechanisms in more detail.

2.1.1 Cross equatorial symmetric instability

At the equator planetary vorticity changes from being positive in the Northern Hemisphere to negative in the Southern Hemisphere. If we consider a fluid parcel originating in one hemisphere, its potential vorticity will typically match the planetary vorticity to ensure symmetric stability. We can then imagine advecting this fluid parcel across the equator. As potential vorticity is materially conserved and planetary vorticity changes sign at the equator, we would expect the symmetric instability criterion to be satisfied in the new hemisphere.

This mechanism does not involve buoyancy or momentum forcing, processes which typically must occur in either a surface boundary layer or sloping bottom boundary layer (Haine and Marshall, 1998; Wenegrat and Thomas, 2020). This means symmetric instability resulting from a change in sign of planetary vortic-

ity may occur in the ocean interior and is distinct from boundary layer symmetric instability. Several recent observational and theoretical studies have investigated the excitement of symmetric instability resulting from the cross-equatorial change in sign of planetary vorticity, notably Forryan et al. (2021); Jakoboski et al. (2022); Zhou et al. (2022). These studies have, however, focused on weak circulations in the ocean interior as opposed to vigorous western boundary currents. In western boundary currents, there is a near constant supply of waters with large magnitude anomalous potential vorticity. These equatorial western boundary currents are rich with temporally varying features, such as mesoscale eddies (Edwards and Pedlosky, 1998*a*; Dengler et al., 2004) which interact differently with symmetric instabilities depending on the flow regime.

2.1.2 Ekman driven symmetric instability

Ekman driven symmetric instability occurs when potential vorticity is made negative by winds blowing along a geostrophically balanced current (Thomas and Lee, 2005). Consider a southwards flowing current in the Northern Hemisphere that is surface intensified. In order to balance the vertical shear, thermal wind balance requires the outcropping of dense waters in the East. A northerly wind stress blowing along the current will induce a westwards Ekman transport (in the Northern Hemisphere), which will act to steepen the isopycnals (Allen and Newberger, 1996). For a current in thermal wind balance, potential vorticity is given by

$$Q = \left(f + \frac{\partial V}{\partial x}\right)\frac{\partial b}{\partial z} - \frac{1}{f}\left(\frac{\partial b}{\partial x}\right)^2 . \tag{2.1}$$

If the stratification is stable, and the planetary vorticity dominates over relative vorticity, as is typical when more than a few degrees away from the equator, then the first term in the equation will have the same sign as f. The quantity $(\partial_x b)^2$

is however positive semi-definite, so the second term will always act to make the potential vorticity more anomalous (Haine and Marshall, 1998). As the isopycnals steepen the $\partial_z b$ term decreases and the $\partial_x b$ term increases, meaning eventually, if the isopycnals become sufficiently steep the potential vorticity can become negative, rendering the flow unstable to symmetric instability (Thomas and Lee, 2005). This process is illustrated in figure 2.1.

Ekman driven symmetric instability has recently been observed in the East Greenland Current (Le Bras et al., 2022), however, the process has also been seen in a variety of other settings, such as the Labrador Sea (Straneo et al., 2002), the Mediterranean Sea (Bosse et al., 2021) and the Gulf Stream (Thomas et al., 2013). Ekman dynamics have even been found to be important in the excitement of symmetric instability in the bottom boundary layer of the Deep Western Boundary Current in the Orkney Deep (Spingys et al., 2021).

Models have been used to further investigate the interactions between Ekman dynamics and symmetric instability. Spall and Thomas (2016) look at wind-forced symmetric instability in a current similar to the East Greenland Current and find that, in conjunction with baroclinic instability, the process leads to large water mass transformations. Yankovsky and Legg (2019) examine how bottom boundary layer Ekman dynamics in Arctic Ocean overflows lead to the excitement of symmetric instability, and Wenegrat and Thomas (2020) look at the excitement of symmetric instability in bottom boundary layers during Ekman adjustment.

2.2 Inviscid symmetric instability of parallel shear flow

In this section, we will derive some classical results concerning the properties of symmetric instability, by considering the stability of an inviscid parallel shear flow on an f-plane. In subsequent sections, we will build on this analysis and investigate

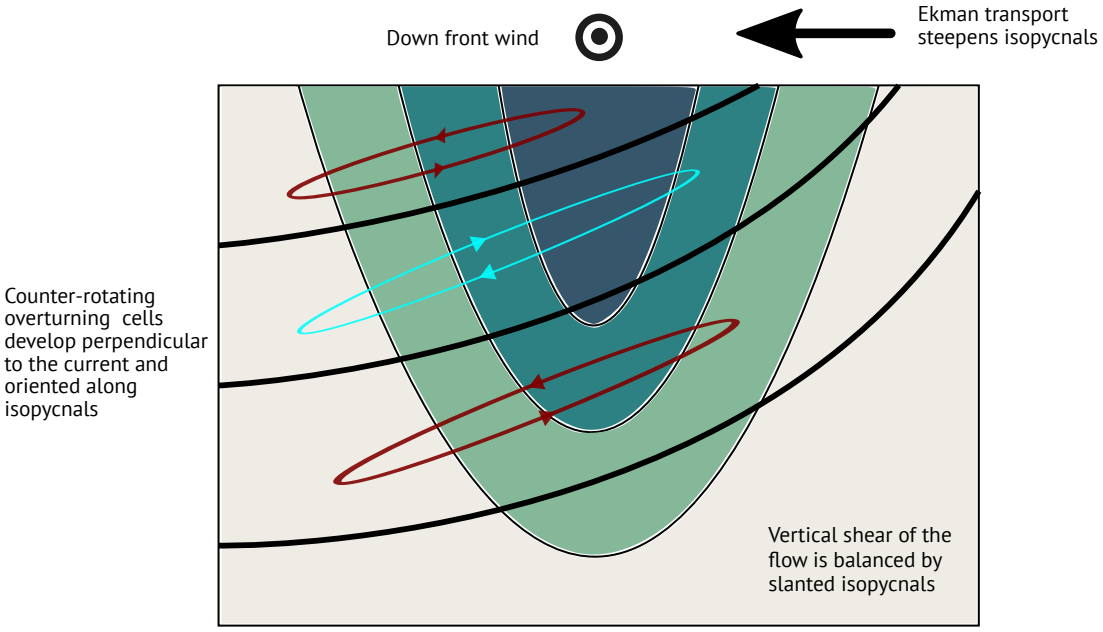


Figure 2.1: Diagram of Ekman induced symmetric instability in the Northern Hemisphere. Filled contours show a surface intensified current flowing out of the page. Thick black contours show isopycnals that balance the vertical shear of the flow. Down front winds blowing out of the page lead to Ekman transport of isopycnal outcrops towards the shore. If the isopycnals become sufficiently steep, the potential vorticity will become negative leading to the excitement of symmetric instability. This produces stacked, counter-rotating overturning cells oriented along isopycnals, shown here in red and blue. Kelvin Helmholtz instability can develop at the interfaces between isopycnals, leading to diapycnal mixing.

how these properties change in both more and less realistic scenarios.

The Boussinesq equations of motion for a meridionally symmetric[2], inviscid flow on an f-plane are

$$\frac{Du}{Dt} - fv - \frac{\partial P}{\partial x} = 0\,, \tag{2.2a}$$

$$\frac{Dv}{Dt} + fu = 0\,, \tag{2.2b}$$

$$\frac{Dw}{Dt} - \frac{\partial P}{\partial z} - b = 0\,, \tag{2.2c}$$

$$\frac{\partial u}{\partial x} + \frac{\partial w}{\partial z} = 0\,, \tag{2.2d}$$

and

$$\frac{Db}{Dt} = 0\,. \tag{2.2e}$$

Here, u, v & w are the zonal, meridional & vertical components of velocity, f is the Coriolis parameter, P is the geopotential pressure and b is the buoyancy.

We now consider a flow which is, initially, purely meridional, with $(u, v, w) = (0, V, 0)$, $P = \Pi$ and $b = B$. The flow is steady and in both geostrophic and hydrostatic balance. Mathematically

$$fV = \frac{\partial \Pi}{\partial x}\,, \tag{2.3a}$$

$$B = \frac{\partial \Pi}{\partial z}\,, \tag{2.3b}$$

$$\frac{\partial B}{\partial z} = N^2\,, \tag{2.3c}$$

and

$$\frac{\partial B}{\partial x} = M^2\,. \tag{2.3d}$$

We can then perturb this balanced flow, giving perturbed variables $(u, v, w) = (u', V + v', w')$, $P = \Pi + \Pi'$ and $b = B + b'$. Substituting these values into the

[2] A meridionally symmetric flow is invariant in the meridional direction, so all terms in ∂_y in its equations of motion will go to zero.

equations of motion and considering terms only of linear order or lower in the perturbed variables, we find that

$$\frac{\partial u'}{\partial t} - fv' + \frac{\partial \Pi'}{\partial x} = 0\,, \tag{2.4a}$$

$$\frac{\partial v'}{\partial t} + u'\frac{\partial V}{\partial x} + w'\frac{\partial V}{\partial z} + fu' = 0\,, \tag{2.4b}$$

$$\frac{\partial w'}{\partial t} + \frac{\partial \Pi'}{\partial z} - b' = 0\,, \tag{2.4c}$$

$$\frac{\partial b'}{\partial t} + w'\frac{\partial B}{\partial z} + u'\frac{\partial B}{\partial x} = 0\,, \tag{2.4d}$$

and

$$\frac{\partial u'}{\partial x} + \frac{\partial w'}{\partial z} = 0\,. \tag{2.4e}$$

From equation (2.4e) we see that we can write u' and w' in terms of an overturning stream-function ψ, where $u' = -\partial_z \psi$ and $w' = \partial_x \psi$. We will now aim to obtain an equation of motion for the overturning stream function. The first step is to differentiate the zonal and vertical momentum equations (equations 2.4a and 2.4c) with respect to the vertical and zonal coordinates, respectively. Subtracting the two equations, differentiating with respect to time, and substituting in our equations for $\partial_t b'$ and $\partial_t v'$ gives

$$\frac{\partial^2}{\partial t^2}\left(\frac{\partial^2}{\partial x^2} + \frac{\partial^2}{\partial z^2}\right)\psi + \left(N^2\frac{\partial^2}{\partial x^2} - 2f\frac{\partial V}{\partial z}\frac{\partial^2}{\partial x \partial z} + f\zeta\frac{\partial^2}{\partial z^2}\right)\psi = 0\,, \tag{2.5}$$

where $\zeta = f + \partial_x V$ is the absolute vorticity of the mean flow. This equation is the Hoskins-Ooyama equation (Ooyama, 1966; Hoskins, 1974), and it describes how overturning motions evolve within a parallel shear flow.

2.2.1 The instability criterion

To examine the stability of solutions to equation 2.5, Hoskins (1974) proposed a trial solution of the form

$$\psi = e^{ik(x\sin\Phi + z\cos\Phi) + i\omega t}\,, \tag{2.6}$$

where ω is the oscillatory frequency of the perturbations, k is the wave number, and ϕ is the angle the perturbation makes with the horizontal. Substituting this into equation 2.5 we find that

$$\omega^2 = \cos^2\Phi(N^2\tau^2 - 2f\partial_z V\tau + f\zeta)\,, \tag{2.7}$$

where $\tau = \tan\Phi$. If ω^2 is less than zero then the corresponding overturning mode will grow exponentially. For this to occur, the discriminant of the quadratic expression in the above must be negative, i.e. we need $N^2 f\zeta - (f\partial_z V)^2 < 0$. Note that not *all* modes will be unstable if this is the case as the growth rate still depends on the orientation of the perturbations, Φ. If, however, $N^2 f\zeta - (f\partial_z V)^2 \geq 0$ all the overturning modes will be stable. The instability criterion can be simplified somewhat by noting that as the flow under consideration is in geostrophic balance, $f\partial_z V = \partial_x B$, and so we can rewrite the instability criterion as

$$f\left[\left(f + \frac{\partial V}{\partial x}\right)\frac{\partial B}{\partial z} - \frac{\partial V}{\partial z}\frac{\partial B}{\partial x}\right] < 0\,. \tag{2.8}$$

The term in square brackets is recognisable as the Ertel potential vorticity of the background flow (Ertel, 1942) and so the classical instability criterion of

$$fQ < 0 \tag{2.9}$$

is recovered (Hoskins, 1974).

2.2.2 Orientation of the least stable modes

From equation 2.7 we can see that ω depends on the direction of the perturbation, and so there should be some value of Φ which maximises the growth rate — i.e. minimises ω^2. The maxima and minima of ω^2 can be found by differentiating equation 2.7 with respect to Φ and setting the result to zero. The extrema of ω^2 then satisfy

$$\sin\left(2\Phi + \arctan\left(-\frac{2M^2}{N^2 - f\zeta}\right)\right) = 0\,. \tag{2.10}$$

We can simplify this somewhat if we assume that $\left|N^2\right| \gg |f\zeta|$ and that $\left|N^2\right| \gg \left|M^2\right|$, to give

$$\sin\left(2(\Phi - \Phi_{iso})\right) = 0\,, \tag{2.11}$$

where Φ_{iso} is the angle the isopycnals make to the horizontal. This equation has four solutions, corresponding to Φ being either parallel or perpendicular to Φ_{iso}. By evaluating the second order derivative of equation 2.7 we can determine the character of these extrema. We find that with stable stratification, the modes parallel to the isopycnals give minima of ω^2 (so are least stable) whereas the modes perpendicular give maxima (and so are most stable). Note that the sign of the maxima and minima may be either positive or negative depending on the parameters of the flow, so these modes may be either entirely stable, entirely unstable or a mix of the two. It is from the orientation of the least stable mode that symmetric instability takes its alias of "slantwise convection" (as discussed in chapter 1). These slantwise overturning cells are shown schematically in figure 2.1.

In the presence of instability, assuming the above approximations remain valid and assuming that the stratification is stable, the fastest growing mode will be that which is parallel to isopycnals. The growth rate is independent of the magnitude of

the wave number; however, in the ocean, we typically have $|k \sin \Phi_{iso}| \ll |k \cos \Phi_{iso}|$ and so the fastest growing modes will tend to have a larger horizontal length scale than in the vertical. We can further show that modes which extract kinetic energy from the mean flow at the fastest rate are those with the largest wavenumber, or equivalently, in the limit of small Φ_{iso}, modes with the smallest vertical extent. This is in no way contradictory to the findings of Stone (1966), who considers the structure of symmetric instability in a vertically bounded domain, and finds modes with infinitesimal horizontal length scales dominate. In his study, he neglects that the fastest growing modes are oriented along isopycnals. As such his findings apply to situations where isopycnals are near vertical, such as within the mixed layer of the ocean.

2.2.3 Gravitational & inertial instability as limiting cases of symmetric instability

Xu and Clark (1985) explore in detail how, under appropriate coordinate transformations, the equations describing the evolution of symmetric instability are mathematically similar to those describing either inertial instability or gravitational instability (an idea first proposed in Hoskins (1974)). This leads to a useful corollary, that symmetric instability is in many ways a hybrid of gravitational and inertial instability (e.g. Haine and Marshall, 1998). To understand this we can perform a simple thought experiment.

Consider a flow, which is free of vertical shear, and therefore has horizontal isopycnals. In this scenario, we have maxima and minima in ω^2 for perturbations which are either purely horizontal or purely vertical. Evaluating ω^2 we find that the two vertical modes correspond to oscillations (or exponentially growing modes if the stratification is unstable) at the Brunt-Väisälä frequency — this corresponds to gravitational instability. The two horizontal modes correspond to either inertial

oscillations or the excitement of inertial instability (depending on the sign of $f\zeta$).

In the limit of weakly sloping isopycnals, symmetric instability becomes equivalent to inertial instability occurring along isopycnals. Another (and slightly less intuitive) interpretation is that it is equivalent to gravitational instability along iso-lines of absolute vorticity. Both these interpretations can be traced back to the interpretation of potential vorticity as being proportional to either the absolute vorticity normal to an isopycnal surface or the stratification along absolute vorticity iso-lines.

2.2.4 Energetics of the instability

The rate of change of the kinetic energy of the perturbed velocity field is given by

$$\frac{\partial E_k}{\partial t} = \frac{1}{2}\frac{\partial}{\partial t}(u'^2 + v'^2 + w'^2)\,. \tag{2.12}$$

Substituting in equations 2.4a to 2.4c, we can show that this gives

$$\frac{\partial E_k}{\partial t} = -v'(\mathbf{u}' \cdot \boldsymbol{\nabla})V - (\mathbf{u}' \cdot \boldsymbol{\nabla})\Pi' + w'b' \tag{2.13}$$

The first term on the right-hand side gives the shear production. It corresponds to a transfer of energy from the shear of the mean flow to the turbulent. The term is often split into a "geostrophic" and "lateral" shear production term (Haine and Marshall, 1998; Thomas et al., 2013; Grisouard, 2018). Typically, the excitement of symmetric instability leads to the excitement of overturning cells oriented along isopycnals, with a horizontal length scale much greater than the vertical. If the turbulent motion is along isopycnals then this term can be thought to be extracting energy from the along isopycnal shear of the mean flow.

The second term on the right-hand side is the turbulent pressure work term.

Using incompressibility of the turbulent flow we can show that

$$-(\mathbf{u}' \cdot \boldsymbol{\nabla})\Pi' = -\boldsymbol{\nabla} \cdot (\mathbf{u}'\Pi') \,. \tag{2.14}$$

This leads to the interpretation of the pressure work term as being a flux. Due to the no normal flow boundary condition, we know this flux must be zero at the boundaries, and all this term does is flux turbulent kinetic energy around the domain, rather than increase the total turbulent kinetic energy.

The final term in equation 2.12 is the turbulent buoyancy flux and corresponds to the turbulent flow extracting gravitational potential energy from the advection of buoyancy anomalies.

2.2.5 The classical and energetic definitions of symmetric instability

In the preceding section, we have chosen to implicitly define symmetric instability as the overturning instability that occurs when the potential vorticity of a flow has the opposite sign to its planetary vorticity. This is the *classical* definition of symmetric instability, as proposed by Hoskins (1974). Under this definition, gravitational and inertial instability are both special cases of symmetric instability (Xu and Clark, 1985).

This isn't, however, the only definition of symmetric instability. Thomas et al. (2013) propose a fine-grained taxonomic system, in which different instabilities can be distinguished by their energy source and the source of their anomalous potential vorticity. They define symmetric instability as getting its energy from the geostrophic shear of the mean flow, inertial instability as getting its energy from the lateral shear of the mean flow and gravitational instability as getting its energy from buoyancy fluxes. Under these definitions, we can have any of pure inertial, hybrid inertial symmetric, pure symmetric, hybrid symmetric gravitational, and

pure gravitational instabilities. We refer to this as the *energetic* definition of symmetric instabilities.

In this thesis, we adopt the classical definition. This is a purely aesthetic choice — we enjoy the simplicity of the definition and how it preserves the link between symmetric instability, pure gravitational and pure inertial instabilities, potential vorticity, and the extraction of turbulent kinetic energy from along isopycnal shear.

2.3 Inviscid symmetric instability of axisymmetric flow

A parallel shear flow in geostrophic balance is a good first-order approximation of a western boundary current's velocity structure. Such current systems, however, are often unstable to a myriad of other instabilities and the "background" flow is rarely as simple as a parallel shear flow. In the North Brazil Current, for instance, we see the spinning up of the North Brazil Current rings — huge anticyclonic eddies resulting from barotropic instability — a few degrees North of the equator (Edwards and Pedlosky, 1998*b*; Castelão and Johns, 2011). With this in mind, we will now examine how symmetric instability changes when the background flow is that of an eddy rather than that of a western boundary current.

To first-order, we can think of eddies as axisymmetric vortices in cyclogeostrophic balance (Castelão and Johns, 2011; Cruz-Gómez and Salcedo-Castro, 2013). The natural coordinate system for such a flow is cylindrical polar, and we can assume symmetry along the azimuthal direction. It is possible to write the Boussinesq equations of motion for such a flow and linearise them with respect to axisymmetric perturbations. We can then manipulate the equations in order to find an analogue of the Hoskins-Ooyama equation (equation 2.5) for an axisymmetric flow. The resulting equation, however, is nowhere near as elegant or concise as the original, due to the considerably more complex form of ∇ in cylindrical polar coordi-

nates and the presence of centrifugal forces — as such, we will not attempt to derive it here. Thankfully, the revised instability condition, as derived in appendix of A of Buckingham et al. (2021*a*), *is* just as elegant, and is given by

$$\left(f + \frac{2V_\phi}{r}\right) Q < 0\,, \tag{2.15}$$

where V_ϕ is the azimuthal velocity of the flow and r is the radial coordinate. Consider now an anticyclone, meaning the term $2V_\phi/r$ (often called the curvature term) has opposite sign to f. If the anticyclone is sufficiently strong, then planetary vorticity will be overwhelmed by the vorticity of the vortex. This means that anticyclonic flows with potential vorticity opposite in sign to the planetary vorticity can still be stable to symmetric instability. Thus, we see that anticyclonic vortices are more robust to symmetric instability than the classical instability criterion suggests.

To see this more clearly we can analyse the dispersion relation, given by

$$\omega^2 = \cos^2\Phi\left(N^2\tau^2 - 2M^2\tau + \left(f + \frac{2V_\phi}{r}\right)\zeta\right). \tag{2.16}$$

We can see that this is identical to equation 2.7 which gives the dispersion relation for the case of a parallel shear flow, but with the Coriolis parameter f replaced by $f' = f + 2\,V_\phi/r$. Assuming anticyclonic relative vorticity, the curvature term will always act to increase ω^2 and so have a stabilising effect on the flow. Conversely, a cyclonic eddy with potential vorticity of the same sign as its planetary vorticity may be symmetrically unstable if f' has a different sign to f. This leads to an asymmetry in the stability of cyclonic and anticyclonic vortices, which is discussed further in section 2.4.3.1.

A common model for an eddy is that of the Rankine vortex, in which the eddy core is assumed to be in solid body rotation, and is surrounded by an irrotational

outer shell. If we consider an anticyclonic eddy, then f' will be more negative in the core than in the outer shell, meaning we expect waters within an anticyclonic eddy core to be more stable to symmetric instability than those in the outer regions.

2.4 Viscous inertial and centrifugal instabilities

2.4.1 Viscous inertial instability of parallel shear flow

We have seen how equation 2.5 describes the evolution of symmetric instability in an inviscid parallel shear flow. However, in real currents, secondary instabilities and dissipation are present. We may then ask how symmetric instability evolves in a viscous current. Unfortunately, the shear term of equation 2.5 makes this problem very difficult to solve, especially when we consider a current in which the region of negative potential vorticity is bounded. For currents near the equator, due to the smallness of planetary vorticity, these shear terms become small and so the problem can be approximated as an inertial instability problem. We can generalise equation 2.5 to viscous flows by replacing the ∂_t operator with $\partial_t - A_r\partial^2_{zz}$, where A_r is the vertical viscosity. If we consider the inertial limit, we then find that the overturning stream function of inertially unstable motions satisfies

$$\left(\frac{\partial}{\partial t} - A_r\frac{\partial^2}{\partial z^2}\right)^2\left(\frac{\partial^2}{\partial x^2} + \frac{\partial^2}{\partial z^2}\right)\psi + \left(N^2\frac{\partial^2}{\partial x^2} + f\zeta\frac{\partial^2}{\partial z^2}\right)\psi = 0\,. \tag{2.17}$$

We can now try to find solutions to this equation of the form

$$\psi(x,z,t) = \hat{\psi}(x)e^{i(mz-\omega t)}\,. \tag{2.18}$$

Here we are assuming that the instability is bounded in the horizontal (i.e. the zonal extent of negative potential vorticity is finite) and that the vertical scale of

the current is much larger than the overturning cells which will develop. Substituting the trial solution into equation 2.17, we obtain the following boundary value problem

$$\frac{(\hat{\omega}^2 - N^2)}{m^2}\frac{d^2\hat{\psi}}{dx^2} + f\zeta\hat{\psi} = \hat{\omega}^2\hat{\psi}\,, \tag{2.19}$$

where $\hat{\omega} = \omega + iA_r m^2$. Upon appropriate non-dimensionalisation of the coordinates and variables, we find that equation 2.19 is identical to equation 4 of Plougonven and Zeitlin (2009), who identify it as a Schrödinger equation.

The eigenfunctions of the equation are $\hat{\psi}$. They define the horizontal structure of the overturning stream function. The eigenvalues of the equation are $\hat{\omega}^2$. If the eigenvalue is negative, then ω can be imaginary. If ω is imaginary, then the overturning circulation may either grow or decay exponentially. It is useful to introduce the quantity $\sigma = \mathrm{Im}(\omega)$, which, if positive, corresponds to the exponential growth rate; if negative, it gives the decay rate. The value of σ is maximised for the smallest real eigenvalue of equation 2.19. For each eigenfunction, there exists a spectrum of vertical wave numbers, each with a characteristic growth rate, or decay rate and frequency if the mode is stable[3]. The relationship between the growth rate and the vertical wave number is determined by the eigenvalue, $\hat{\omega}^2$.

2.4.2 Viscous centrifugal instability of axisymmetric flow

In the above, we have formulated a boundary value problem which describes how overturning cells develop in a viscous parallel shear flow, by neglecting the horizontal buoyancy gradient and vertical shear terms, and modifying the temporal derivative of the Hoskins-Ooyama equation (equation 2.5.) We can do the same for an axisymmetric flow by neglecting these same terms in the generalised Hoskins-

[3]Note that equation 2.19 is Hermitian. This means that its eigenvalues, $\hat{\omega}^2$, are real and that $\hat{\omega}$ will always be either purely real or purely imaginary. If $\hat{\omega}$ is imaginary then σ is also imaginary and so the mode is purely decaying or growing. If $\hat{\omega}$ is real, then the mode will have an oscillatory frequency of $\pm\hat{\omega}$ and decay exponentially over a timescale of $\tau_e = 1/A_r m^2$.

Ooyama equation of Buckingham et al. (2021*a*). This gives the axisymmetric analogue of equation 2.17 which is

$$\left(\frac{\partial}{\partial t}-A_r\frac{\partial^2}{\partial z^2}\right)^2\left(\frac{\partial^2}{\partial r^2}+\frac{1}{r}\frac{\partial}{\partial r}-\frac{1}{r^2}+\frac{\partial^2}{\partial z^2}\right)\psi+\left(N^2\left(\frac{\partial^2}{\partial r^2}+\frac{1}{r}\frac{\partial}{\partial r}-\frac{1}{r^2}\right)+f'\zeta\frac{\partial^2}{\partial z^2}\right)\psi=0\,, \tag{2.20}$$

where ψ now represents a stream-function in cylindrical polar coordinate, and has been defined as $u' = \partial_z\psi$ and $w' = -\partial_r\psi/r$. This equation describes the evolution of centrifugal instability which is the axisymmetric counterpart of inertial instability.

We will now try to find solutions of the form

$$\psi(r,z,t)=\hat{\psi}(r)e^{i(mz-\omega t)}\,. \tag{2.21}$$

Substituting this trial solution into equation 2.20 we find

$$\frac{(\hat{\omega}^2-N^2)}{m^2}\left(\frac{d^2\hat{\psi}}{dr^2}+\frac{1}{r}\frac{d\hat{\psi}}{dr}-\frac{\hat{\psi}}{r^2}\right)+f'\zeta\hat{\psi}=\hat{\omega}^2\hat{\psi}\,. \tag{2.22}$$

The eigenvalues and eigenfunctions of this equation have the same physical significance as previously discussed.

2.4.3 Application to the North Brazil Current and its rings

We will now consider a parallel shear flow similar to the North Brazil Current and an axisymmetric flow similar to the North Brazil Current rings. We will solve equations 2.19 and 2.22 for these flows and examine the structure and growth rate of the overturning cells which are generated by the inertial and centrifugal instabilities.

For the North Brazil Current, we will assume the flow looks something like a

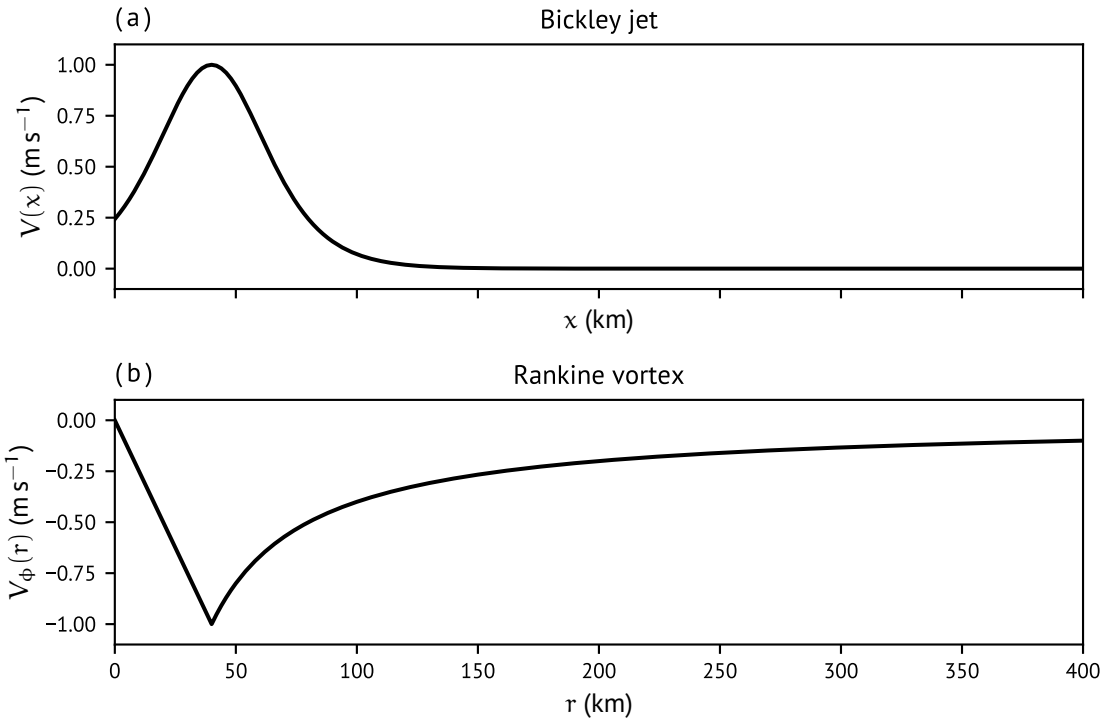


Figure 2.2: Velocity profiles of the Bickley jet and Rankine vortex used in the linear stability analyses.

Bickley jet, with the meridional velocity of the mean state given by

$$V(x) = V_0 \left(1 - \tanh^2 \left(\frac{x - x_{mid}}{\delta_b} \right) \right) \tag{2.23}$$

where V_0 is the peak velocity of the jet, x is the across stream coordinate, x_{mid} gives the distance of the peak velocity of the jet from the western boundary and δ_b is the width of the jet — this is sketched in figure 2.2a.

We will use the Rankine vortex model to represent the North Brazil Current rings. The azimuthal velocity in this model is given by

$$V_\phi(r) = \begin{cases} V_0 r / R_0 & , r < R_0 \\ V_0 R_0 / r & , r \geq R_0 \end{cases} \tag{2.24}$$

where V_0 is the velocity at the eddy's core-shell interface and R_0 is the radius of the core. This is sketched in figure 2.2b. For the Bickley jet we will use $V_0 = 1\ \mathrm{m\,s^{-1}}$, and for the Rankine vortex we will use $V_0 = -1\ \mathrm{m\,s^{-1}}$. We will set $x_{\mathrm{mid}} = 40$ km, $\delta_b = 30$ km and $R_0 = 100$ km. These values are chosen based on the observations of Johns et al. (1998) and Castelão and Johns (2011). The background stratification is set to $N^2 = 2.5 \times 10^{-5}\ \mathrm{s^{-2}}$, which is the mean buoyancy frequency at a depth of between 200 m and 400 m, as estimated from 82 neutral density profiles[4] taken by an Argo float off the coast of Brazil between January 2016 and February 2017 (Argo, 2022). The trajectory of the float and the mean neutral density profile are shown in figure 2.3. Data from a single Argo float was used as it was readily available and provides a plausible estimate of the density structure of the region.

2.4.3.1 Instability at a fixed latitude

We will first consider the properties of the eigenvalues and eigenfunctions of equations 2.19 and 2.22 at a fixed latitude of 4°N, meaning $f = 1.01 \times 10^{-5}\ \mathrm{s^{-1}}$. From the definition of $\hat{\omega}^2$, we can see that the growth rates of the instabilities (or equivalently the equations' eigenvalues) depend on the value of the vertical wavelength of the perturbations (or equivalently vertical wave-number) and the viscosity. In figure 2.4 we have plotted the growth rate of both the centrifugal and inertial instabilities as a function of vertical wavelength (λ) and the viscosity. These plots are generated by numerically solving the boundary value problem.

We see in figure 2.4 that for a given viscosity, there is a vertical wavelength which maximises the growth rate of the instabilities. As the growth is exponential, within a few e-folding timescales, the vertical mode which maximises the growth rate will dominate the structure of the instability — assuming non-linear effects

[4] A limitation of using neutral density to estimate the buoyancy frequency is that neutral density does not reliably preserve vertical buoyancy gradients (Eden and Willebrand, 1999). Here, we only really require a buoyancy frequency of the right order of magnitude, and this is unlikely to be the biggest source of errors in the subsequent calculations.

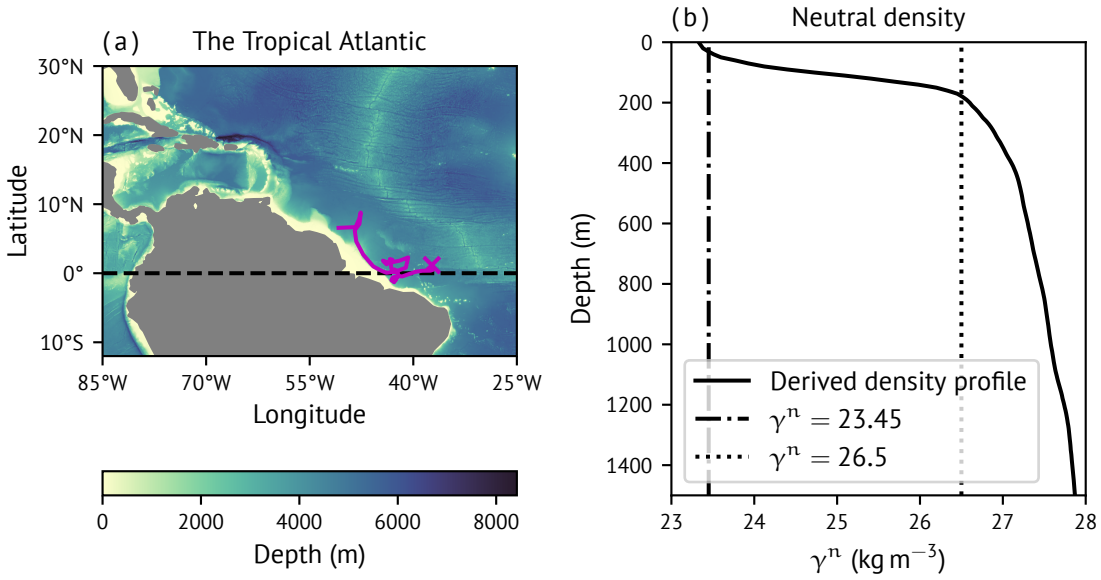


Figure 2.3: (a) Trajectory of the Argo float from which a characteristic neutral density profile for the Tropical Atlantic was obtained and (b) the mean neutral density profile, from which $\partial_z b$ was subsequently estimated.

have not taken hold before this time. Thus, although a discrete set of horizontal modes and a continuous spectrum of vertical modes may be excited, we expect only a single horizontal and vertical mode to dominate the structure of the instability.

Below a maximum 'critical' viscosity, there is a maximum and minimum vertical wavelength at which unstable modes exist; at higher viscosities, all modes are stable. The maximum wavelength is a result of stratification inhibiting vertical motions. Any mode with a wavelength smaller than the minimum will experience strong viscous damping, rendering the mode stable. The minimum vertical wavelength tends to zero in the inviscid limit. The maximum 'critical' viscosity is found when the maximum wavelength allowed by the stratification and the minimum wavelength allowed by viscosity are equal — i.e. it is related to the Ozmidov scale (Ozmidov, 1965; AMS, 2022). It has been suggested that submesoscale coherent vortices in the Tropical Atlantic (small and stable anticyclones with anomalous

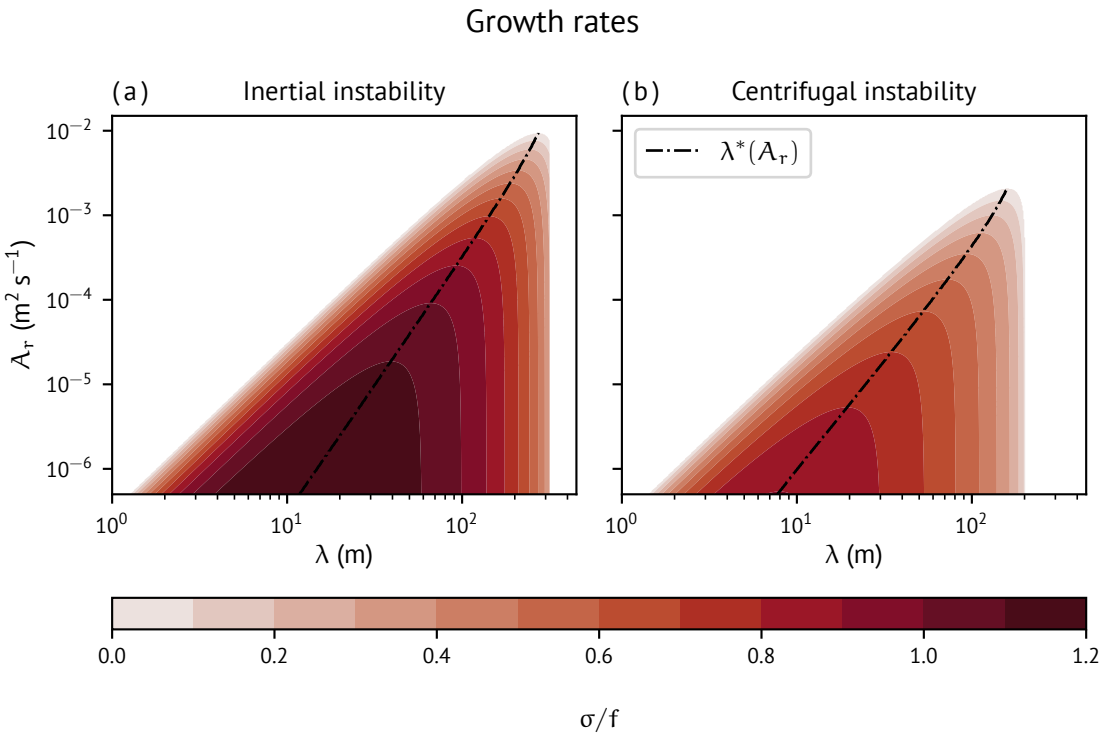


Figure 2.4: Growth rates of (a) inertial instability in a Bickley jet and (b) centrifugal instability in a Rankine vortex as a function of vertical wavelength of the mode and viscosity.

potential vorticity) are stabilised by the effects of strong stratification and dissipation (Simoes-Sousa et al., 2021). In such vortices, the stratification is so strong that overturning cells with a large vertical extent cannot exist, whereas the mixing is so strong that any overturning cells with small vertical extent will quickly dissipate. This allows the vortices to persist despite their anomalous potential vorticity. Furthermore, anticyclonic submesoscale coherent vortices experience further stabilisation resulting from their curvature. Cyclonic submesoscale coherent vortices, however, are less common as their curvature has a destabilising effect and reduces the range of parameters for which they are stable (Buckingham et al., 2021*b*). The curvature only produces an asymmetry in the prevalence of cyclonic and anticyclonic eddies at submesoscales and not at mesoscales, as the curvature term needs

to be sufficiently large to overwhelm the planetary vorticity. This typically only happens in eddies with small diameters.

It is not *a priori* clear whether the viscosity which sets properties of the instabilities is molecular or turbulent. If one is looking for signs of symmetric instability in a sufficiently coarse ocean model, then it is the turbulent viscosity that will set the vertical length scale. This makes sense as it is the only mixing process the fluid is 'aware' of. For real fluids, matters become less clear. Griffiths (2003*b*) shows that secondary Kelvin-Helmholtz instabilities form as a result of symmetric instability and play a more dominant role in the vertical scale selection than viscosity does. We suggest that when thinking about the properties of symmetric instabilities in the real ocean, it will not be the molecular viscosity which matters but the turbulent viscosity. Secondary Kelvin-Helmholtz processes are more efficient at generating mixing on a molecular scale than symmetric instability and so the rate at which anomalous potential vorticity is removed will depend on their strength as opposed to the strength of the molecular mixing generated directly by the excitement of symmetric instability.

For a given vertical viscosity we can also plot the two-dimensional structure of the overturning that the instability generates, as shown in figure 2.5. We use a viscosity of 4×10^{-4} m^2 s^{-1}, which corresponds to a typical turbulent viscosity used in high-resolution idealised models that do not resolve Kelvin-Helmholtz instabilities. For the inertial mode, the e-folding timescale is 1.4 days and the wavelength 110 m, whereas for the centrifugal mode the timescale is 3.0 days and the wavelength is 97 m. We see that both instabilities generate a stack of alternating overturning cells. Overlain in the figure is the absolute vorticity (solid line), highlighting that in the case of inertial instability the cells are strongly localized to the region of negative potential vorticity. Despite the localization, the overturning is non-zero outside the region of negative absolute vorticity. This enables the mixing

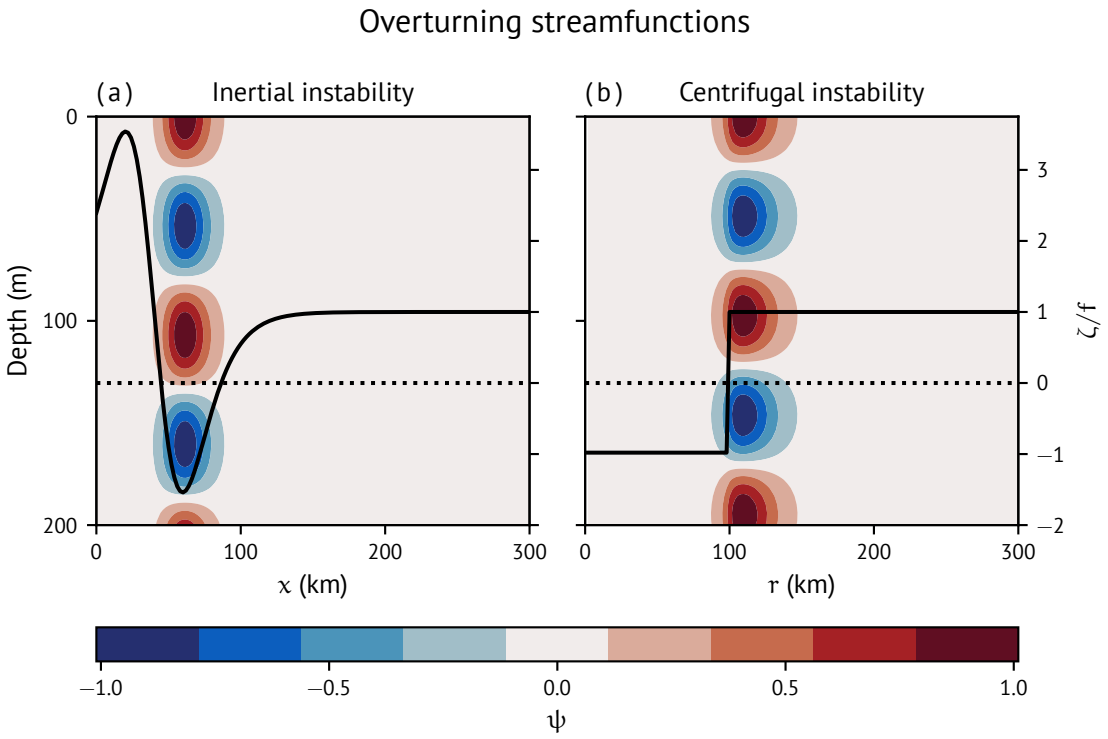


Figure 2.5: Normalised overturning stream functions generated by (a) inertial instability in a Bickley jet and (b) centrifugal instability in a Rankine vortex. Overlain is the absolute vorticity of the flows. A_r is set to 4×10^{-4} m^2 s^{-1} and $\partial_z b$ to 2.5×10^5 s^{-2}.

of waters with positive and negative potential vorticity, which over time will create a neutrally stable potential vorticity configuration.

In the case of centrifugal instability, we see that despite its negative potential vorticity, most of the eddy core is stable, and the overturning occurs mainly at the interface between the inner core and outer shell. This acts to mix waters from both within and outside the eddy core, eventually leading to a marginally stable potential vorticity configuration within the flow. We see in figure 2.4b that the range of unstable modes is slightly more limited for the anticyclonic Rankine vortex than for the Bickley jet shown in figure 2.4a. The growth rate is also smaller in the case of centrifugal instability. This reduced growth rate and the shifting of the insta-

bility away from the centre of the eddy core means the negative potential vorticity within the eddy may persist for some time.

Seawater has a viscosity of 10^{-6} m^2 s^{-1}, which puts both a lower limit on the vertical wavelength and an upper limit on the growth rate of both inertial and centrifugal instabilities for a given set of flow parameters. For the parameters used in this analysis, the e-folding timescale is 23 hours and the wavelength is 15 m for inertial instability, and for centrifugal instability, the e-folding timescale is 1.3 days and the wavelength is 10 m.

A more rigorous analysis of the solutions to the inertial instability problem described in this section is given in Plougonven and Zeitlin (2009), who consider barotropic zonal shear flows on an f-plane. On an f-plane there is no physical distinction between meridional and zonal flows so, their findings are broadly applicable, although the vorticity profiles they use differ from those considered here. There also exists a broad literature base on linear stability analyses of symmetric and inertial instabilities on a β-plane, with a focus on zonal currents (e.g. Hua et al., 1997; Griffiths, 2003*a*; Ribstein et al., 2014; Kloosterziel et al., 2017).

2.4.3.2 Instability at varying latitudes

We will now look at how the growth rates of inertial and centrifugal instability vary as a function of latitude. To do this we will solve the inertial instability and centrifugal instability boundary value problems whilst varying f, and setting the viscosity to either 10^{-6} m^2 s^{-1} or 4×10^{-4} m^2 s^{-1}. The former viscosity is chosen as it places an upper limit on the growth rate of the instabilities as a function of latitude, and the latter as it corresponds to the viscosity used in the numerical models we will present in subsequent chapters.

Figure 2.6 shows how the maximum growth rates of inertial and symmetric instability vary as a function of latitude at the two different viscosities. For both in-

ertial and centrifugal instabilities, at both high and low viscosity, the growth rate varies approximately parabolically with latitude, peaking some distance north of the equator (for a northward flowing current). The velocity profiles are unstable close to the equator; however, when we get far enough away from it, planetary vorticity starts to overwhelm the relative vorticity of the flows and so the unstable modes disappear. The centrifugal instability has a lower growth rate than the inertial instability at all latitudes, suggesting that not only are anticyclonic eddies able to maintain reserves of negative potential vorticity in their core but that the instability will grow more slowly than for a parallel shear flow.

This linear stability analysis helps explain the findings of Castelão and Johns (2011) who observe zero vorticity in North Brazil Current rings as far north as 11°N. One may expect these rings to have become symmetrically unstable much closer to the equator than this and for the marginally stable potential vorticity to have been modified by other processes by the time they reach this latitude. The above analysis, however, shows that the growth rate of the centrifugal instability is slower than that of inertial instability and that it will take a while for the instability to spread to the rings' cores given that the unstable overturning is strongest at the interface between the inner core and outer shell of the eddies.

2.4.4 Application to the Deep Western Boundary Current

We now apply the linear stability analysis to a parallel shear flow with parameters similar to the southward flowing Deep Western Boundary Current, close to the equator. We use the Bickley jet model with $V_0 = -0.2\ \mathrm{m\,s^{-1}}$, $x_{\mathrm{mid}} = 60$ km and $\delta_b = 30$ km. Let us set $f = -1.91 \times 10^{-6}\ \mathrm{s^{-1}}$ which corresponds to a latitude of 0.75°S and $N^2 = 1 \times 10^{-6}\ \mathrm{s^{-2}}$ which is a typical value for the deep ocean close to the equator (Schott et al., 1993, 2005). We choose the f of a lower latitude than before, as we suspect the slower advective timescale of the Deep Western Bound-

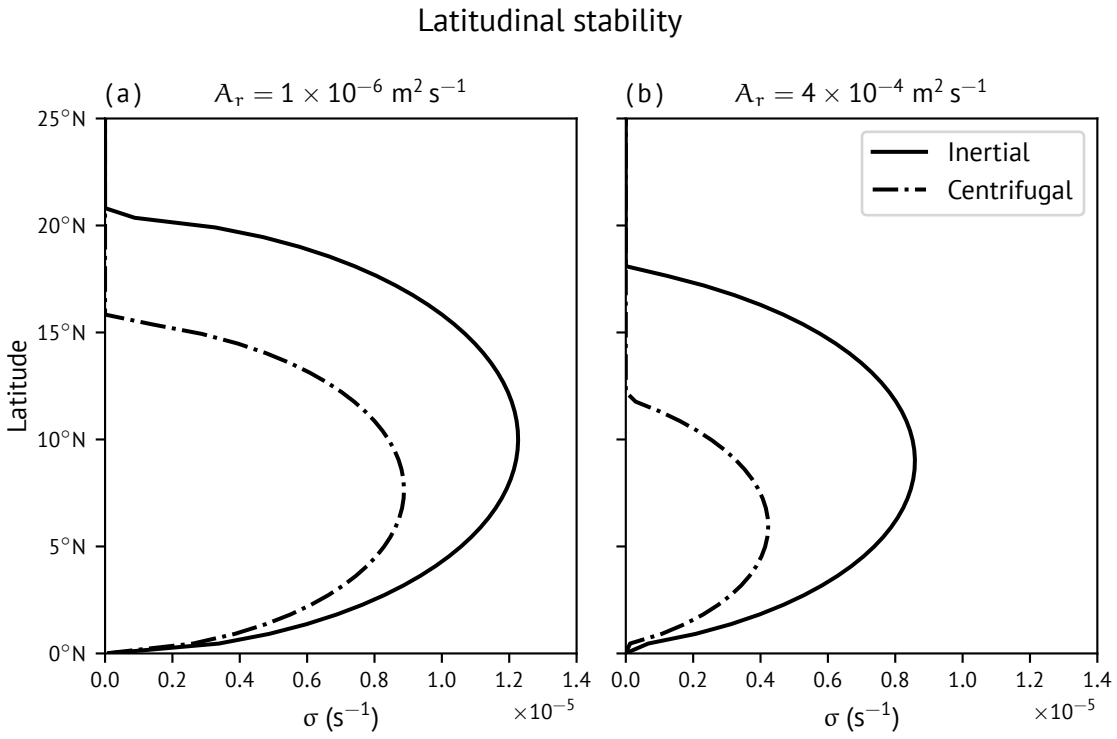


Figure 2.6: Growth rates of inertial (solid line) and centrifugal (dot-dashed line) instabilities as a function of latitude for (a) a low viscosity of $A_r = 1 \times 10^{-6}$ m^2 s^{-1} and (b) a high viscosity of 4×10^{-4} m^2 s^{-1}.

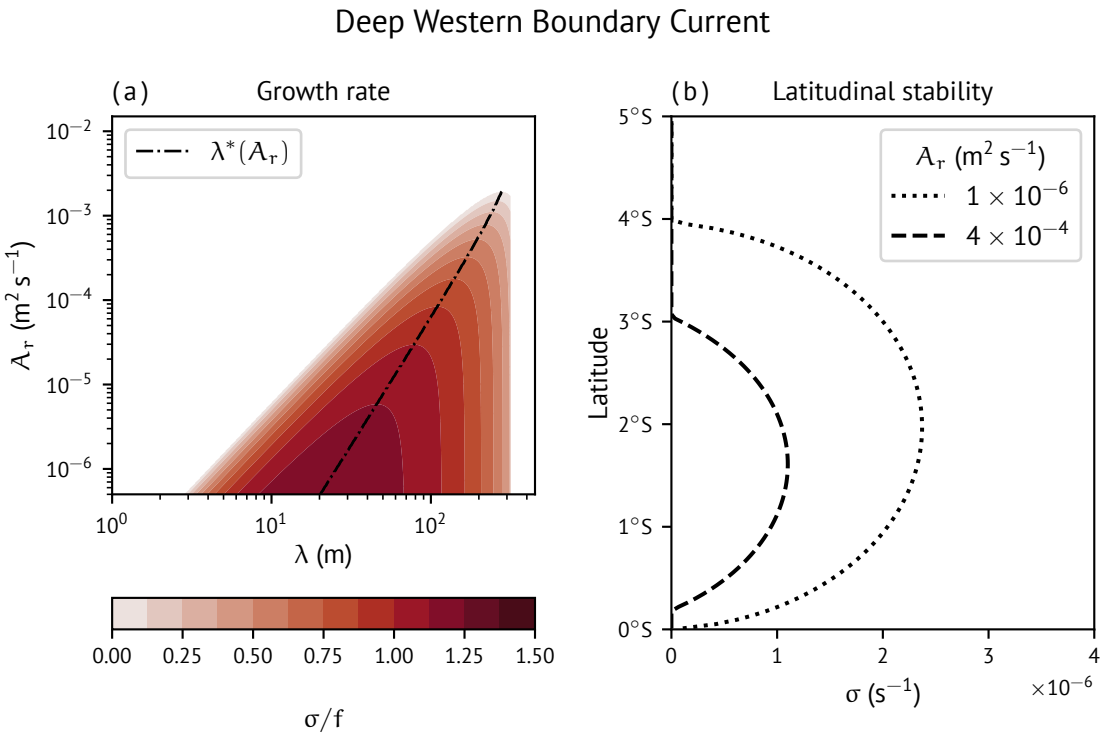


Figure 2.7: Growth rates of inertial instability (a) as a function of vertical wavelength and vertical viscosity at a fixed latitude and (b) as a function of latitude for the vertical wavelength with the largest growth rate at a fixed viscosity, for the Deep Western Boundary Current.

ary Current will mean that the instability occurs closer to the equator than in the surface currents[5].

The growth rate of inertial instability in the Deep Western Boundary Current is shown in figure 2.7a and tells much the same story as the growth rates of inertial and centrifugal instabilities in the North Brazil Current and its rings. Note, however, that for a viscosity of 4×10^{-4} m^2 s^{-1} the timescale of the instability is much longer, at 11 days, and that the size of the overturning cells is much larger at 180 m. For a viscosity of 10^{-6} m^2 s^{-1} the timescale is 5 days and the wavelength 26 m. The increased vertical length scales can be understood in terms of the reduced

[5] See section 4.3.3 for further details.

stratification, which means the vertical extent of the overturning cells is less constrained. The reduced growth rate is a combination of the reduced magnitude of f and the relative vorticity.

The growth rate of inertial instability is almost an order of magnitude smaller in the Deep Western Boundary Current than in the North Brazil Current. Furthermore, figure 2.7b show that the latitude of maximal instability is much closer to the equator and that the velocity profile ceases to be unstable much closer to the equator too. When looking for signs of symmetric instability in the Deep Western Boundary Current we will likely see it occurring much closer to the equator than it does in the North Brazil Current.

Further differences in the character of symmetric instabilities in the North Brazil Current and the Deep Western Boundary Current may be expected to arise from interactions between the current and the bottom boundary layer. We argue that these stresses are unlikely to be of leading order importance. By definition, bottom friction will only have a significant impact on the Deep Western Boundary Current within the bottom boundary layer, which typically extends around 10 m above the seabed (e.g. Weatherly and Martin, 1978). In spite of its name, the Deep Western Boundary Current is separated from the bottom boundary by around 2,000 m (Schott et al., 2005). As such bottom stresses are unlikely to have a significant impact on the dynamics, and any effects will likely be confined to the lower portion of the current.

2.5 Viscous symmetric instability with the complete Coriolis force

At the equator, the meridional component of the planetary vorticity vector is a maximum. In studies of geophysical fluid dynamics, this term is often neglected,

which we describe as making the "traditional Coriolis approximation". Conversely, retention of the meridional component of the planetary vorticity vector is described as including the "complete", "full", or "non-traditional" components of the Coriolis force (Stewart and Dellar, 2011). When treating the vertical component of the planetary vorticity as constant, we make the f-plane approximation. Close to the equator, we may also make the non-traditional f-plane approximation in which we treat the meridional component of planetary vorticity as constant instead.

Zeitlin (2018) states that "symmetric instability drastically changes upon inclusion of the full Coriolis force." The author goes on to perform a linear stability analysis of a zonally symmetric shear flow on an f-plane, taking into account the non-traditional component of the full Coriolis force. He finds that the growth rate and spatial structure of unstable modes may be significantly altered by the inclusion of the full Coriolis force. Given that on an ordinary f-plane there is no difference between a meridional and zonal flow (as the system has no preferred orientation), one may naïvely expect this finding to apply to the meridional parallel shear flows we have considered in the preceding sections; however, the inclusion of the non-traditional component of the Coriolis force breaks this meridional-zonal symmetry and reintroduces a natural meridional direction. To understand how symmetric instability in meridional flows changes under the complete Coriolis force, we must repeat the linear stability analysis of Zeitlin (2018) but for the case of a meridional flow.

The Boussinesq equations of motion for a meridionally symmetric flow on an f-plane, with the complete Coriolis force, and in the limit in which the horizontal length scale is much larger than the vertical length scale, are

$$\frac{Du}{Dt} - fv + F_{NT} w - \frac{\partial P}{\partial x} = A_r \frac{\partial^2}{\partial z^2} u\,, \tag{2.25a}$$

$$\frac{Dv}{Dt} + fu = A_r \frac{\partial^2}{\partial z^2} v\,, \tag{2.25b}$$

$$\frac{Dw}{Dt} - F_{NT} u - \frac{\partial P}{\partial z} - b = A_r \frac{\partial^2}{\partial z^2} w\,, \tag{2.25c}$$

$$\frac{\partial u}{\partial x} + \frac{\partial w}{\partial z} = 0\,, \tag{2.25d}$$

and

$$\frac{Db}{Dt} = \kappa \frac{\partial^2}{\partial z^2} b\,, \tag{2.25e}$$

where A_r is the viscosity, κ is the buoyancy diffusion coefficient and F_{NT} is the non-traditional component of the Coriolis parameter.

Similarly to section 2.2 we will now consider a flow which is, initially, purely meridional, with $(u, v, w) = (0, V, 0)$, $P = \Pi$ and $b = B$. The flow is steady, in geostrophic balance and hydrostatically balanced. Mathematically

$$fV = \frac{\partial \Pi}{\partial x}\,, \tag{2.26a}$$

$$B = \frac{\partial \Pi}{\partial z}\,, \tag{2.26b}$$

$$\frac{\partial B}{\partial z} = N^2\,, \tag{2.26c}$$

$$\frac{\partial^2 B}{\partial z^2} = 0\,. \tag{2.26d}$$

$$\frac{\partial B}{\partial x} = M^2\,, \tag{2.26e}$$

and

$$\frac{\partial^2 V}{\partial z^2} = 0\,. \tag{2.26f}$$

Again, we will perturb this balanced flow, giving perturbed variables $(u, v, w) = (u', V + v', w')$, $P = \Pi + \Pi'$ and $b = B + b'$. Substituting these values into the equations of motion and considering terms only of linear order or lower in the

perturbed variables, we find that

$$\frac{\partial u'}{\partial t'} + F_{NT} w' - f v' + \frac{\partial \Pi'}{\partial x} = 0\,, \tag{2.27a}$$

$$\frac{\partial v'}{\partial t'} + u' \frac{\partial V}{\partial x} + w' \frac{\partial V}{\partial z} + f u' = 0\,, \tag{2.27b}$$

$$\frac{\partial w'}{\partial t'} + \frac{\partial \Pi'}{\partial z} - b' - F_{NT} u' = 0\,, \tag{2.27c}$$

$$\frac{\partial b'}{\partial t} - \kappa \frac{\partial^2 b'}{\partial z^2} + w' \frac{\partial B}{\partial z} + u' \frac{\partial B}{\partial x} = 0\,, \tag{2.27d}$$

and

$$\frac{\partial u'}{\partial x} + \frac{\partial w'}{\partial z} = 0\,, \tag{2.27e}$$

where the operator $\partial/\partial t'$ is defined as

$$\frac{\partial}{\partial t'} = \frac{\partial}{\partial t} - A_r \frac{\partial^2}{\partial z^2}\,. \tag{2.28}$$

From equation 2.27e we see that we can again write u' and w' in terms of an overturning stream-function ψ, where $u' = -\partial_z \psi$ and $w' = \partial_x \psi$. We can then attempt to find an equation of motion for the stream function, analogous to equation 2.5. As before, we differentiate the zonal and vertical momentum equations (equations 2.27a and 2.27c) with respect to the vertical and zonal coordinates respectively and then subtract them, giving

$$\frac{\partial}{\partial t'}\left(\frac{\partial^2}{\partial x^2} + \frac{\partial^2}{\partial z^2}\right)\psi - f\frac{\partial v'}{\partial z} + \frac{\partial b'}{\partial x} + F_{NT}\left(\frac{\partial u'}{\partial x} + \frac{\partial w'}{\partial z}\right) = 0\,. \tag{2.29}$$

We note that the only place F_{NT} enters this equation is in the final term and that as a result of incompressibility (equation 2.27e) this term is equal to zero. Without loss of generality, we can set $\kappa = A_r$[6]. If we now differentiate the above equation

[6]This is done to simplify the notation, however, the arguments subsequently made still hold.

with respect to t' and substitute in the equations for $\partial_{t'} b'$ and $\partial_{t'} v'$ we get

$$\frac{\partial^2}{\partial t'^2}\left(\frac{\partial^2}{\partial x^2}+\frac{\partial^2}{\partial z^2}\right)\psi+\left(N^2\frac{\partial^2}{\partial x^2}-2f\frac{\partial V}{\partial z}\frac{\partial^2}{\partial x\partial z}+f\zeta\frac{\partial^2}{\partial z^2}\right)\psi=0\,, \tag{2.30}$$

which, apart from the viscous terms, is identical to equation 2.5. This has no dependence on F_{NT} at all and from this, we conclude that the complete Coriolis force does not alter symmetric instability in meridional, parallel shear flows. This finding is not in any way contradictory to the findings of Zeitlin (2018). The difference arises due to the asymmetry between the purely meridional flow considered here and the zonal flow considered in the aforementioned study.

It is, in fact, possible to make a more general statement about the types of forces which do not alter the evolution of meridional symmetric instabilities. We can modify the momentum equations (2.4a and 2.4c) with the addition of any irrotational force acting in the xz-plane and which satisfies the relationship

$$\frac{\partial \mathcal{F}_x}{\partial z}+\frac{\partial \mathcal{F}_z}{\partial x}=0\,, \tag{2.31}$$

where $\mathcal{F}_x$ and $\mathcal{F}_z$ are the zonal and meridional components of the force, respectively. Such a force is said to be irrotational. This finding can be understood in the framework of Marshall and Pillar (2011) as follows — an irrotational force is divergent and so will project onto the pressure gradient terms of the momentum equation. A rotational force is non-divergent and so projects entirely onto the acceleration term. An irrotational force (or equivalently, a divergent force) is not able to alter acceleration terms in the momentum equation. In the system described above, the inclusion of the complete Coriolis force may alter the pressure field but not the motions within the xz-plane due to its irrotational nature.

Although the crossing of the equator is a meridional phenomenon, western boundary currents, such as the North Brazil Current or the Deep Western Bound-

ary Current, will be oriented at some angle to a meridian, and so have both zonal and meridional components of velocity. In the zonal limit, symmetric instability can change drastically with the inclusion of the full Coriolis force, whereas in the meridional limit there is no change at all. For a realistic (not purely meridional) western boundary current crossing the equator, the structure of symmetric instability may therefore have some dependence on the complete Coriolis force.

The relative importance of non-traditional effects depends on the direction of the current relative to the meridional direction. For a current oriented at an angle χ to the meridional direction, the findings of Zeitlin (2018) apply but with the value of F_{NT} scaling with $\sin\chi$. Zeitlin (2018) defines a "non-traditionality" parameter and, using the findings of our work, we can generalise it to flows with a meridional component, giving

$$\Gamma = \frac{H \cot\theta \sin\chi}{L}, \tag{2.32}$$

where Γ is the "non-traditionality parameter" and θ is the latitude. Non-traditional effects are important when $\Gamma \gtrsim 1$. Close to the equator, the coast of Brazil forms an angle of $\chi \sim 60^\circ$ to the meridian. If we assume that symmetric instability in the North Brazil Current occurs at a latitude of around 4°N[7], and the current has $H \sim 100$ m and $L \sim 30$ km, we find $\Gamma \sim 0.04$. This suggests that non-traditional effects are unlikely to be hugely important in the North Brazil Current. For the Deep Western Boundary Current we expect $\theta \sim 1^\circ$N, $H \sim 1,000$ m and $L \sim 50$ km. This gives $\Gamma \sim 1$ suggesting non-traditional effects may be important here. This is likely an exaggeration of the importance of such effects though as we have taken H to be the current's vertical extent — the "correct" scale to use would be somewhere between the overturning scale size and the vertical width of the current. Finally, the East Greenland Current sits at around 60°N, forms an angle of $\chi \sim 30^\circ$ to the meridian, has $H \sim 100$ m and has $L \sim 30$ km. Due to its high latitude, we suspect

[7] This will be shown to be a reasonable prediction in section 3.3.2

non-traditional effects will be very weak, and this is reflected in a value of $\Gamma \sim 10^{-3}$.

2.6 Symmetric instability of an ageostrophic background state

If the above linear stability analyses, we have assumed the flow is in geostrophic balance. This is not always the case, for instance within a few degrees either side of the equator (Vianna and de Menezes, 2003). It is tempting to attempt a linear stability analysis under the assumption that the background flow can be split into a geostrophic and ageostrophic component such that $V = V_g + V_a$, where

$$fV_g = \frac{\partial \Pi}{\partial x}; \tag{2.33}$$

however, we will soon discover that we are unable to satisfy the requirement of a background flow that is initially steady, symmetric in the alongstream direction and not in geostrophic balance. Instead we must turn to numerical models to examine how symmetric instability manifests itself in ageostrophic currents. In the following chapter, we will do just this, with the numerical models described in section 3.2 having an ageostrophic background state, due to their proximity to the equator.

2.7 Summary

We started this chapter with a qualitative discussion of the two different ways of exciting symmetric instability — by changing the sign of either the planetary vorticity or the potential vorticity of a flow. We then went on to investigate symmetric instability more rigorously, deriving the Hoskins-Ooyama equation for a parallel

shear flow and using this to derive the classical instability criterion for symmetric instability (Ooyama, 1966; Stone, 1966; Hoskins, 1974). We then used this equation to explore some key characteristics of symmetric instability. Furthermore, we showed that symmetric instability generates overturning cells parallel to isopycnals and saw how gravitational and inertial instability can be seen as limiting cases of symmetric instability (Xu and Clark, 1985; Emanuel, 1994). We saw how the instability leads to the extraction of energy from mean flows via turbulent buoyancy fluxes and by reducing the along isopycnal shear (Haine and Marshall, 1998; Thomas et al., 2013). This led us to discuss the two different definitions of symmetric instability currently present in the literature — namely the *energetic* definition which distinguishes between lateral and geostrophic shear, and the *classical* definition which sees inertial, symmetric and gravitational instabilities as different manifestations of the same phenomena. We next looked briefly at how symmetric instability manifests itself in an axisymmetric flow, reviewing the work of Buckingham et al. (2021*a*).

Having examined these classical results, we then went on to investigate inertial instability in parallel shear flows and centrifugal instability in axisymmetric flows in the vicinity of the equator. We explored the parameter space spanned by the North Brazil Current and its rings and the Deep Western Boundary Current. We examined the structure and growth rate of the instabilities by numerically solving the boundary values problems which govern their evolution. We found instability in the North Brazil Current would have an e-folding timescale of $\mathcal{O}(1\text{ day})$ and a vertical extent of $\mathcal{O}(50\text{ m})$. In the deep western boundary current, these values rise to $\mathcal{O}(1\text{ week})$ and $\mathcal{O}(100\text{ m})$, respectively.

Finally, we looked at the effect of the complete Coriolis force on parallel shear flows near the equator. We found that meridional currents are unaffected by the force, and showed that any irrotational force will leave the dynamics of symmetric

instability unchanged. We showed that the complete Coriolis force will have almost no impact on the East Greenland Current and North Brazil Current, but its effects may become noticeable in the Deep Western Boundary Current due to the larger vertical length scale of this flow.

Chapter 3

Symmetric instability in a cross-equatorial surface current

> *When I find myself in times of trouble, Father Hoskins comes to me, saying there will be an answer, it's PV.*
> Paul McCartney

We have seen in the previous chapter how the change in sign of planetary vorticity at the equator, coupled with the conservation of potential vorticity, leads us to expect symmetric instability to be excited in cross-equatorial western boundary currents. In this chapter, we will explore results from high-resolution idealised numerical models of a surface intensified western boundary current, as an analogue of the North Brazil Current.

In section 3.1, we will describe in detail the North Brazil Current and its rings, and motivate this study. In section 3.2, we introduce a two-dimensional numerical model used to investigate how symmetric instability develops in the Tropical Atlantic, before applying a three-dimensional model to the problem in section 3.3. We use this model to estimate the amount of mixing that is induced by symmetric instability and to investigate the potential vorticity dynamics in the current. We end the chapter with a summary of our findings in section 3.4.

The content of this chapter is based on a paper published in the Journal of Physical Oceanography in which I took the lead in experimental design, implementation and authoring (Goldsworth et al., 2021).

3.1 The North Brazil Current and its rings

The tropical Atlantic contains two major western boundary current systems. At the surface, there is the North Brazil Current and its rings which flow northward and below it sits the southwards flowing Deep Western Boundary Current. The flows considered in this chapter are dynamically similar to the North Brazil Current; however, the conclusions of this work are expected to apply to cross-equatorial flows in upper-ocean western boundary currents more generally.

The North Brazil Current follows the coast of Brazil from around 10°S – 15°S to 4°N – 8°N. Here, it retroreflects and breaks up into anticyclonic eddies called the North Brazil Current rings, which continue northward to the Caribbean (Bourlès et al., 1999; Garzoli et al., 2003; Fratantoni and Richardson, 2006; Talley et al., 2011*b*). The latitude of retroflection of the North Brazil Current is set by the position of the intertropical convergence zone (Fonseca et al., 2004). The position of this region is known to depend strongly upon AMOC heat transports and varies seasonally (Zhang and Delworth, 2005; Fučkar et al., 2013). At the intertropical convergence zone, there is a zero in the wind stress curl, and this forces the North Brazil Current to cross the equator. If the wind stress curl was perfectly symmetric about the equator, there would be no gyre contribution to interhemispheric water exchange, just sufficient mass exchange to close the AMOC.

Both the North Brazil current and its rings are important pathways in the northward transport of Southern Hemisphere waters and form an important component of the AMOC (Zhang et al., 2011; Bower et al., 2019). The current has an annual

mean transport of around 32 Sv (1 Sv $\equiv 10^6$ m^3 s^{-1}) in the upper 600 m of the ocean, with typical peak velocities of around 80 cm s^{-1} and a width of approximately 100 km (Schott et al., 1993; Johns et al., 1998; Barnier et al., 2001). At the equator there is a breakdown in geostrophy due to the vanishing of the Coriolis parameter; however, at latitudes 1° either side of the equator, the current is geostrophically balanced to leading order, while the rings are in cyclogeostrophic balance (Vianna and de Menezes, 2003; Castelão and Johns, 2011). Typically, North Brazil Current rings have radii of $\sim$ 100 km and rotational velocities of $\sim$ 1 m s^{-1}, and much slower translational velocities of $\sim 10^{-2}$ m s^{-1} (Castelão and Johns, 2011). As North Brazil Current rings head northward they detach from the coast, due to the geometry of the coastline (Nof, 1996; Nof and Pichevin, 1996; Zharkov and Nof, 2010; Deremble et al., 2017).

The change in sign of the locally vertical component of planetary vorticity at the equator is an important constraint on how water can cross from one hemisphere to the other. The potential vorticity of a fluid parcel is materially conserved in the absence of mechanical and buoyancy forcing and neglecting non-linearities in the equation of state. Waters starting in the Southern Hemisphere typically have negative potential vorticity as a result of the vertical component of their planetary vorticity. Close to the equator, the planetary vorticity varies approximately linearly with latitude — the β-plane approximation. As Southern Hemisphere waters flow northward across the equator, their planetary vorticity increases and so, to conserve potential vorticity, the flow generates anti-cyclonic relative vorticity. Killworth (1991) shows that this requirement to conserve potential vorticity inhibits the penetration of fluid from one hemisphere to another, further than a few Rossby deformation radii.

In a numerical model of cross-equatorial flow, Edwards and Pedlosky (1998*a*) find an anti-cyclonic eddy field generated at the equator. They show that this field

is responsible for advecting potential vorticity, of the opposite sign to the planetary vorticity, into a viscous boundary layer where it can be dissipated. This provides a mechanism for the modification of potential vorticity, whose conservation would otherwise inhibit cross-equatorial flow. The eddy field is observed in other models of cross-equatorial flow (e.g. Jochum and Malanotte-Rizzoli, 2003; Goes et al., 2009). In a follow-up study, Edwards and Pedlosky (1998*b*) show that the eddy field is generated by barotropic instability, and is enhanced as the Rossby deformation radius is maximal at the equator (Chelton et al., 1998). It has been proposed this mechanism is behind the generation of the North Brazil Current rings (Jochum and Malanotte-Rizzoli, 2003); however, in a recent study Aguedjou et al. (2019) suggested that some other mechanism may be at play. They use satellite-derived estimates of vorticity to identify regions where necessary conditions for barotropic instability are frequently met. The dataset on which they base their analysis, however, is very coarse and so masks the fine scale vorticity structure present in the North Brazil Current system. This means their conclusions have limited applicability away from the ocean interior.

Viscous processes, like those modelled by Edwards and Pedlosky (1998*a*), can play only a limited role in the modification of potential vorticity. As such, turbulent processes in the current's interior are more likely to be of importance. These turbulent processes are of particular interest as they may lead to a short-circuiting of the AMOC through enhanced diapycnal mixing. Symmetric instability is a turbulent process that may be capable of modifying the potential vorticity in cross-equatorial flows.

3.2 Two-dimensional numerical models

The linear stability analysis of section 2.4.3 makes predictions of the growth rate of viscous symmetric instability in a meridionally symmetric, parallel shear flow situated at approximately 4°N. We will now consider a two-dimensional numerical model of a similar flow, but with vertical shear, variable stratification and finite depth. The two-dimensional nature of the flow will be retained, via the imposition of a periodic meridional boundary condition on a domain one grid cell thick. This means there is no β-effect and that equatorially enhanced barotropic instability will not occur (Edwards and Pedlosky, 1998*a*,*b*).

3.2.1 Methods

The numerical simulations are performed using the MITgcm model (Marshall et al., 1997). The model domain consists of a channel 400 km wide in the zonal direction and periodic in the meridional direction. The horizontal resolution is 2 km, and is sufficient to resolve symmetric instability (e.g. Bachman and Taylor, 2014; Brannigan et al., 2017). In the vertical there are 160 depth levels, varying in size from 6.25 m at the surface to 25 m at the bottom, giving a total depth of 1,500 m. The horizontal resolution is chosen such that the model can resolve the small-scale vorticity structure that is crucial to the excitement of symmetric instability, and the vertical resolution is chosen so that it is smaller than the expected size of the overturning cells the instability will generate.

Simulations are run on an f-plane, with $f = 1.01 \times 10^{-5}$ s^{-1}, corresponding to a latitude of 4°N, with the non-traditional component of the Coriolis force included also, taking a value of $F_{NT} = 1.45 \times 10^{-4}$ s^{-1}. A control integration is run in which the non-traditional component of the Coriolis force is neglected. A further set of integrations at 40°N and 0°N, both with and without the non-

traditional component of the Coriolis force, are performed. For the integration at 40°N, $f = 9.35 \times 10^{-5}$ s^{-1} and $F_{NT} = 1.11 \times 10^{-4}$ s^{-1}; at 0°N, $f = 0$ s^{-1} and $F_{NT} = 1.45 \times 10^{-4}$ s^{-1}. In all cases, no qualitative difference between integrations with and without the complete Coriolis force is found; this finding is unsurprising given the results presented in section 2.5.

Closure of the momentum equations is provided by an adaptive biharmonic Smagorinsky viscosity, which operates on the horizontal derivatives of momentum. This is chosen to minimize damping at the length-scales of interest (Smagorinsky, 1963; Griffies and Hallberg, 2000), with the choice inspired by its successful use in Brannigan (2016) which attempts to resolve similar submesoscale processes. A Laplacian viscosity, A_r, which operates on vertical derivatives of momentum is also used. It is set to a constant value of 4×10^{-4} m^2 s^{-1} for all integrations, apart from a viscous integration for which a value of 6×10^{-3} m^2 s^{-1} is used. The standard value is chosen to ensure the vertical structure of the symmetric instability can be adequately resolved by the model grid.

A linear equation of state is employed:

$$\rho = \rho_0 \left(1 - \alpha_T (T - T_0)\right), \tag{3.1}$$

where ρ_0 is the background density, T is temperature, T_0 is a reference temperature, and α_T is the thermal expansion coefficient. The absence of salinity means that changes in density are modulated solely by changes in temperature. The value of ρ_0 is set to 1,023.35 kg m^{-3}, α_T set to 2×10^{-4} K^{-1}, and T_0 set to 30° C. The linear equation of state is used to avoid the complexities added by non-linear effects such as cabbelling and thermobaricity (e.g. Groeskamp et al., 2016). The diffusivity of temperature is set to 1×10^{-5} m^2 s^{-1}. A second order-moment Prather advection scheme with a flux limiter is used (Prather, 1986). The initial density profile is

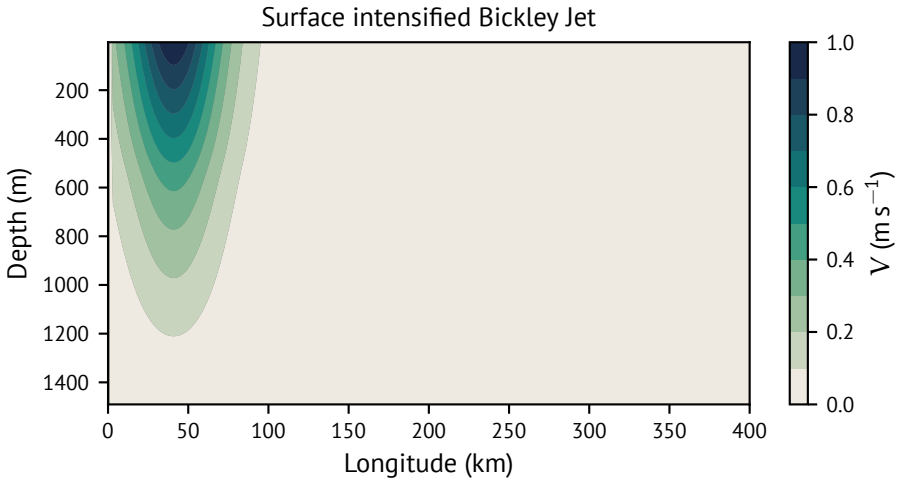


Figure 3.1: Velocity structure of the surface intensified Bickley jet with $V_0 = 1\,\mathrm{m\,s^{-1}}$, $x_{mid} = 40$ km, $\delta_b = 30$ km and $H = 1,500$ m.

based on observations taken by an Argo float in the tropical Atlantic (Argo, 2022). The neutral density profile and float trajectory are shown in figure 2.3, with the temperature profile in the model chosen to match the density profile of the aggregated observations.

The initial velocity profile is based on that of the surface intensified Bickley jet. This can be expressed as

$$V(x,z) = V_0\left(1 - \tanh^2\left(\frac{x - x_{mid}}{\delta_b}\right)\right)\frac{z+H}{H}, \tag{3.2}$$

where z is the vertical coordinate which becomes increasingly negative below the surface, and H is the absolute value of the depth. The jet parameters are set as follows: $V_0 = 1\,\mathrm{m\,s^{-1}}$, $x_{mid} = 40$ km, $\delta_b = 30$ km, $H = 1,500$ m. The profile is shown in figure 3.1. To test the sensitivity of the model to the jet's position, two control simulations were also run with x_{mid} set to either 20 km or 80 km: the resulting instability shows no qualitative dependence on the jet's position. The jet parameters are chosen to be similar to those observed in the North Brazil Current

by Johns et al. (1998). However, it should be noted that the jet described in this work is more intense ($V_{max} \sim 1\ \mathrm{m\,s^{-1}}$ rather than $\sim 0.9\ \mathrm{m\,s^{-1}}$), has less vertical shear ($\partial_z V \sim 6.6 \times 10^{-4}\ \mathrm{m^{-1}\,s^{-1}}$ rather than $\sim 3.5 \times 10^{-3}\ \mathrm{m^{-1}\,s^{-1}}$), and is deeper ($H \sim 1,500$ m rather than ~ 800 m) than that observed by Johns et al. (1998). The depth is chosen to be large, to prevent the bottom boundary layer from having too strong an influence on the evolution of any instabilities, hence the low shear and deeper current.

In the 4°N integrations, the jet prescribed is symmetrically unstable from the outset. This allows us to explore the evolution of unforced symmetric instability in a 'plausible' western boundary current. In a two-dimensional numerical model, the meridional advection of Southern Hemisphere waters with negative potential vorticity into the domain is not possible. As such we must initialise the numerical integration with waters of negative potential vorticity already in place.

At the surface boundary, a rigid lid condition is used. The lateral boundary conditions at the eastern and western edges of the domain are set to no slip. At the bottom, a free-slip boundary condition is used. The sensitivity of the simulations to the choice of boundary condition has been tested by performing model integrations with free-surface, free-slip lateral, and no-slip bottom boundary conditions: in each case, no qualitative differences in the resulting instability are observed.

3.2.2 Results and their relation to the linear stability analysis

Snapshots of potential vorticity at two-week intervals in the standard two-dimensional numerical integration are shown in figure 3.2. After around 5 days the potential vorticity distribution begins to change (not shown) and after two weeks the excitement of the instability is visible. The timescale (the inverse of the growth rate, $1/\sigma$) predicted by the linear stability analysis is ~ 2 days, which is of the right order of magnitude for what is seen here. In the leftmost panel (c), we see how the po-

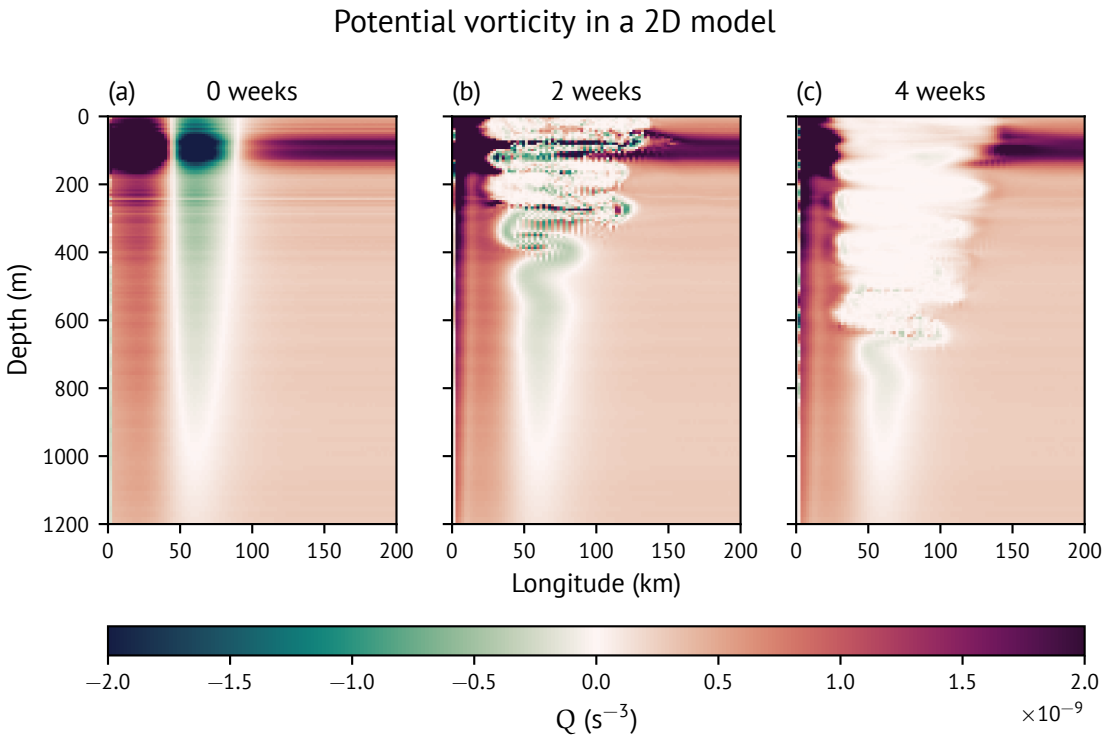


Figure 3.2: Snapshots of potential vorticity over time in the standard (no-slip) two-dimensional model. Potential vorticity is shown as a function of depth and longitude.

tential vorticity in the initially unstable region has been modified and set to a state of marginal stability — i.e. $Q = 0$. This modification of potential vorticity is driven by the overturning cells, which were predicted by the linear stability analysis. Due to the along stream symmetry, we can rearrange the equation for the conservation of potential vorticity to give

$$\frac{\partial Q}{\partial t} = \frac{\partial \psi}{\partial z}\frac{\partial Q}{\partial x} - \frac{\partial \psi}{\partial x}\frac{\partial Q}{\partial z}, \tag{3.3}$$

which explicitly links the unstable overturning generated by the instability and the redistribution of potential vorticity[1].

[1] This equation neglects the frictional dissipation of potential vorticity; however, this contribution is generally much smaller than the contribution from advection.

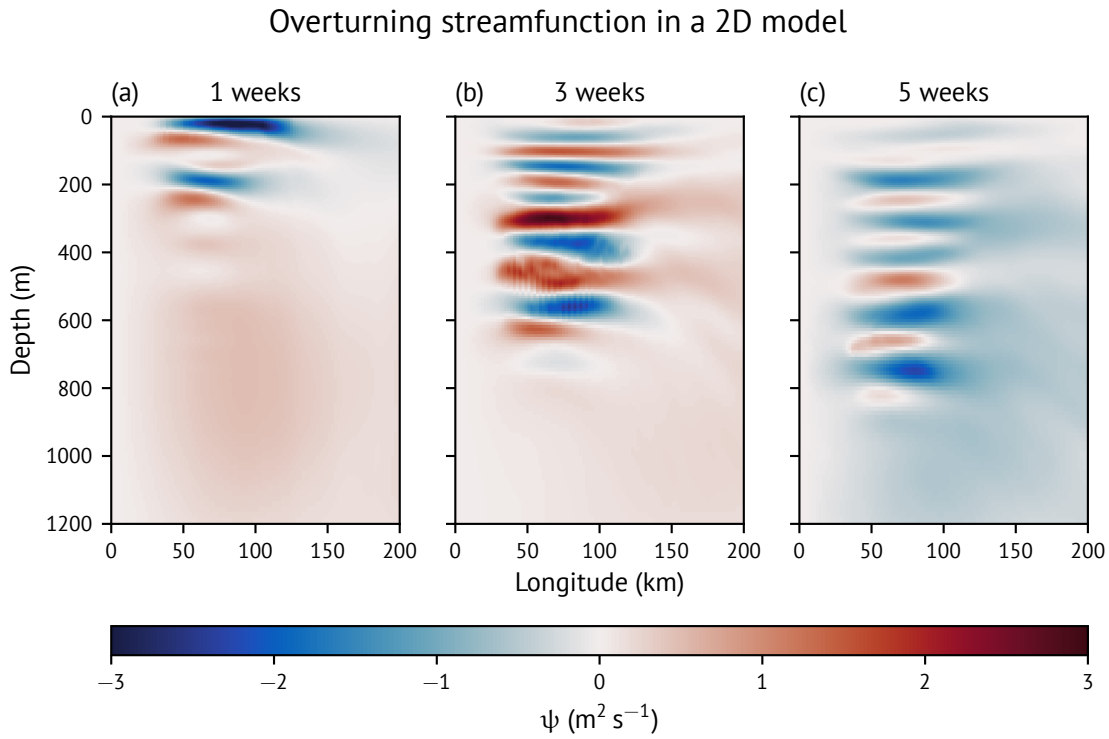


Figure 3.3: Snapshots of the zonal overturning stream-function generated by symmetric instability in the standard (no-slip) two-dimensional model. The five-day moving average of the stream function is taken to mask the effects of internal waves.

Figure 3.3 shows the zonal overturning stream-function from the standard two-dimensional numerical integration. We see structures similar to those predicted by the linear stability analysis (c.f. figure 2.5). The vertical Fourier transform of the stream function is taken at two weeks. At the longitude of the absolute vorticity minimum, there is a maximum in the power spectrum with a vertical wavelength of 100 m. This estimate of the size of the overturning cells is remarkably similar to the prediction of 105 m made by the linear stability analysis. We would expect fairly close agreement as the parameters used in the linear stability analysis are based on the jet used to initialise the model.

The resolution of the model means that secondary Kelvin-Helmholtz instabil-

ities that typically accompany the excitement of symmetric instability are absent. Furthermore, the use of an artificially high vertical viscosity, to ensure numerical stability, means the growth rate of the instability is suppressed and its vertical extent exaggerated. Although symmetric instability may look different in the ocean, the conclusion that symmetric instability is efficient at eliminating anomalous potential vorticity within a few degrees of the equator will not change — if anything the process will be more efficient due to the lower viscosity of the ocean meaning the growth rate of the instability is larger.

The linear stability analysis found that by setting the vertical viscosity to be sufficiently high, the symmetrically unstable motions can be suppressed. Integrations with a high vertical viscosity of 6×10^{-3} m^2 s^{-1} are performed and, indeed, no instability develops within them. The linear stability analysis also predicts no instability if the experiment is performed at a sufficiently high latitude, or at the equator: model integrations at 40°N and 0°N verify this is indeed the case (not shown).

3.3 Three-dimensional numerical models

Although a useful tool in understanding the processes at play in cross-equatorial flows, two-dimensional numerical models fail to capture many of their key dynamics. Perhaps the most important missing ingredients are the β-effect and meridionally asymmetric motions, both of which are suppressed by the imposition of along-stream symmetry. It is the variation and change in sign of planetary vorticity at the equator which we suspect will lead to symmetric instability. Furthermore, Edwards and Pedlosky (1998*b*) show that barotropic eddies are an important and robust feature of cross-equatorial flows. These motions cannot form if there is no meridional variation in the flow. To fully understand what is going on in

the ocean, we must relax the requirement of along-stream symmetry and turn to three-dimensional numerical models. This section describes an idealised three-dimensional model of the tropical Atlantic based on the two-dimensional model discussed previously.

3.3.1 Methods

The horizontal domain is 816 km in the zonal and 2,688 km in the meridional direction. The horizontal resolution is 2 km. The southernmost boundary is located 512 km south of the equator and the northern boundary is 2,176 km to the north. The velocity at the northern and southern boundaries is prescribed and takes the form of the surface intensified Bickley jet, as shown in figure 3.1b. The zonal velocity is initially set to zero and the meridional velocity to the same surface intensified Bickley jet prescribed at the northern and southern boundaries. As in the models previously discussed, this means the initial potential vorticity configuration is unstable to symmetric instabilities. In the Northern Hemisphere, within around 3 weeks, the majority of the negative potential vorticity initially present has been neutralized by an initial flurry of symmetric instability (in the standard viscosity runs). After this time the largest source of negative potential vorticity in the Northern Hemisphere is waters advected across the equator.

To absorb any incoming waves or eddies, there exists a sponge region within the domain, which relaxes the velocity to the Bickley jet profile prescribed at the northern and southern boundaries. The sponges stretch from 350 km south of the northern and 40 km north of the southern edges of the domain. The inverse relaxation timescale in these sponge regions varies according to a tanh function from 0 s^{-1} in the interior of the sponge to 2×10^{-5} s^{-1} at the open boundary. The sponge regions are cropped from all figures.

Unlike the two-dimensional model integrations, the three-dimensional inte-

grations evolve in qualitatively different ways depending on whether a no-slip or free-slip lateral boundary condition is imposed. The no-slip boundary condition is taken to be the standard choice, although results from free-slip integrations are also presented. A time step of 144 seconds is used for the no-slip model and 72 seconds for the free-slip model, which has a higher Reynolds number.

Integrations are performed with either a standard vertical viscosity of 4×10^{-4} $m^2\ s^{-1}$, or a high vertical viscosity of 1×10^{-2} $m^2\ s^{-1}$. The high viscosity is larger than the value of 6×10^{-3} $m^2\ s^{-1}$ used in the two-dimensional high viscosity runs. This is because the former value was insufficient to shut down the excitement of symmetric instability at high latitudes. The larger value is still not strong enough to completely shut down the excitement of symmetric instability; however, it does appreciably suppress the growth of the instability.

The β-plane approximation is made, which gives a linear latitudinal variation of planetary vorticity of 2.3×10^{-11} $m^{-1}\ s^{-1}$. The non-traditional component of the Coriolis force is also included by setting F_{NT} to a constant value[2] of 1.5×10^{-4} s^{-1}.

The same thermodynamic scheme and initial stratification are used as in the two-dimensional numerical models previously discussed. In much of the following discussion, analyses are performed at a depth of 50 m. This depth is chosen as it sits below the model's mixed layer but is still close to the surface where the excitement of symmetric instability is expected to be most vigorous.

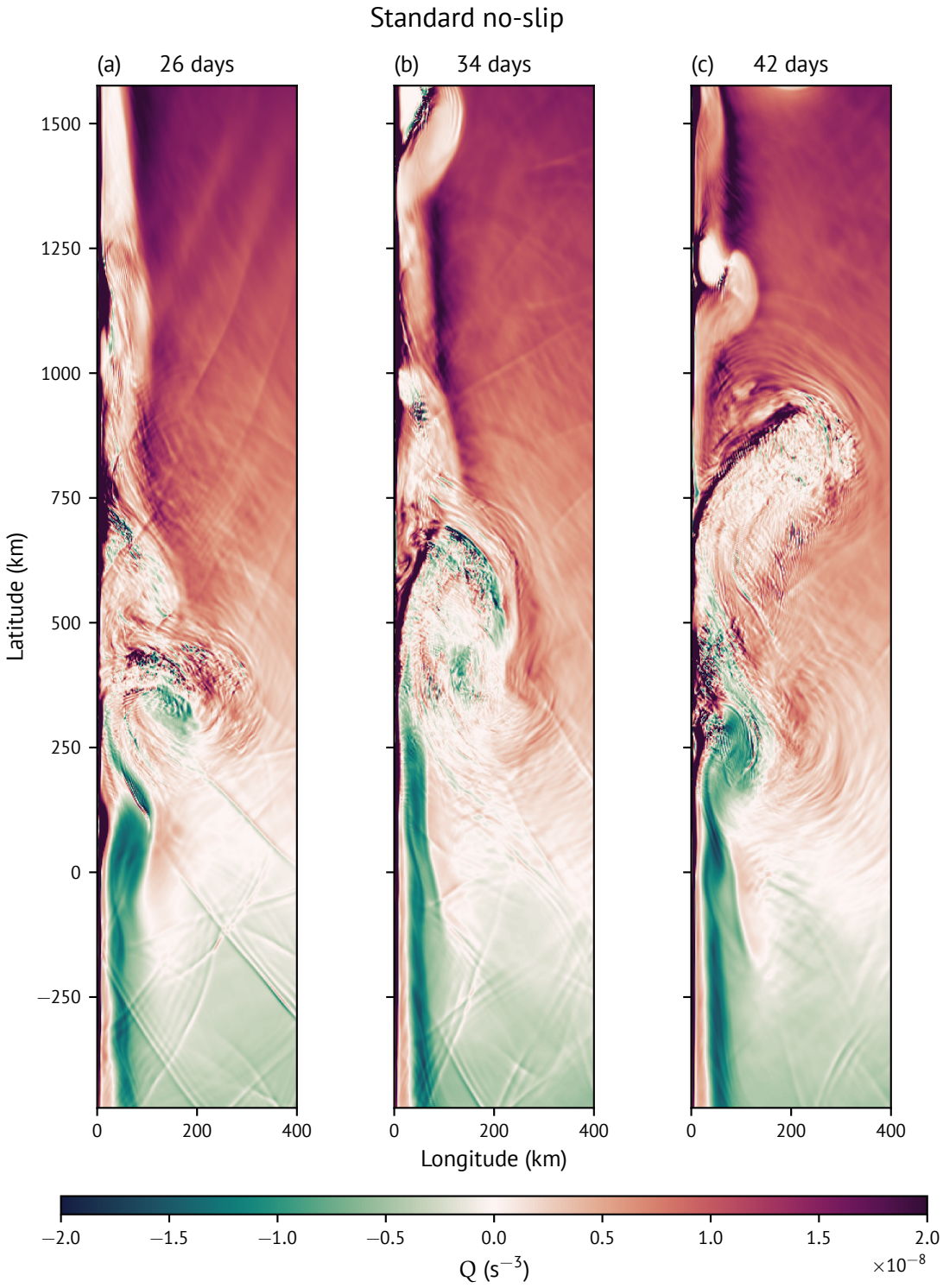


Figure 3.4: Snapshots of potential vorticity at 50 m depth for the standard (no-slip) three-dimensional model.

3.3.2 Results & discussion

3.3.2.1 No-slip lateral boundary conditions

Figure 3.4 shows snapshots of the potential vorticity field in the standard three-dimensional no-slip integration, at a depth of 50 m. Close to the equator, we see the spinning up of anticyclonic eddies of up to 200 km in diameter. The eddies are dynamically similar to those seen in other studies of cross-equatorial flow and are a result of barotropic instability (e.g. Edwards and Pedlosky, 1998*a*,*b*; Jochum and Malanotte-Rizzoli, 2003; Goes et al., 2009). Between around 250 km and 1,000 km north of the equator, smaller scale features within the eddies are visible: these arise from the excitement of symmetric instability.

There is an interesting interplay between barotropic and symmetric instabilities. We see in the Northern Hemisphere of figure 3.4a that the eddy with anticyclonic potential vorticity initially penetrates a few hundred kilometres before it begins to retroflect. Within around a week, the potential vorticity within the eddy has been reduced and it can propagate further northwards (see figure 3.4b). If we look at the submesoscale, we see features with large spatial potential vorticity gradients over short distances. This is a result of the excitement of symmetric instability which acts to redistribute potential vorticity within the eddy. By reducing its potential vorticity the eddy can propagate even further north (figure 3.4c). As the eddy moves further northwards the growth rate of symmetric instability increases and any remaining regions of negative potential vorticity become increasingly unstable. Eventually, we are left with an anticyclonic eddy with approximately neutral potential vorticity, corresponding to a state of marginal stability. The core of the eddy is one of the last regions to reach this stable state. Figure 3.5 shows a

[2] Strictly speaking, in a spherical geometry we would expect $F_{NT} = 2\Omega \cos\theta$ where θ is the latitude. At the equator, the variation in F_{NT} with latitude is minimal, and over the domain considered here, F_{NT} is constant to 2 significant figures. As such it was decided to ignore the meridional variation in F_{NT} and make the "non-traditional f-plane" approximation.

comparison of the relative and potential vorticity of an eddy which has undergone this process. We see that close to the equator regions of negative potential vorticity correspond to regions of negative relative vorticity. In a region from around 500 km to 800 km north of the equator the relationship is less clear. North of this region, the planetary vorticity is larger than the relative vorticity and contributes the most to the absolute vorticity. The excitement of symmetric instability is driving the transition from one regime to the other. South of a distance 500 km north of the equator, the relative vorticity is negative. Between 500 km and 800 km north, symmetric instability is excited. Waters leaving this region then have approximately neutral potential vorticity as a result of the excitement of symmetric instability.

The offset of this symmetrically unstable region from the equator can be understood in terms of the growth rate of the instability. Firstly, in the inviscid limit, the square of the growth rate of symmetric instability is proportional to $f(f + \xi)$, where ξ is the relative vorticity of the fluid. To first order (and in the absence of symmetric instability), changes in the planetary vorticity are approximately balanced by the relative vorticity, meaning $(f + \xi)$ is approximately constant along flow lines. This gives a growth rate that grows linearly with f and hence latitude. Close to the equator where f is small, the growth rate will be so small that other processes will dominate over symmetric instability. When a fluid parcel is advected further north, its growth rate will increase until the excitement of symmetric instability becomes apparent. At this point, symmetric instability begins to modify the potential vorticity and absolute vorticity, removing anomalous vorticity from the flow. At higher latitudes still, the source of negative potential vorticity that the instability feeds off has been largely depleted. This means we only see symmetric instability occurring within a finite latitude range.

Secondly, the fluid takes a finite time to show signs of symmetric instability. During this time the fluid will have been advected northwards away from the equa-

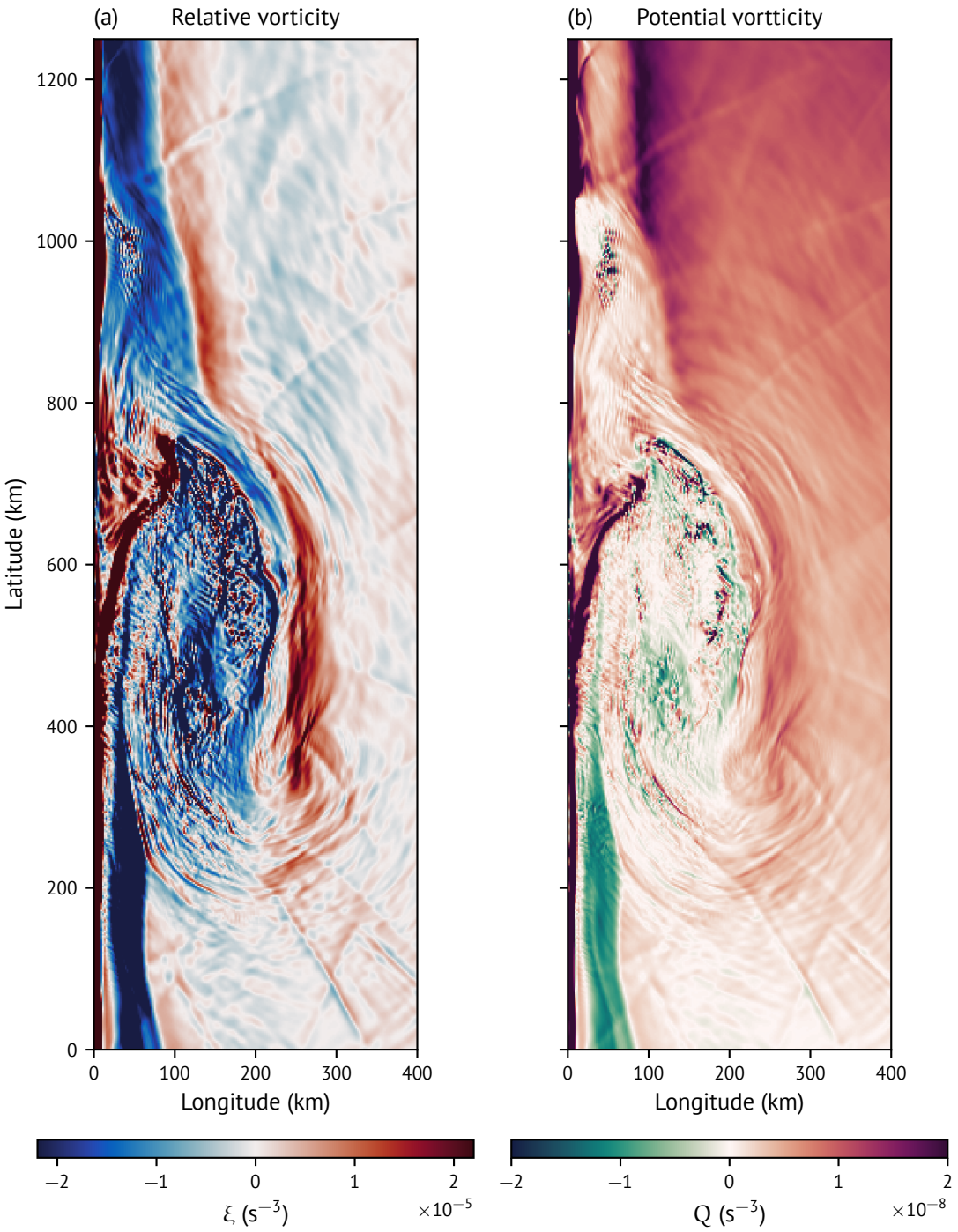


Figure 3.5: Instantaneous (a) relative vorticity and (b) potential vorticity, after 35 days of model integration at 50 m depth from the standard (no-slip) three-dimensional models.

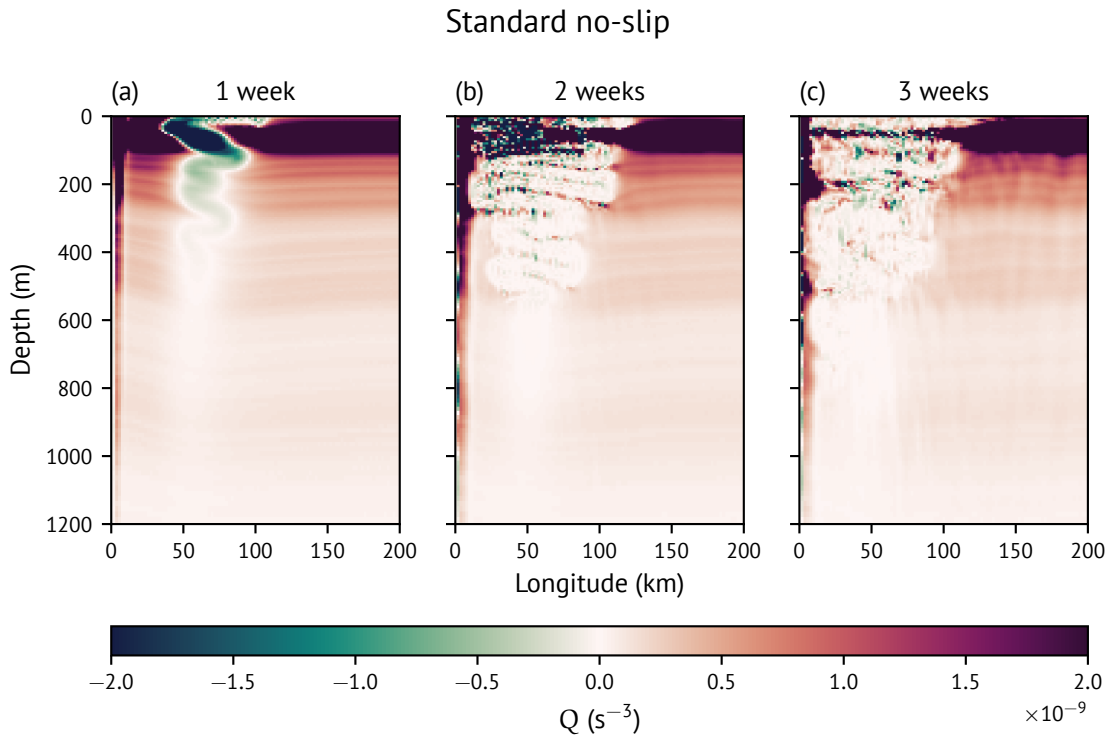


Figure 3.6: Snapshots of potential vorticity as a function of depth and longitude at 750 km North of the equator in the standard no-slip three-dimensional model.

tor. This distance, d, can be crudely estimated by $d = V\tau_e$, where V is a typical velocity of the fluid and τ_e is the timescale it takes for symmetric instability to become apparent in the flow. Taking $V \sim 80$ cm s^{-1} and $\tau_e \sim 4$ days gives $d \sim 300$ km. From this simple calculation, we shouldn't expect the instability to be well-developed either at or close to the equator.

It is interesting to look at snapshots of the potential vorticity from the three-dimensional model at a fixed latitude, to track how the symmetric instability evolves, akin to what is shown in figure 3.2. This is done in figure 3.6. Initially the instability behaves similarly to the two-dimensional case, although the features are slightly distorted by 'noise' from passing eddies and internal waves. In more realistic model set-ups and the ocean, it may not be possible to see the initial, clean evolution of symmetric instability. As such, other diagnostic quantities may be required to de-

tect its excitement.

As with the two-dimensional numerical model, the coarseness of the grid and the use of an enhanced eddy viscosity are key limitations of the three-dimensional integrations presented here. The grid is unable to resolve fully the evolution of secondary instabilities, will suppress the growth rate, and will enhance the vertical extent of the instability. As before, it seems unlikely that this will change the fact that symmetric instability is efficient at neutralising anomalous potential vorticity in waters that have crossed the equator, especially due to the larger growth rate we expect to see when a lower, more realistic viscosity is used. Overcoming these limitations through the use of model integrations at higher resolutions remains computationally very expensive and hence infeasible.

The potential vorticity evolution of the viscous no-slip integration is shown in figure 3.7. The results appear qualitatively similar to those of Edwards and Pedlosky (1998*a*) whose model does not permit symmetric instability. In this model, the viscosity is leading to the dissipation of potential vorticity, which is not as dominant in the standard no-slip integration. At some latitudes, submesoscale patterns are starting to become apparent, particularly at the edges of the anticyclonic eddies. Figure 3.8 shows how the potential vorticity varies with depth. Immediately clear is the presence of symmetric instability-like features, suggesting the high viscosity has only partially suppressed symmetric instability. Note how the vertical length scale of the disturbance is larger in this integration than in the standard no-slip case. This can be understood with reference to figure 2.4 — higher viscosities lead to larger vertical length scales.

The presence of the eddies in the viscous integration, in which symmetric instability is suppressed, suggests that the spin up of the eddies occurs independently of the symmetric instabilities and provides further evidence that the eddies are a result of barotropic instability. In the simulations shown here, both barotropic and

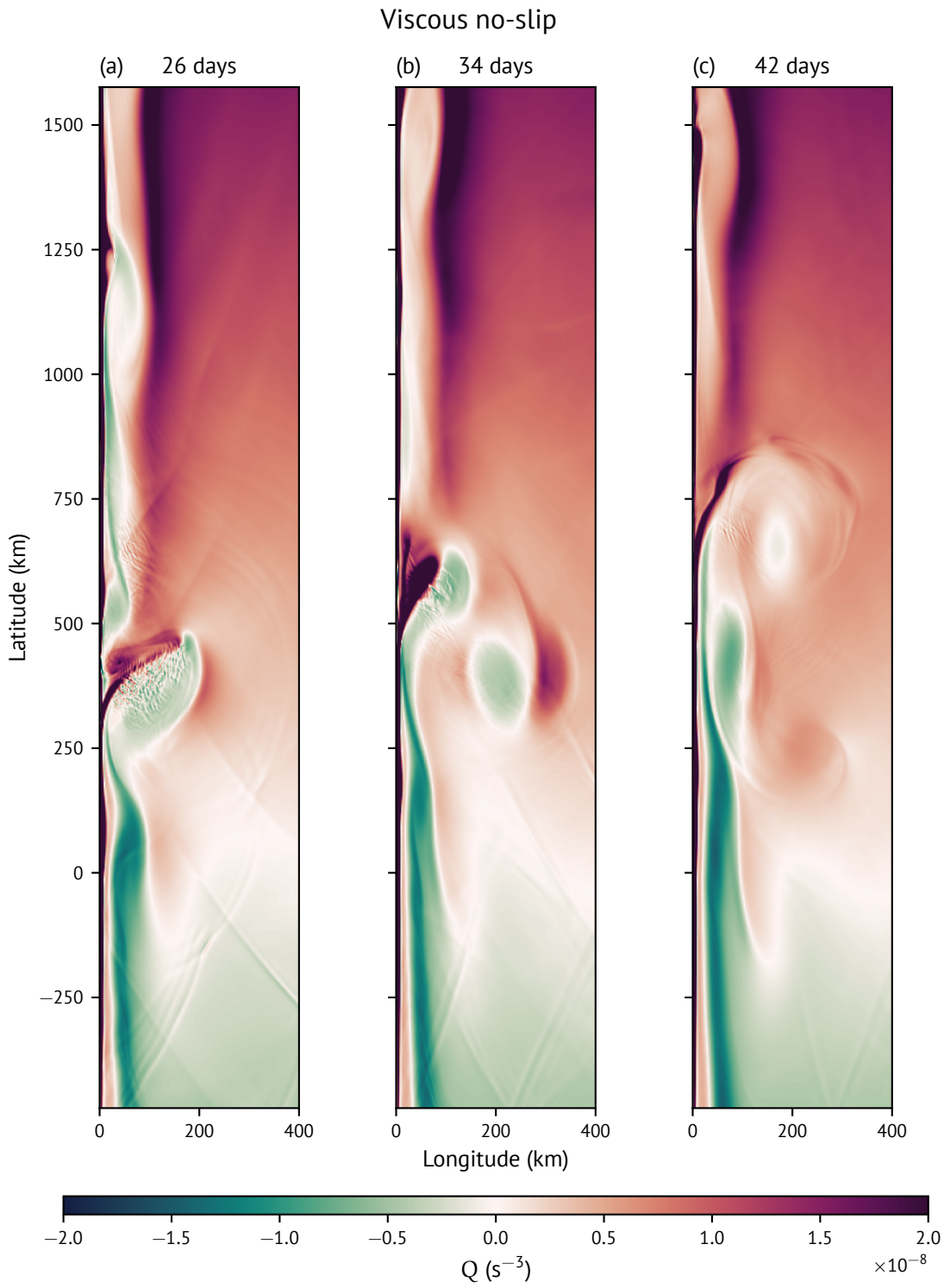


Figure 3.7: Snapshots of potential vorticity at 50 m depth for the no-slip viscous three-dimensional model.

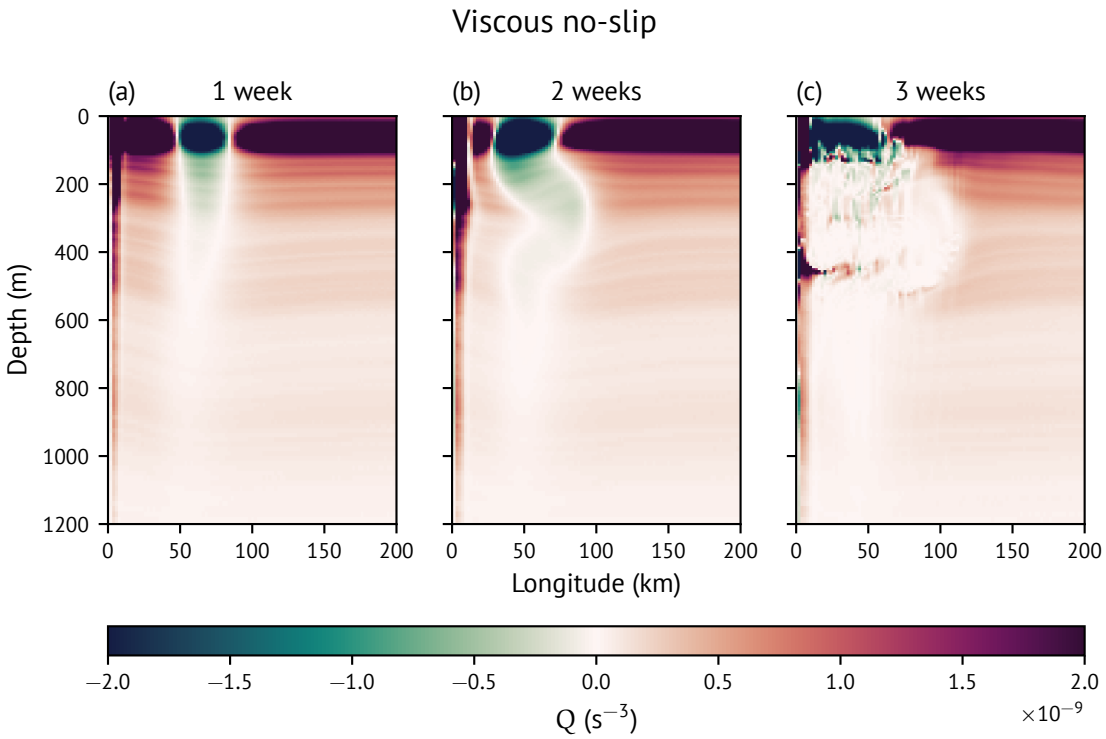


Figure 3.8: Snapshots of potential vorticity as a function of depth and longitude at 750 km north of the equator, in the no-slip viscous three-dimensional model.

symmetric instabilities have similar growth rates and occur concurrently. The simultaneous evolution of both instabilities means they will inevitably interact. In this work we have focussed on the effect of barotropic instability on the evolution of symmetric instabilities, in particular how the barotropic instability modifies the background flow of the western boundary current by spinning up anticyclonic eddies that suppress symmetric instability (see section 2.3). We have not discussed how the presence of symmetric instability affects the evolution of barotropic instability, however, this would be an interesting avenue for further research. The lateral mixing of waters along the boundary, induced by symmetric instability, may affect whether and where North Brazil Current rings detach from the coast. Furthermore, the redistribution of potential vorticity within the western boundary current will likely change the positions of potential vorticity extrema, affecting

both the growth rate and spatial distribution of the barotropic eddies.

3.3.2.2 Free-slip lateral boundary conditions

The behaviour of the three-dimensional model under no-slip and free-slip lateral boundary conditions is qualitatively different. The main difference is the behaviour of the barotropic eddies. The sensitivity to the choice of lateral boundary condition is not seen in the two-dimensional models as they do not allow these barotropic eddies to develop. The differences can be seen by comparing figures 3.4 and 3.9.

In the free-slip integrations, the eddies grow to be more elongated, and propagate northwards more quickly than in the no-slip integrations. They do not retroflect in the same way as before. As they propagate northwards, they entrain waters of negative potential vorticity and elongate, creating a concentrated pool of symmetrically unstable waters. When the eddies do become unstable, the process is much more explosive — this can be seen in figure 3.9. As the eddies propagate northwards more quickly, the symmetrically unstable region is shifted northwards. This is because it takes a similar time for symmetric instability to develop, but the eddies have moved further north of the equator during this time.

The differences in the behaviour of the boundary current and the eddies (and the subsequent impacts on the symmetric instabilities) in the free-slip integrations derive from the differences in boundary layer dynamics. In the no-slip integrations positive vorticity is input at the boundary and this exerts viscous stresses on the adjacent current, producing a turbulent boundary layer. In the free-slip integrations there is no injection of vorticity, leading to a more laminar boundary layer. Edwards and Pedlosky (1998*a*) show that vorticity dynamics do not permit the development of a turbulent boundary layer under free-slip boundary conditions until some distance polewards of the equator; however, under no-slip boundary condi-

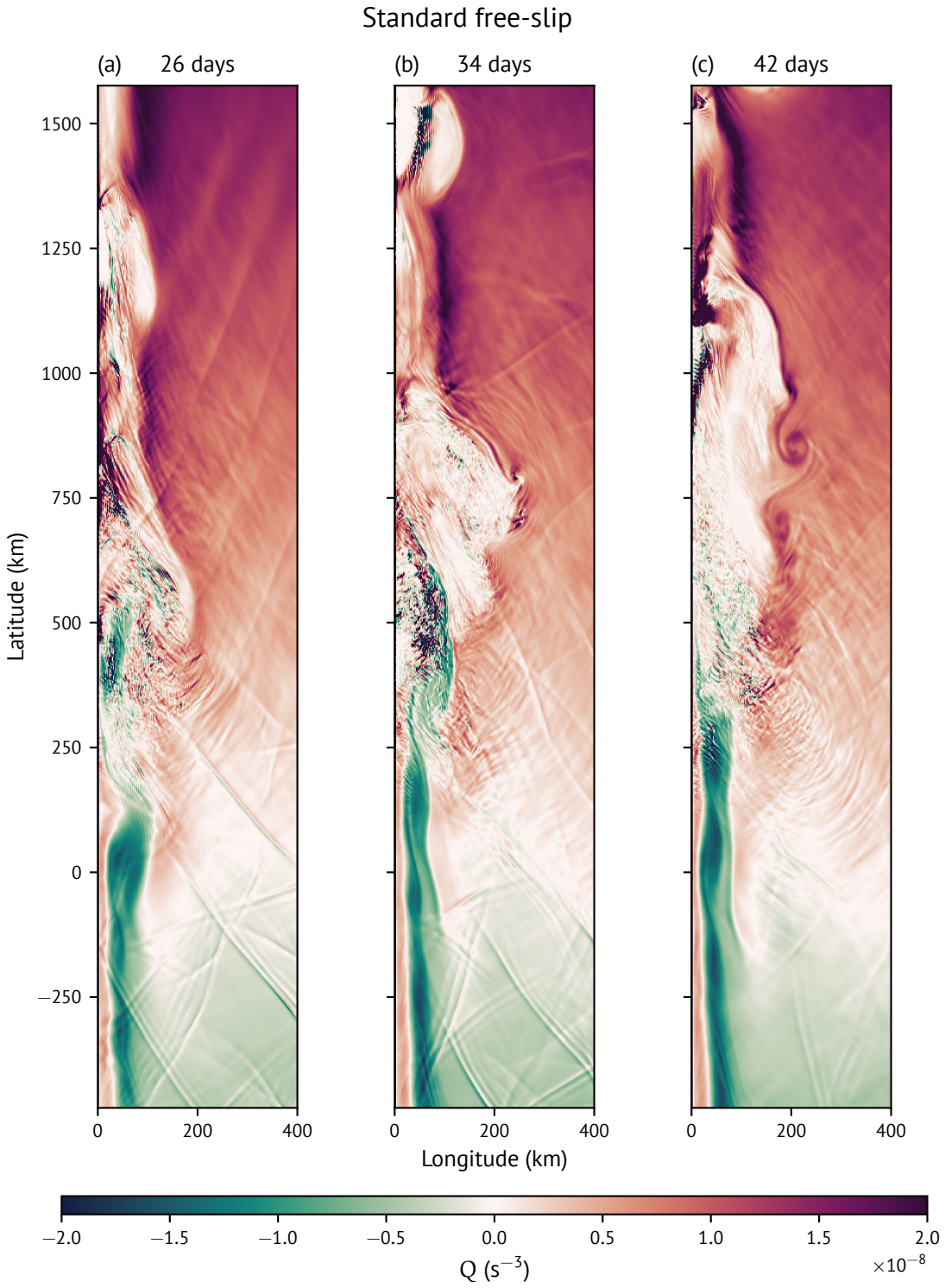


Figure 3.9: Snapshots of potential vorticity at 50 m depth for the free-slip three-dimensional model.

tions a turbulent boundary layer must develop at the equator.

The potential vorticity evolution from a free-slip viscous integration is shown in figure 3.10, reinforcing that, with the noise of symmetric instability removed, the barotropic eddies behave very differently under the two different lateral boundary conditions. This raises the question of what the most appropriate boundary condition is. For the idealised model setup, this is likely the no-slip lateral condition. In a realistic model, given the small aspect ratio of the problem, a no-slip bottom boundary and free-slip lateral boundary condition, along with variable bathymetry might better represent the physics. This is a result of gently sloping ocean bathymetry in the region meaning that the sea floor is better characterised as a bottom boundary, rather than a lateral boundary.

3.3.3 Correlations between relative and potential vorticity

It is useful to be able to define concretely the latitudes at which symmetric instability is occurring. Thus far, this has been done visually by looking at the regions in which submesoscale patterns begin to form in areas of anticyclonic vorticity. It has been noted that regions in which symmetric instability is occurring mark a transition from a regime in which potential vorticity is dominated by relative vorticity to one in which planetary vorticity dominates. Figure 3.5 suggests it may be possible to identify latitudes at which symmetric instability is occurring by considering correlations between relative vorticity and potential vorticity.

The relative vorticity and potential vorticity are interpolated onto the same grid. The Pearson correlation coefficient, r, of the vertical component of relative vorticity and potential vorticity between 21 days and 49 days is calculated for all grid points between the western boundary and 400 km east at 50 m depth for each latitude. The calculation starts at 21 days so that any instability resulting from the initial conditions has died down. How the correlation coefficient varies with

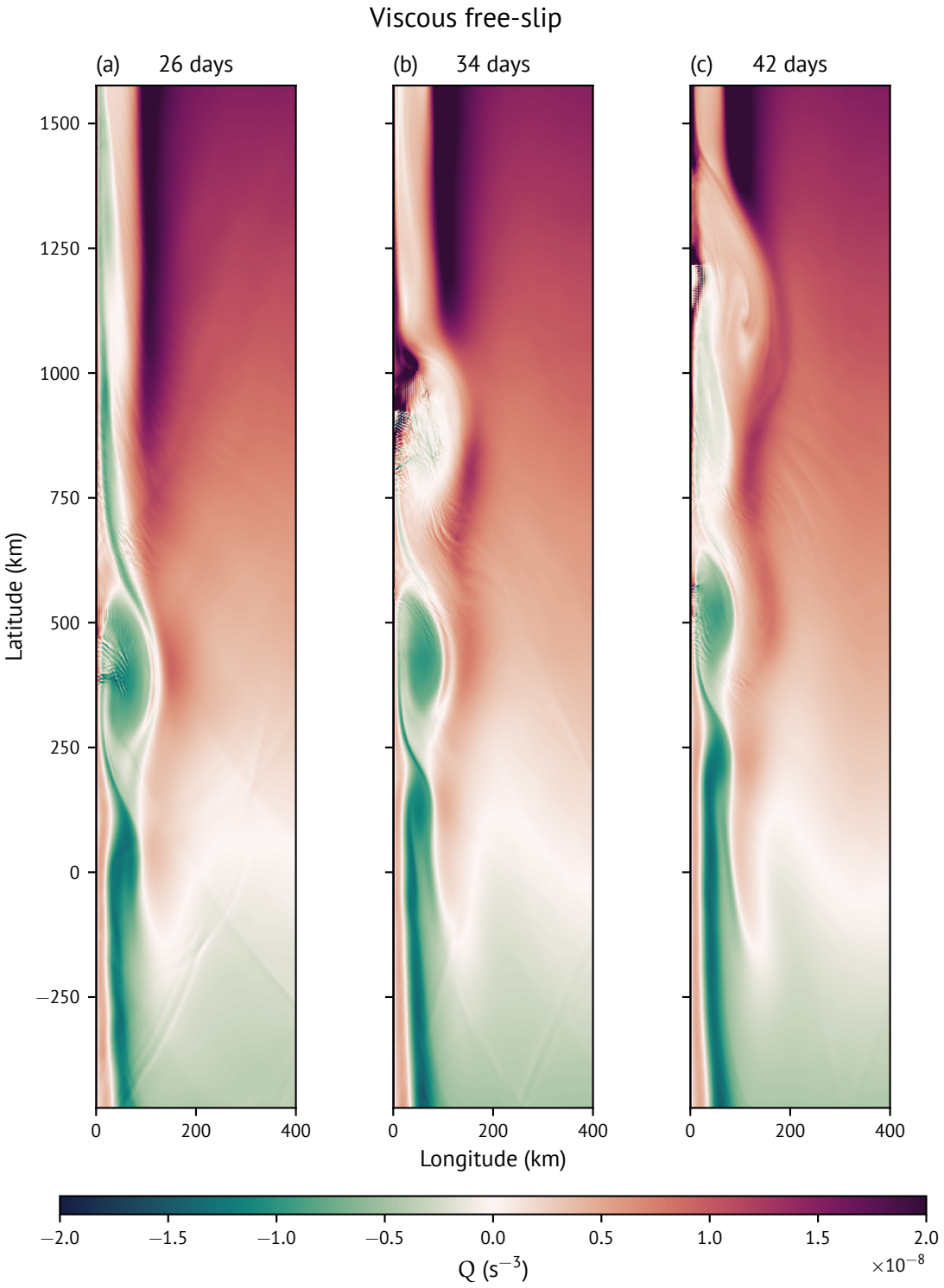


Figure 3.10: Snapshots of potential vorticity at 50 m depth for the free-slip viscous three-dimensional model.

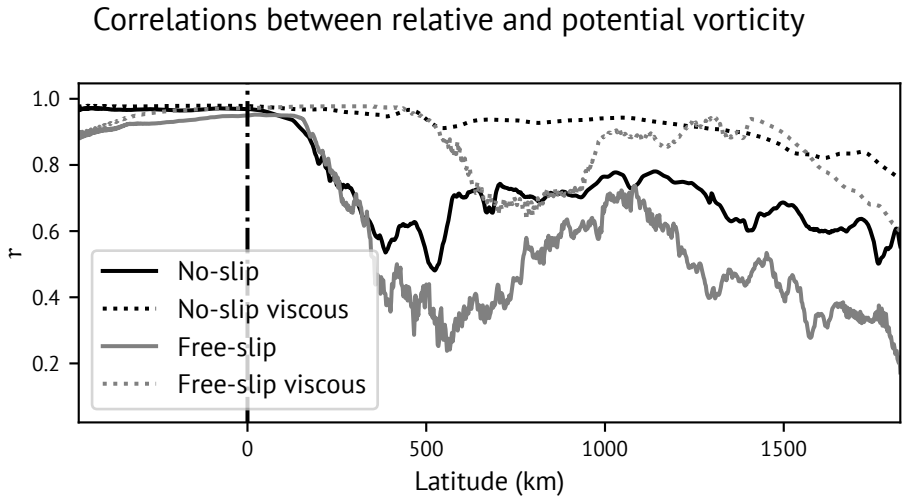


Figure 3.11: Correlations between relative and potential vorticity as a function of latitude. Shown for integrations with a standard (solid lines) or enhanced (dotted lines) vertical viscosity, and for both no-slip (black lines) and free-slip (grey lines) models.

latitude is shown in figure 3.11, for both the no-slip and free-slip, and standard and viscous integrations. In figure 3.11, we see that the vertical component of relative vorticity and potential vorticity are very strongly correlated in the Southern Hemisphere. At around 250 km north of the equator, there is an abrupt change in the correlation of the standard no-slip and free-slip integrations. The latitude of the change seems to correspond to the latitude north of which we observe symmetric instability. In the case of the no-slip integration, r reduces to around 0.5, and for the free-slip integration, it is reduced even further, to less than 0.3. This makes sense — in the free-slip experiment the excitement of symmetric instability appears qualitatively more vigorous than in the no-slip experiment.

We see a much smaller and more gradual drop in the correlation for the viscous integrations, and the decrease in r appears to begin at much higher latitudes — around 500 km for the free-slip and 1,500 km for the no-slip integration. This is consistent with what we see in the models: at low latitudes, we see little evidence

of symmetric instability; however, its effects become apparent at higher latitudes.

We can understand the change in correlations in terms of the potential vorticity of a meridional flow, given by

$$Q \approx \left(N^2 f - M^2 \frac{\partial V}{\partial z} \right) + N^2 \xi \tag{3.4}$$

where N^2 and M^2 are the vertical and horizontal buoyancy gradients, respectively. In the absence of symmetric instability, at a given latitude, one would expect there to be a strong correlation between Q and ξ. If N^2 and f are approximately constant, and M^2 and $\partial_z V$ are small, then the bracketed term of the above equation will be approximately constant and a linear relationship between Q and ξ will exist. When symmetric instability is excited, localized vortex stretching and changes in the vertical shear cause a breakdown of this linear relationship. As such, one would expect the correlation between the vertical component of relative vorticity and potential vorticity to be much lower. The fact that the correlation changes only slightly in the viscous runs, which exhibit barotropic eddies but suppressed excitement of symmetric instability, suggests that the changes in the linear relationship are the result of symmetric instability.

3.3.4 Spectral energy density

Symmetric instability is a submesoscale instability, suggesting that when it is excited we would expect to see an increase in the amount of energy at small length scales. Yankovsky and Legg (2019) find that in their models of Arctic overflows, symmetric instability has a fingerprint in the spatial Fourier transform of the vertical kinetic energy. This technique is used here in an attempt to diagnose symmetric instability.

For the standard three-dimensional no-slip integration, the quantity $w^2/2$ is

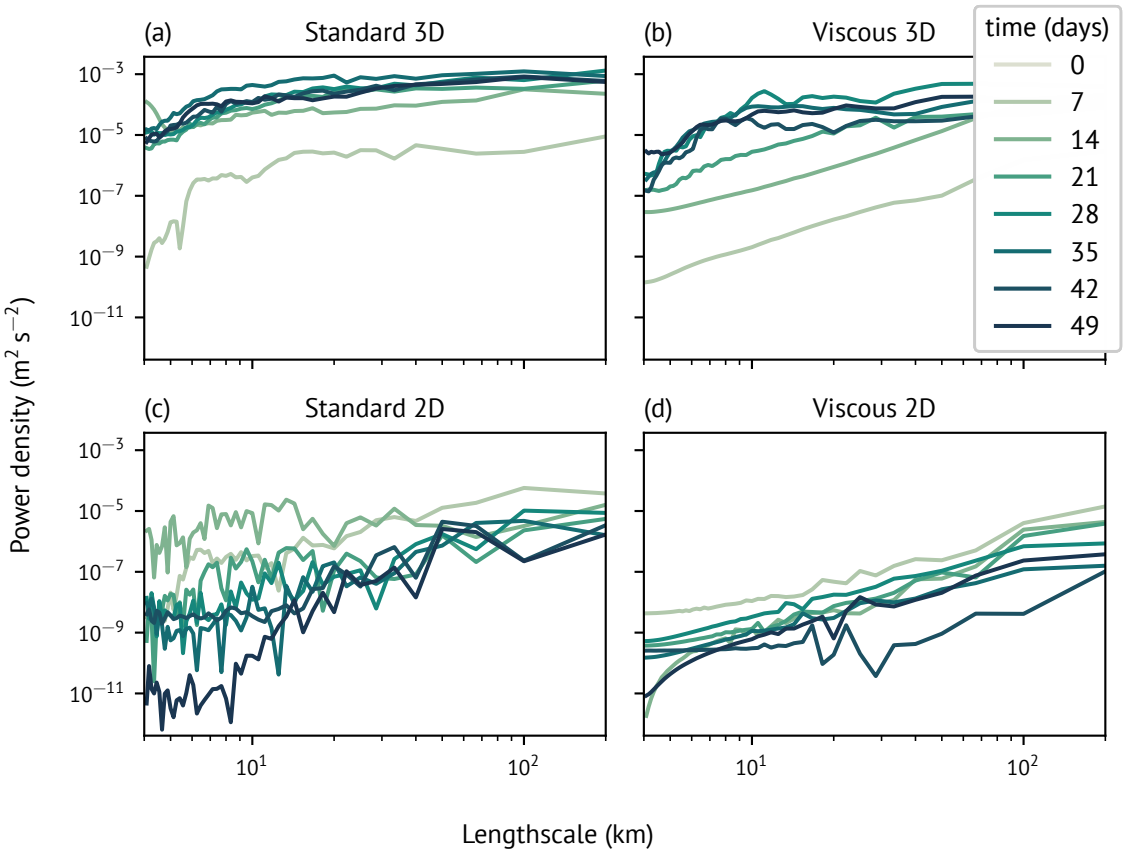


Figure 3.12: Spectral distribution of vertical kinetic energy for the (a) standard three-dimensional, (b) viscous three-dimensional, (c) standard two-dimensional, and (d) viscous two-dimensional models. Note that the vertical viscosity used in the viscous two-dimensional integration is 6×10^{-3} m^2 s^{-1} compared to 10^{-2} m^2 s^{-1} for its three-dimensional counterpart. The darkening line colour corresponds to later model times.

calculated at a depth of 50 m from the western boundary to 200 km east, and from 250 km to 750 km north. The power spectrum is taken along the zonal dimension and the meridional mean is taken. This is plotted at one-week intervals in figure 3.12a. The same is done for the three-dimensional viscous no-slip integration in figure 3.12b. The same procedure is performed for the single latitude of the two-dimensional standard and viscous no-slip models and the results are shown in figures 3.12c and 3.12d respectively.

In each of the panels (a), (b) & (c) of figure 3.12, we see a flattening of the power spectra over time. This corresponds to the development of vertical motions with a structure that varies over small-length scales. In the case of the standard three-dimensional model, within around a week, the power spectrum reaches an equilibrium.

In the viscous three-dimensional model, it takes around three weeks for the flattening to take place. This is due to the increased vertical viscosity suppressing symmetric instabilities. We still see the flattening effect of symmetric instability at later times, as the viscosity is not sufficient to completely inhibit its development.

In the standard two-dimensional model, after an initial flattening of the spectra, there is a subsequent steepening from four weeks onwards. After four weeks, the two-dimensional model has used up most of its finite reserves of negative potential vorticity which fuels the symmetric instability. This means that there is no process to sustain the small-scale vertical motions and they begin to die away. This is in contrast to the three-dimensional model in which the supply of negative potential vorticity is constantly being replenished by the advection of Southern Hemisphere waters across the equator. As the two-dimensional model is not capable of producing barotropic eddies, we can be fairly certain that the changes in the power spectrum are not related to them. The increased variability relative to the three-dimensional models is due to the removal of the meridional averaging step.

In the viscous two-dimensional model, in contrast to its three-dimensional counterpart, we see no flattening at all in the power spectra[3]. This is because the vertical viscosity is sufficient to completely inhibit symmetric instability in this model. The stationarity of the power spectra allows us to say with some confidence that the flattening seen in the other models is due to the presence of symmetric instability. Indeed, the flattening of power spectra may prove useful for identifying symmetric instability in more complex ocean models and in observations, in which the signature of symmetric instability may otherwise be less obvious.

The power spectra appear to show a lot of power concentrated at the grid scale. Inspection of the vertical velocities in the region suggests this is not the result of grid-scale noise, but rather physical flow structures. Note also that the axes in figure 3.12 are logarithmic.

3.3.5 Transformation of water masses

Symmetric instability leads to the generation of small-scale overturning cells. Such cells may be expected to lead to the mixing of waters with different densities and contribute to water mass transformation. In the Walin (1982) water mass transformation framework, the rate of formation of water between two isopycnal surfaces ρ and $\rho + \Delta\rho$ is given by

$$\mathcal{F} = \frac{\partial \mathcal{V}}{\partial t} + \Delta\psi = G(\rho) - G(\rho + \Delta\rho) \tag{3.5}$$

where $\mathcal{F}$ is the rate of formation of fluid between the isopycnals, $\mathcal{V}$ is the volume bounded by the isopycnals, $\Delta\psi$ is the net volume flux out of the region, and $G(\rho)$ is the diapycnal volume flux across the ρ-isopycnal — also known as the water mass transformation. By convention, a positive value of G corresponds to a flux

[3] Note that the viscous two-dimensional model uses a viscosity of 6×10^{-3} m^2 s^{-1} compared to 10^{-2} m^2 s^{-1} for the viscous three-dimensional model.

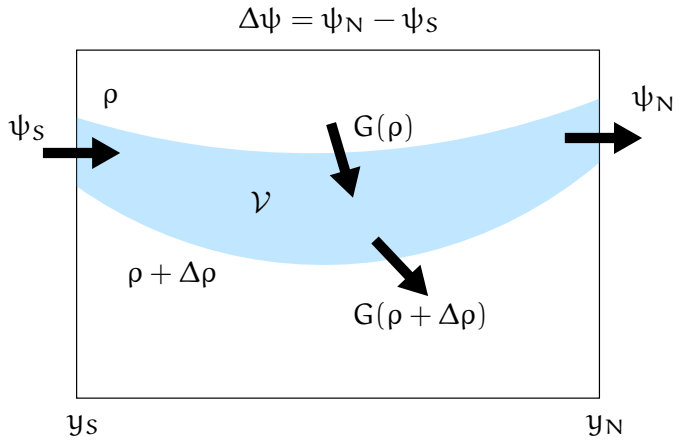


Figure 3.13: Sketch of the processes contributing to water mass formation in the Walin (1982) framework. Based on a figure in Williams and Follows (2011).

from lighter to denser waters. These quantities are shown diagrammatically in figure 3.13.

The water mass formation rate is calculated for density classes of $\gamma^n \leq 23.45$, $23.45 < \gamma^n \leq 26.50$ and $\gamma^n > 26.50$. Physically these correspond to a surface layer, the pycnocline and deep ocean, and are marked in figure 2.3 alongside the initial stratification profile. The formation is diagnosed in latitude bands with boundaries at -500 km, -250 km, 0 km, 250 km, 750 km, and 1, 500 km for both the standard no-slip and viscous no-slip integrations. There is a large amount of temporal variability in the formation and so it is hard to discern any trends in the volumes of the chosen density layers. To remove this variability, the 3-day rolling average is taken. We also normalise the formation rate by the latitude band width, giving the water mass formation rate in units of $\mathrm{Sv\,km^{-1}}$. The results of the calculation are shown in figure 3.14. By cumulatively integrating the time series, it is easier to identify long-term trends in formation. Figure 3.15 shows the cumulative

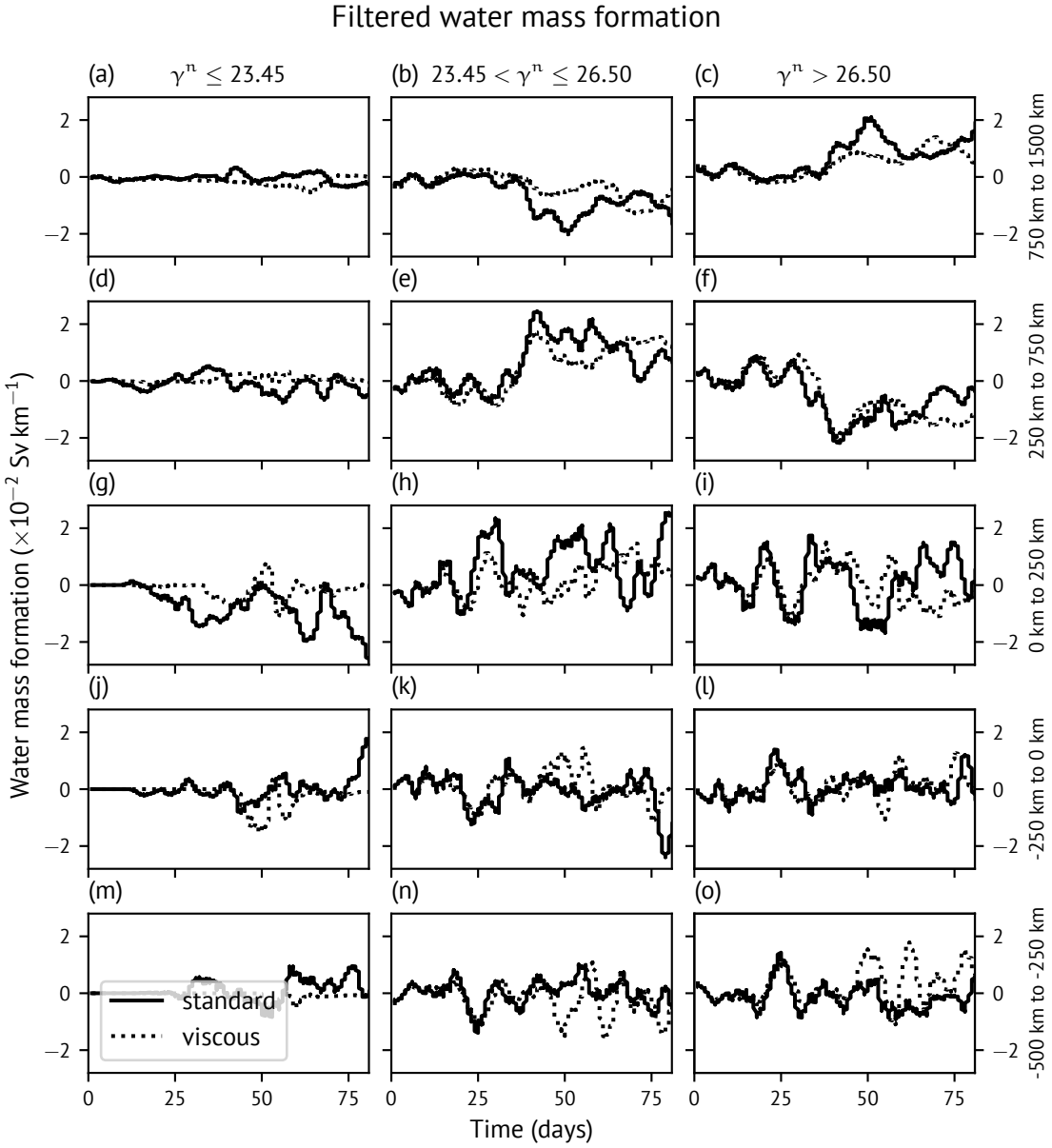


Figure 3.14: Water mass formation rates for the surface, pycnocline and deep ocean (columns) within different latitude bands (rows). Rates are shown for the three-dimensional standard (solid lines) and viscous (dotted lines) no-slip models. High-frequency variability is filtered from the rates by taking a 3-day rolling average.

formation (normalised by latitude band widths) in each of the density classes and latitude bands.

Outside the 0 km to 250 km latitude band, there are no large changes in the net formation within the surface layers for the standard integration. Within this band, we see a large decrease in cumulative formation. This corresponds to the creation of denser waters by the action of symmetric instability, mixing surface and intermediate waters — there is an almost equal and opposite increase in the formation of intermediate waters over time. By the time the surface waters are north of 250 km they are largely free of anomalous potential vorticity, meaning there is near-zero further mixing north of this latitude. There is little net-formation in the surface of the viscous integrations, with the vertical viscosity being sufficient to shut down the growth of symmetric instability modes within these layers.

There is a transformation between the intermediate water and deep water density classes from 250 km to 1,500 km north of the equator. The formation rates are larger in the standard than in the viscous integrations as would be expected. In the 250 km to 500 km band, we see the creation of intermediate waters from deep waters and from 500 km to 1,500 km we see the creation of deep waters from intermediate waters. Given the larger width of the northern latitude band, the net effect will be to form denser deep waters from intermediate waters. This occurs at a rate of between 2 Sv and 4 Sv from 250 km to 1,500 km north of the equator.

Symmetric instability-induced mixing is suppressed more strongly by the high viscosity in the intermediate waters than in the deep waters. This is due to the presence of the pycnocline enhancing the suppression of symmetrically unstable modes — the high stratification acts to restrict the growth of larger modes whereas the high viscosity prevents smaller modes from becoming well established.

Figure 3.4 shows potential vorticity in the standard no-slip integration at a depth of 50 m which in density space sits just below the interface between the

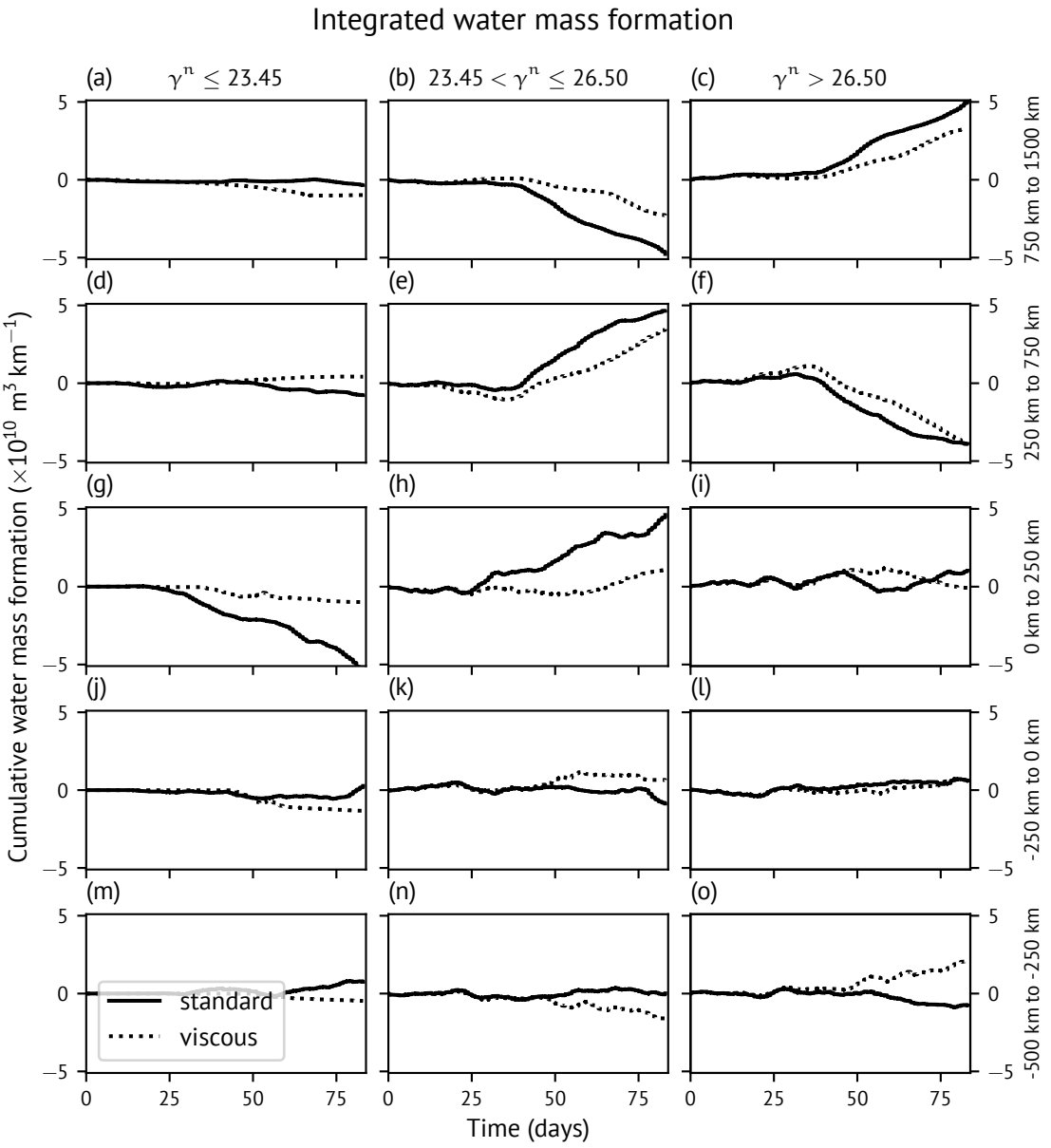


Figure 3.15: Cumulatively integrated water mass formation rates for the surface, pycnocline and deep ocean (columns) within different latitude bands (rows). The net formation is plotted for the three-dimensional standard (solid lines) and viscous (dotted lines) no-slip models.

surface and intermediate waters[4]. Due to the noisiness of the water mass formation rates it is difficult to link specific changes to features in the potential vorticity field. The passage of the anticyclonic eddy initially centred around 300 km north at 26 days to 850 km north after 42 days is however visible. Looking at panel (h) of figure 3.14 we see a peak in the water mass formation rate between days 24 and 35. During this time the eddy is within the 0 km to 250 km latitude band and the action of the instabilities leads to enhanced mixing of around 2×10^{-2} Sv km^{-1}. In panel (e) there is another increase in the water mass formation rates beginning around day 30 and peaking around day 40, again at a rate of approximately 2×10^{-2} Sv km^{-1}. This is due to the same eddy entering the 250 km to 750 km North latitude band and symmetric instability being excited whilst it is there. Finally, panel (b) shows an increase in formation rates in the northernmost latitude band from around 50 days, when, from its previous trajectory, we would expect the eddy to start crossing the 750 km north latitude band. There isn't a drop in the water mass formation rates within the 250 km to 750 km latitude band at this time as the eddy leaving the region in the North is replaced by a new eddy with negative potential vorticity entering from the South.

A key limitation of the water mass formation rates found here is that they are affected by the vertical viscosity used, suggesting different formation rates would be found if a lower viscosity were employed. Yankovsky and Legg (2019) find that mixing by symmetric instability is largely adiabatic, with irreversible mixing resulting from secondary shear instabilities. The model grid used here is too coarse to resolve such secondary instabilities, suggesting formation rates may be higher if a finer grid were used. It seems unlikely that this limitation will alter the key finding that symmetric instability is efficient at removing anomalous potential vorticity

[4]Strictly speaking we should have plotted the potential vorticity on an isopyncal surface, however, this was not done due to the computational costs of interpolating the field on to an isopycnal surface, and the amount of extra storage space that would have been required to save all the requisite model diagnostics.

originating from the opposing hemisphere.

3.4 Summary

In this chapter, we presented results from two-dimensional and three-dimensional numerical models of a Bickley jet crossing the equator. In the two-dimensional models, we were able to see the clean evolution of symmetric instability and the generation of stacked overturning cells confined to regions of negative potential vorticity as predicted by the linear stability analyses of section 2.4 and 2.5.

The two-dimensional model neglects the β-effect and constrains the horizontal motions of the flow. A further degree of realism was added by developing an idealised three-dimensional model of the Tropical Atlantic which incorporates these effects. As the flow evolves in the model, two main classes of instability develop. The first is the spinning up of anticyclonic eddies as the fluid crosses the equator. This is a result of barotropic instability and has been both investigated and observed in the works of Edwards and Pedlosky (1998*a*,*b*) and Goes et al. (2009). The second instability is identified as symmetric instability for the following reasons:

- The characteristic timescale of the instability is of the same order of magnitude as that predicted by linear stability analyses.
- The vertical length scales of the overturning cells that develop are consistent with those predicted by linear stability analyses.
- The instability is confined to regions of negative potential vorticity with minimal penetration of the instability into regions of positive potential vorticity.
- Eddies with strongly negative potential vorticity fuel the excitement of the instability, becoming unstable towards the edge of their cores first, as predicted by linear stability theory.

- Water leaving regions of instability have potential vorticity that is neutrally stable to symmetric instability.
- The latitude at which the instability occurs is explained well by arguments about the latitudinal dependence of the growth rate of symmetric instability.
- The instability can be suppressed in numerical models via the imposition of a sufficiently high vertical viscosity, as predicted by linear stability theory.
- The power spectrum of the vertical kinetic energy in the standard three-dimensional integration is similar to that in its two-dimensional counterpart. The latter unambiguously shows symmetric instability and shows that the change in the spectrum is not the result of barotropic instability. Moreover, the power spectrum of the viscous two-dimensional integration, which displays no signs of symmetric instability also remains stationary, with no flattening occurring.

We hypothesised the excitement of symmetric instability could lead to the transformation of fluids between different water mass classes. An analysis of the water mass formation rates in the surface, pycnocline and deep ocean suggests that the net contribution of symmetric instability to the AMOC's overturning budget could be significant. We see typical transformation rates of $\pm 2 \times 10^{-2}$ Sv km^{-1}, but reaching as high as ± 4 Sv when integrated over latitude bands. Over longer time scales these transformations imply the formation of deep waters from intermediate waters. A key limitation of these water mass transformation calculations is the viscosity dependence of the overturning cells generated by the instability. In the ocean we expect a lower limit of their vertical extent to be around 15 m, which would likely alter the formation rates we have calculated in this study. Furthermore, Yankovsky and Legg (2019) find that the mixing of waters by symmetric instability is largely adiabatic and that secondary shear instabilities are what

cause irreversible mixing. Achieving a high enough resolution with the three-dimensional models presented here may be difficult, however, a modified two-dimensional model may prove useful for obtaining better estimates.

Mixing aside, the key finding of this work is that symmetric instability is an efficient mechanism for removing anomalous potential vorticity originating from the opposite hemisphere in cross-equatorial flows. This work has focussed on currents dynamically similar to the North Brazil Current, however, the findings may also apply to other surface intensified cross-equatorial flows, such as the Somali current, an intense, seasonal, wind-driven western boundary current in the Indian Ocean. In the next chapter, we will explore the excitement of symmetric instability in the Deep Western Boundary Current, the AMOC's return flow, as it crosses the equator. We will compare what is seen at depth, to what we have seen in this chapter, and explore the overturning cells generated by symmetric instabilities further.

Chapter 4

Symmetric instability in a cross-equatorial deep western boundary current

So, does the staircase stay exactly as is, then?

Kevin McCloud, Grand Designs

We have just seen how symmetric instability can be excited in a surface-intensified western boundary current as it crosses the equator, and you may wonder whether the findings of the preceding chapter apply to deep western boundary currents also. In this chapter, we will see that to some extent they do, and that symmetric instability may indeed be excited in cross-equatorial deep western boundary currents. We will explore how symmetric instability leads to the generation of density staircases in idealised models, potentially providing an easily observable fingerprint by which symmetric instability might be inferred observationally. We then go on to look at a simplified model of staircase formation and contrast what is going on in the Deep Western Boundary Current with what is going on in the surface North Brazil Current.

In section 4.1 we will introduce the Deep Western Boundary Current in the Tropical Atlantic. In section 4.2 we describe our idealised numerical model of the Deep Western Boundary Current crossing the equator. In section 4.3 we demon-

strate the formation of density staircases and the excitement of symmetric instability in the model, and propose that the staircases are generated as a result of the excitement of symmetric instability. Simple scaling arguments are used to explain the differences between the instabilities seen in deep western boundary currents and surface-intensified currents. Finally, in section 4.4 we summarise our findings and explain the potential implications of our results.

This chapter is based on a manuscript published in Geophysical Research Letters (Goldsworth et al., 2022). I took the lead in the experimental design, implementation and authoring of the work.

4.1 The Deep Western Boundary Current in the Tropical Atlantic

The Deep Western Boundary Current is the other major western boundary current system of the Tropical Atlantic. Unlike the North Brazil Current it is not driven by wind forcing and gyre circulations, rather, it is the main pathway of North Atlantic Deep Waters across the equator and into the Southern Ocean. Around 2/3rds of the AMOC's deep interhemispheric transport occurs in this current, with the remainder crossing the equator via interior pathways (Arhan et al., 1998; Bower et al., 2019). The current has a peak velocity of around 20 $\mathrm{cm\,s^{-1}}$, sits at a depth of approximately 1,200 m to 3,600 m and is around 100 km wide (Rhein et al., 1995). At 5°S it transports 25.5 ± 8.3 Sv of water southwards (Schott et al., 2005). In the previous chapter, we saw how symmetric instability can be excited in surface intensified cross-equatorial western boundary currents; however, the susceptibility of deep western boundary currents to symmetric instability remains an open question. In the chapter, we will not only show that deep western boundary currents are susceptible to symmetric instability, but that this instability can result in the

formation of density staircases.

Density staircases are step-like features which can be seen in plots of seawater density against depth, and they are ubiquitous in the global ocean (Stern, 1960; Tait and Howe, 1968; Johannessen and Lee, 1974; Lambert and Sturges, 1977; Melling et al., 1984; Schmitt et al., 1987). The staircases consist of alternating well-mixed regions with low stratification and thin interfaces with high stratification. The high stratification interfaces act as "mixing barriers" which inhibit the vertical transport of water properties such as heat and salt, whereas mixing is enhanced in the low stratification regions. Density staircases can affect both diapycnal mixing and water mass transformation rates (Schmitt et al., 2005), which are known to be important in closing the AMOC's overturning budget (de Lavergne et al., 2022). Many staircases are thought to form as a result of double-diffusive convection (Merryfield, 2000), but other staircase generation mechanisms have been identified, such as inhomogeneous mixing (Balmforth et al., 1998).

4.2 Model configuration

Simulations of an idealised deep western boundary current crossing the equator are performed using the MITgcm (Marshall et al., 1997). The domain size is 600 km in the zonal direction, 3,600 km in the meridional and 4,500 m in the vertical. The horizontal grid spacing is 1 km and the vertical grid spacing is 10 m. As with the models of the North Brazil Current, the horizontal resolution is chosen to ensure the model adequately resolves the small-scale vorticity dynamics we are studying and the vertical resolution is chosen to be smaller than the expected size of the overturning cells that symmetric instability generates[1]. The time step is

[1] A higher horizontal resolution is used here than in the North Brazil Current simulations, as at the time of the integrations being performed I was helping to test the ARCHER2 HPC facility before it came online. I had been instructed to try and push the system in terms of both the number of cores being used and the amount of data being produced.

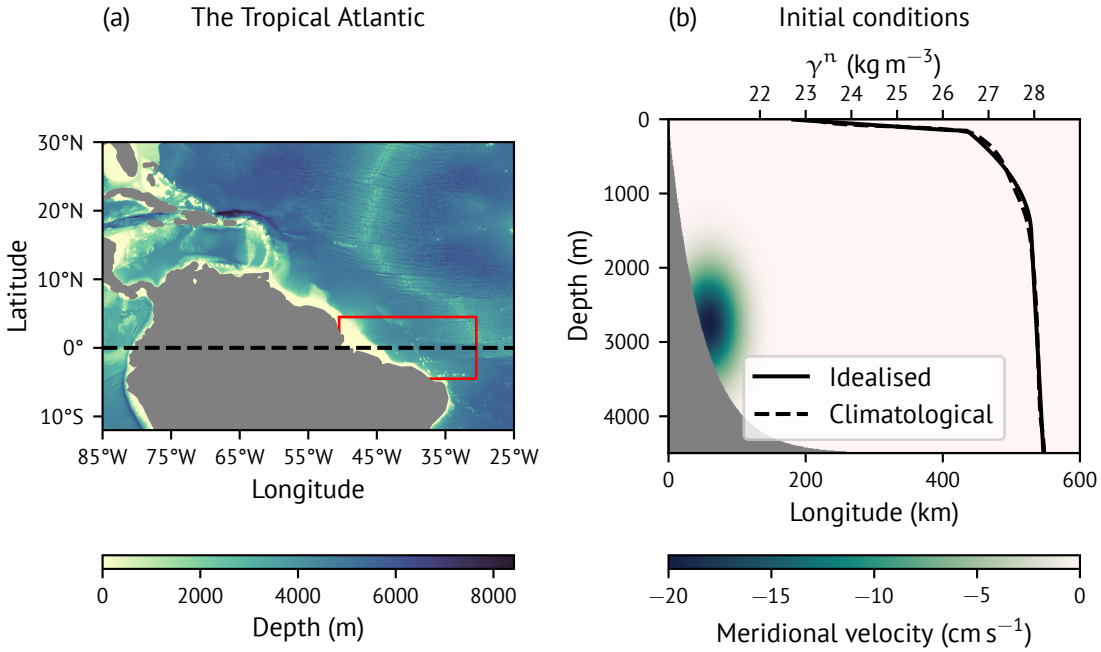


Figure 4.1: (a) Bathymetric map of the western tropical Atlantic. Climatological profiles of neutral density were aggregated from the area enclosed by the red rectangle. Bathymetry data is from the GEBCO Compilation Group (2020) dataset. (b) Meridional velocity (colours) and density (solid line) profiles used as initial and boundary conditions for the model. The velocity profile is based on observations by Schott et al. (2005), and the density profile on the climatological mean from Boyer et al. (2018) (dashed line).

144 s and the model is integrated for a total of 239 days. The longer integration time is chosen as the slower speeds of the Deep Western Boundary Current mean the model takes longer to spin up. The model domain is sited on a β-plane, with the equator placed 2,000 km north of the southern boundary. The meridional gradient in the Coriolis parameter is set to 2.3×10^{-11} s^{-1} m^{-1}, and the meridional component of the Coriolis parameter is set to 1.5×10^{-4} s^{-1}.

At the surface, a rigid lid boundary condition is employed. The lateral boundary conditions are set to be free-slip and the bottom boundary condition to no-slip. The model has sloping bathymetry as shown in figure 4.1b, which also shows the meridional velocity and density profiles used to initialise the model. The zonal velocity is initially set to zero. The density profile is based on a neutral density climatology aggregated from the area enclosed by the red rectangle in figure 4.1a. The model is forced by prescribing the meridional velocity, zonal velocity, and density, at the northern and southern domain boundaries. The same fields used to initialise the model are used as boundary conditions. A sponge region is placed at both the northern and southern edges of the domain. The northern sponge is 100 km thick and the southern sponge is 300 km thick. The inverse relaxation timescale varies from 1×10^{-5} s^{-1} (corresponding to a timescale of around 1.2 days) at the external boundary of the sponge region to 0 s^{-1} at the model-sponge interface. The inverse relaxation timescale has a hyperbolic tangent shape, with a characteristic length scale of 5 km in the northern sponge and 10 km in the southern sponge.

As in chapter 3, a linear equation of state is used, with a reference density of 1,022.73 kg m^{-3} and thermal expansion coefficient of 2×10^{-4} K^{-1}. The linear equation of state avoids the complexities added by non-linear effects such as thermobaricity and cabbelling (e.g. Groeskamp et al., 2016). The thermal diffusion coefficient is set to 1×10^{-5} m^2 s^{-1}. A second-order-moment Prather advection scheme with a flux limiter is employed. Salinity is set to be constant and has no impact on

the dynamics. Momentum dissipation is provided by a vertical Laplacian viscosity of 4×10^{-4} m^2 s^{-1} and an adaptive biharmonic Smagorinsky viscosity which acts on horizontal momentum gradients. Potential vorticity is calculated using the C-grid algorithm of Morel et al. (2019).

4.3 Symmetric instability and staircase formation

Figure 4.2b shows $\partial_z b$ in the model after 239 days of integration 250 km south of the equator. Immediately apparent are the thin, sharp regions of high stratification (so-called "mixing barriers") separating larger regions of well-mixed waters with low and uniform stratification. Moving to 500 km south, we see in figure 4.2c that some weaker barriers have dissipated, however, the stronger barriers remain. Figure 4.2a shows the squared buoyancy frequency at the equator. At the outer edge of the current's core, we see some weak mixing barriers.

Figure 4.3a shows the average of the meridional component of relative vorticity between 234 and 239 days of model integration in a region 250 km south of the equator. This can be thought of as a crude proxy for a zonal overturning stream function — it measures the local rotation around the meridional axis, i.e. the amount of zonal overturning. As the flow is not invariant in the meridional direction, the "true" zonal overturning stream function is ill-defined, so here we will consider the meridional vorticity instead. Examining the meridional vorticity, note that there are a series of counter-rotating stacked overturning cells between around 1,750 m and 3,500 m below the surface. The black contours overlain show $\partial_z b = 2 \times 10^{-6}$ s^{-2} and help identify the locations of the mixing barriers. We can see that the structure of the stratification and the meridional vorticity are remarkably similar, with the horizontal edges of the overturning cells (vorticity zeros) approximately coinciding with the locations of the mixing barriers. This can also be seen

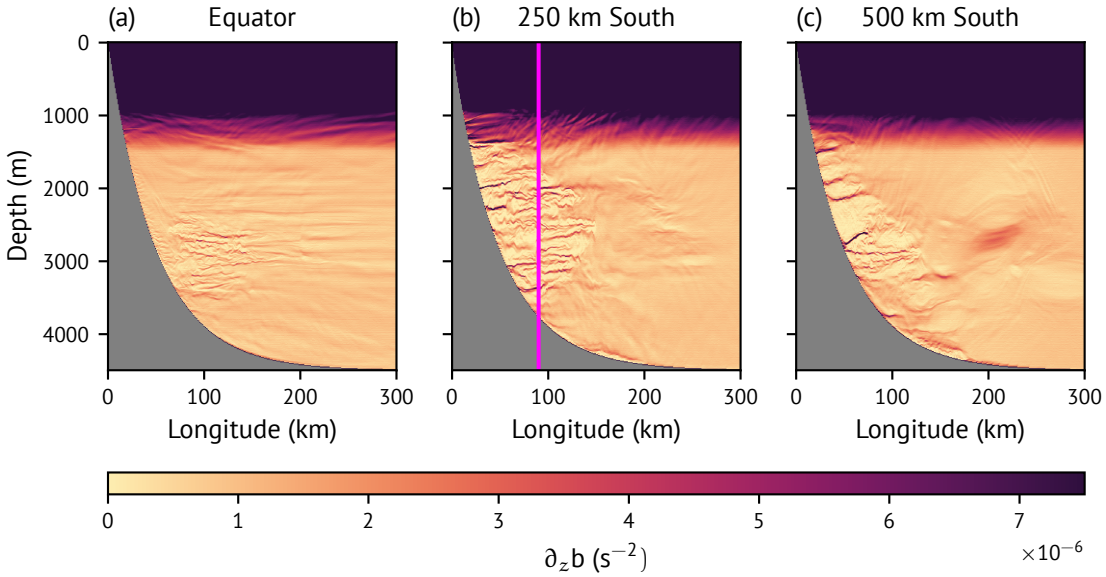


Figure 4.2: Squared buoyancy frequency after 239 days of model integration plotted at (a) the equator, (b) 250 km south of the equator and (c) 500 km south of the equator. The magenta line indicates the location of the vorticity and density profiles shown in figure 4.3.

in figure 4.3b. The black line shows neutral density plotted as a function of depth at 250 km south and 90 km west (the location of the magenta lines and points shown in the other figures). The orange line shows the meridional component of relative vorticity at the same point. Both quantities have been averaged over the period spanning 234 to 239 days. The treads of the steps in neutral density correspond to mixing barriers and the risers to well-mixed regions. When comparing neutral density and the meridional vorticity we again see that the mixing barriers tend to coincide with vorticity zeros, whereas the mixing barriers coincide with vorticity extrema. This suggests that the inhomogeneous mixing driven by the overturning cells is what is causing the formation of the staircases.

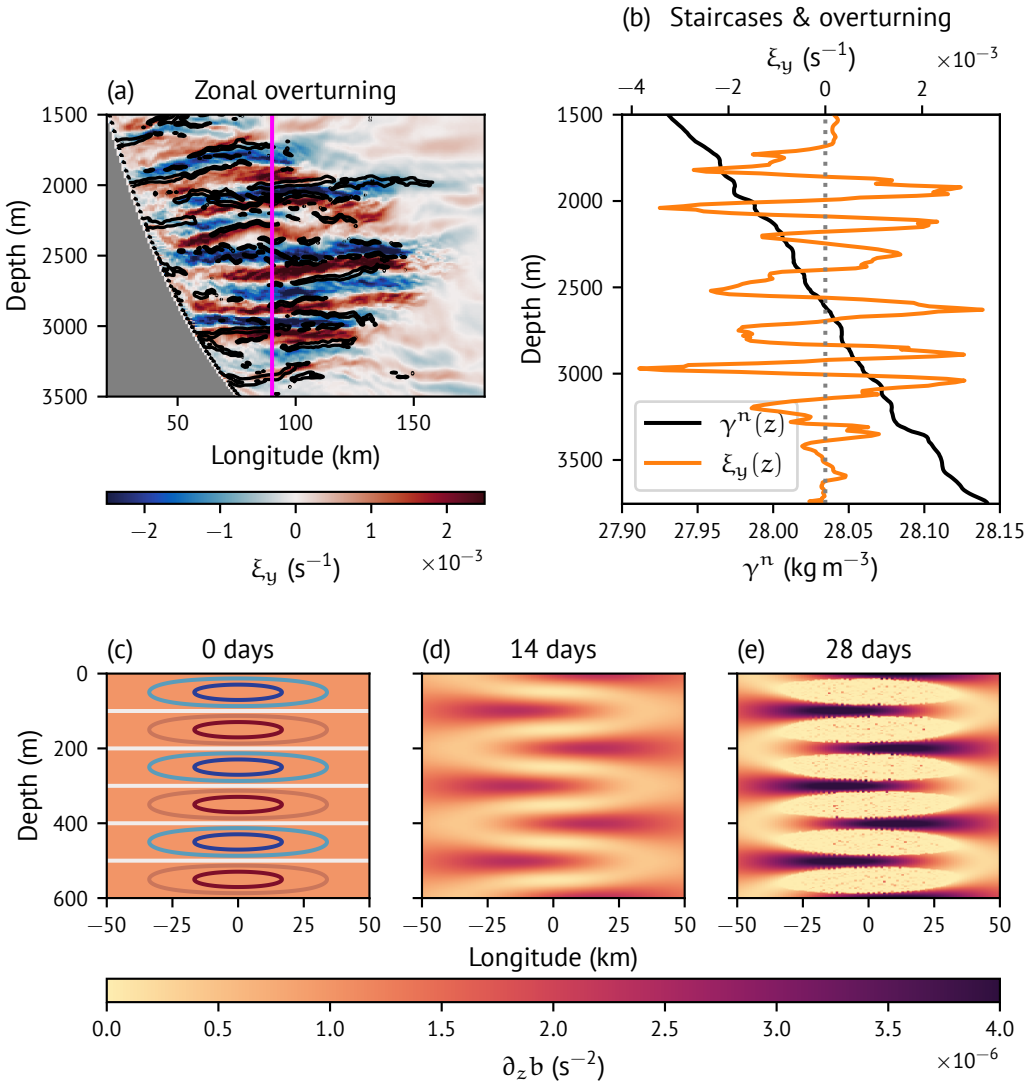


Figure 4.3: (a) The time mean meridional component of relative vorticity between 234 and 239 days of model integration, plotted as a function of longitude and depth, at 250 km south. Overlain is the contour defined by $\partial_z b = 2 \times 10^{-6}$ s^{-2}, indicating locations of mixing barriers. (b) Density (black line) and the time mean meridional component of relative vorticity (orange line) plotted as a function of depth at 90 km west and 250 km south (shown on other figures as a magenta line or point). Panels (c) to (e) show snapshots of the stratification over time from the toy model. The contours on panel (c) show the overturning stream function used to drive staircase formation.

4.3.1 A very simple model of staircase formation

The differential mixing which produces the mixing barriers is analogous to the process which produces zonal jets on a β-plane (Manfroi and Young, 1999). Manfroi and Young (1999) study a sheared zonal flow on a β-plane and find that mixing in the presence of a meridional gradient in planetary vorticity leads to the preferential formation of zonal jets. The separation of the jets is set by the strength of the mixing. Here, instead of a meridional gradient in planetary vorticity, there is a vertical gradient in buoyancy and instead of mixing in the horizontal plane we have overturning in the vertical plane. We can reproduce the formation of mixing barriers with a toy model, in which we consider how buoyancy changes over time as a result of vertical diffusion and advection by overturning cells. If we express the overturning motion as a stream-function ψ where $u = -\partial_z \psi$ and $w = \partial_x \psi$ and use a constant harmonic diffusivity, κ we can express the evolution of b as

$$\frac{\partial b}{\partial t} = \frac{\partial \psi}{\partial z}\frac{\partial b}{\partial x} - \frac{\partial \psi}{\partial x}\frac{\partial b}{\partial z} + \kappa \frac{\partial^2 b}{\partial z^2}\,. \tag{4.1}$$

This is the advection-diffusion equation of a passive tracer in a two-dimensional flow. We choose $\psi = e^{-x^2/2\delta_x^2}\sin(mz)$, to represent stacked overturning cells which are localised to a region of width δ_x in the horizontal. We also set $b(t=0) = N^2 z$, and then solve the equation numerically using the 3rd order Adam's Bashforth scheme on a domain stretching from -50 km to 50 km in the horizontal and spanning 600 m in the vertical. We set $\delta_x = 25$ km, $m = 2\pi/200\,\mathrm{m}^{-1}$, $\kappa = 1\times10^{-5}\ \mathrm{m^2\ s^{-1}}$ and $N^2 = 1\times10^{-6}\ \mathrm{s^{-2}}$. The grid spacing is set to 1 km in the horizontal and 2.5 m in the vertical, and the time step is 240 seconds. In regions where the stratification is unstable, κ is increased to $5\times10^{-3}\ \mathrm{m^2\ s^{-1}}$.

The stratification in this toy model is shown at three different times in figures 4.3c to 4.3e. Alternating high and low stratification regions develop with time.

Initially, this is a result of differential mixing; however, at later times the mixing barriers become sharper and start to form filaments due to the extra mixing occurring in regions with unstable stratification.

4.3.2 But what is generating the overturning?

In chapter 3, we saw that western boundary currents can become unstable when crossing the equator as they advect anomalous potential vorticity from one hemisphere into the other. In figure 4.4a, which shows the potential vorticity on the γ^n = 28.04 surface, we can see the advection of positive potential vorticity from the Northern Hemisphere into the Southern Hemisphere, so we may expect to see symmetric instability excited south of the equator. The excitement of the instability is apparent in a region from around 25 km to 600 km south of the equator. Figures 4.4b to 4.4d show the potential vorticity as a function of depth and longitude at the equator, 250 km south and 500 km south, respectively, after 239 days of model integration. At the equator, we see the advection of waters with anomalous potential vorticity into the Southern Hemisphere. At 250 km south we can see the excitement of symmetric instability, and by 500 km south we can see large pools of neutral potential vorticity suggesting the waters here have experienced symmetric instability, with the excitement of symmetric instability still underway at a depth of 3,000 m. In figure 4.4b we also see symmetric instability-like patterns in a region of negative potential vorticity. This suggests these waters with negative potential vorticity were undergoing symmetric instability in the Northern Hemisphere before being advected south of the equator. This also explains the presence of the weak staircases at the equator seen in figure 4.2a. A similar mechanism was proposed by D'Orgeville et al. (2004) in their investigation of deep zonal jets along the equator.

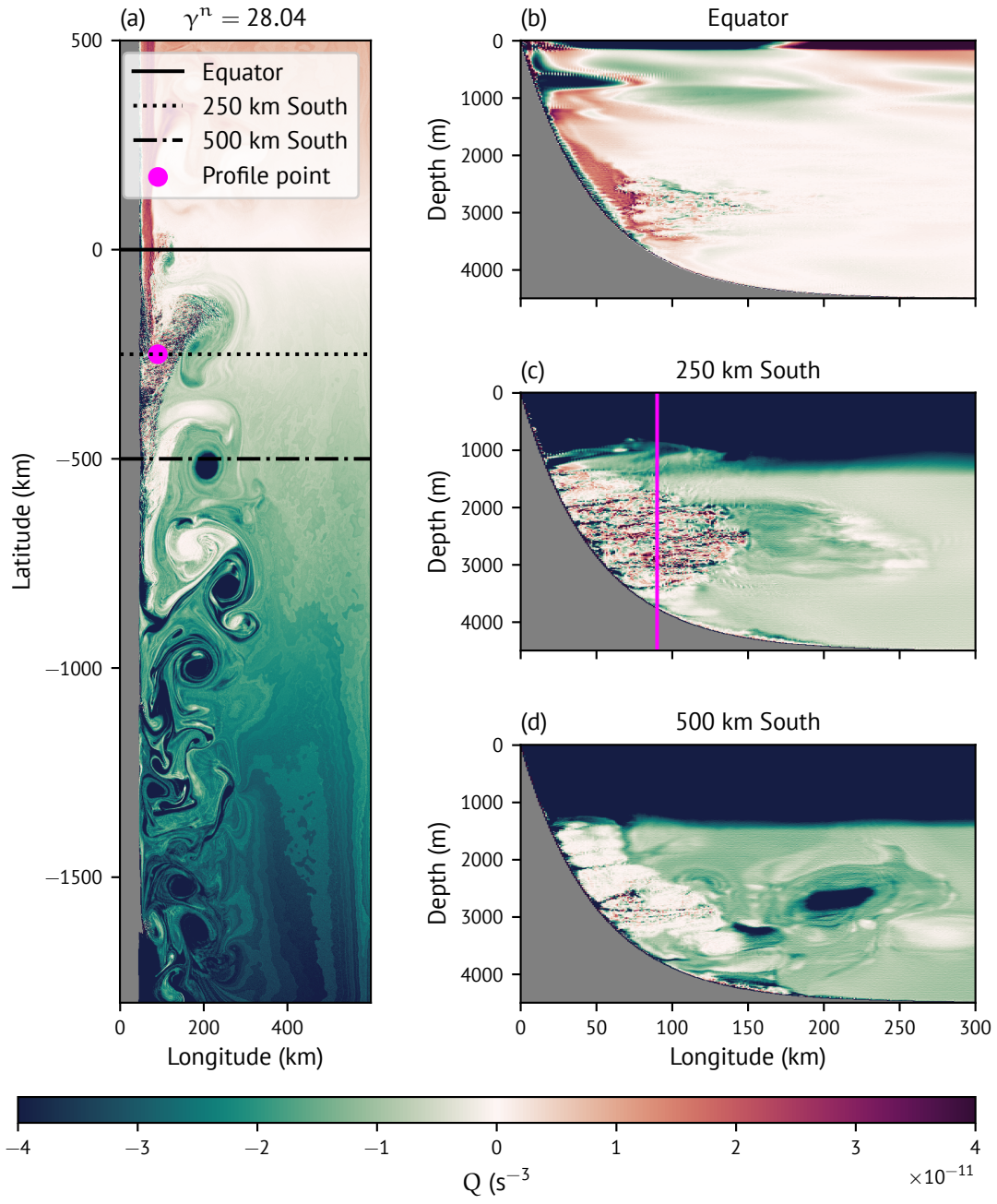


Figure 4.4: Potential vorticity after 239 days of model integration plotted on (a) the $\gamma^n = 28.04$ surface, (b) at the equator, (c) at 250 km south of the equator, and (d) at 500 km south of the equator. Black lines show the latitudes at which sections have been plotted. The magenta line and point indicate the location of the vorticity and density profiles shown in figure 4.3.

4.3.3 Estimating at which latitudes symmetric instability occurs

In the Deep Western Boundary Current, we see the excitement of symmetric instability close to the equator followed by the formation of eddies, unlike in the North Brazil Current where we see the spinning up of large anti-cyclonic eddies followed by the excitement of symmetric instability further away from the equator. This is due to the reduced growth rate of barotropic instability in the deep western boundary current (Edwards and Pedlosky, 1998*b*), meaning that symmetric instability dominates over short time scales. In the North Brazil Current the anti-cyclonic eddies act to reduce the growth rate of symmetric instability further, allowing anomalous potential vorticity to persist whilst the eddies grow (Buckingham et al., 2021*a*).

We can be more quantitative about the latitude at which the instability is forming. There is an e-folding timescale, τ_e, associated with symmetric instability which can be converted into an advective meridional length scale, y with the equation $y = V\tau_e$, where V is a typical meridional velocity. From linear stability theory, we know that for a parallel shear flow, like a deep western boundary current, the timescale of symmetric instability is given by

$$\tau_e \sim \left(\beta y\left(f + \frac{V}{L_x}\right)\right)^{-1/2} \tag{4.2}$$

(Hoskins, 1974), and that for the case of an eddy, such as a North Brazil Current ring, the symmetric instability timescale is

$$\tau_e \sim \left(\beta y\left(f + \frac{2V}{R}\right)\right)^{-1/2} \tag{4.3}$$

(Buckingham et al., 2021*a*). We can then convert these expressions to a meridional

length scale, giving

$$y \sim \sqrt[3]{\frac{VL_x}{\beta}}, \tag{4.4}$$

for parallel shear flows, and for an eddy

$$y \sim \sqrt[3]{\frac{2VR}{\beta}}. \tag{4.5}$$

In the case of the eddying flow, we have assumed the meridional velocity is of a similar order of magnitude to the azimuthal velocity. In both expressions, we have assumed y to be small and only considered terms of the lowest order in y. We can now evaluate the expressions for the latitude of the onset of symmetric instability. For the Deep Western Boundary Current we choose $V \sim 0.2\ \mathrm{m\,s^{-1}}$, $L_x \sim 30$ km and $\beta \sim 2.3 \times 10^{-11}\ \mathrm{m^{-1}\,s^{-1}}$, giving $y \sim 60$ km. For the North Brazil Current rings we choose $V \sim 1\ \mathrm{m\,s^{-1}}$, $R \sim 100$ km and the same value for β, giving $y \sim 200$ km. These predictions of the latitude of instability are of the same order of magnitude as those we see in the numerical models. In the case of North Brazil Current rings, we see instability at around 400 km north, and in the Deep Western Boundary Current, we see instability from around 25 km south of the equator.

Another key difference between the Deep Western Boundary Current and the North Brazil Current is the former's proximity to the bottom boundary layer. For reasons discussed in section 2.4.4 we don't believe that bottom friction or stresses will have a significant impact on the current — the vertical scale of the current is just so much bigger than that of the bottom boundary layer. We hypothesise that the topographic β-effect (vortex stretching induced by the sloping bathymetry) will have a much greater effect on the potential vorticity dynamics than the bottom boundary layer and look forwards to refining and testing this idea in future work.

4.4 Summary

Density staircases are step-like features which can be seen in plots of seawater density against depth, and are common throughout the Earth's oceans. In an idealised model of a deep western boundary current crossing the equator, we see density staircases form. The staircases are generated by overturning cells which are in turn generated by the excitement of symmetric instability as the current crosses the equator. Symmetric instability in cross-equatorial flows is excited due to the advection of anomalous potential vorticity from one hemisphere to another. The stacked overturning cells that generate the staircases are, however, a feature of symmetric instability regardless of what is forcing it, suggesting we may see staircase formation in other symmetrically unstable flows, including when anomalous potential vorticity is induced by frictional torques or diabatic processes. Differences in the latitude of instability between surface intensified western boundary currents and deep western boundary currents can be adequately explained using simple scaling arguments relating the growth rate of symmetric instability to the currents' advective timescales.

It is thought that diapycnal mixing may play an important role in closing the overturning budget of the Atlantic Meridional Overturning Circulation's deep limb. Figures 4.2 and 4.4 clearly show that vigorous mixing is taking place; however, accurately calculating the amount of mixing that is occurring is tricky. This is due to the importance of secondary Kelvin Helmholtz instabilities in transforming water masses. In order to resolve these processes, we would need a model with around 40 times the resolution used here (Bachman and Taylor, 2014), which is computationally infeasible — such a model would require at least 10^4 times more computational resources to run. Simplified two-dimensional models may help in accurately quantifying the induced diapycnal mixing, however.

Density staircases are well documented in the Tropical Atlantic and are often said to form as a result of salt fingering and double diffusive convection (e.g. Schmitt et al. (1987, 2005)). In light of this work, we suggest new insights into mixing in the region could be gained by revisiting existing observations and re-examining the origins of observed staircases.

Chapter 5

Ekman driven symmetric instability in the East Greenland Current

> *And the Aurora was swaying above them in golden arcs and loops, and all around was the bitter Arctic cold and the immense silence of the North.*
>
> Philip Pullman, the Northern Lights

In previous chapters, we explored the excitement of symmetric instability generated by the change in sign of planetary vorticity at the equator. We will now turn our attention to instabilities generated by changing the sign of the potential vorticity of a fluid. In particular, we will be exploring the role of symmetric instability in deep water formation in the high-latitude East Greenland Current.

In section 5.1 we will introduce the East Greenland Current and explore previous works looking at symmetric instability in the Sub-polar North Atlantic. In section 5.2 we will describe an ensemble of 37 idealised two-dimensional numerical models of the East Greenland Current that we use to quantify the water mass transformation rates induced by symmetric instability and secondary instabilities. In section 5.3 we will examine in detail one of the ensemble members, before looking at the results from the whole ensemble in section 5.4. We will summarise our

findings in section 5.6.

This topic is wide-ranging, and the work reported in this chapter can only address some of the key issues, leaving many questions unanswered. We believe that, nevertheless, we are still able to draw meaningful conclusions which contribute to a better understanding of the mixing processes taking place in the East Greenland Current.

5.1 Water mass formation in the Irminger Sea

The Irminger Sea is the region of the North Atlantic that sits between the East Coast of Greenland and the West Coast of Iceland. It has recently been revealed by OSNAP observations to be an important region in the formation of dense North Atlantic Deep Waters which make up the lower limb of the AMOC (Lozier et al., 2019). This finding came as a surprise to many, with most models suggesting deep water formation occurs mainly in the adjacent Labrador Sea. As such, there has been a renewed interest in processes that may enhance deep water formation in the Eastern Sub-polar North Atlantic Ocean (e.g. de Jong and de Steur, 2016; Josey et al., 2019; Le Bras et al., 2022).

The East Greenland Current is the western boundary current of the Irminger sea that flows southwards along the east coast of Greenland. It has a speed of around 20 cm s^{-1} and transports 16 Sv of water (Talley et al., 2011*a*,*b*). The strong baroclinicity of the flow means the current is a hotbed of mesoscale eddy activity (Foldvik et al., 1988). Mesoscale eddies at this latitude are much smaller than those seen in the Tropical Atlantic due to the smallness of the Rossby deformation radius (Chelton et al., 1998). Typical eddy length-scales here are $\sim$ 10 km as opposed to $\sim$ 200 km, as is the case for the North Brazil Current Rings. This leads to interesting interactions between the mesoscale and submesoscale, with the length

scales over which the two regimes are active having significant overlap (Gula et al., 2022).

The established view is that North Atlantic Deep Waters form at high latitudes as a result of surface buoyancy loss, predominantly through air-sea heat fluxes. A recent study by Le Bras et al. (2022) challenges this view. They study the effect of strong down front winds which blow along the East Greenland Current, often referred to as "barrier wind events", and estimate that the Ekman buoyancy flux induced by these winds can be as much as four times stronger than the buoyancy flux resulting directly from heat loss to the atmosphere (the mechanism by which winds can extract buoyancy from a flow was described in section 2.1.2). The resulting buoyancy loss can lead to the excitement of symmetric instability which is capable of generating mixing and creating a low potential vorticity layer below the convectively mixed layer (Taylor and Ferrari, 2010; Yu et al., 2021). The winds that drive these Ekman buoyancy fluxes occur frequently during winter and spring, typically lasting around 3 days and exerting maximal stresses of up to 2 $\mathrm{N\,m^{-2}}$ on the sea surface (Le Bras et al., 2022). The mean stratification in the deep wintertime mixed layer is also particularly conducive to the excitement of submesoscale instabilities (Brannigan et al., 2015).

The idea of Ekman induced symmetric instability being an important mechanism in the formation of deep waters in the Sub-polar North Atlantic is not a new one. Straneo et al. (2002) found that wind-driven Ekman buoyancy fluxes over the Labrador Sea can be around a third of the size of the air-sea buoyancy flux, and concluded that symmetric instability should be taken into account when modelling deep water formation in the region.

Spall and Thomas (2016) investigate the effect of down front winds in an idealised model of the East Greenland Current. They integrate both two-dimensional and three-dimensional hydrostatic models, with a horizontal grid spacing of 500 m

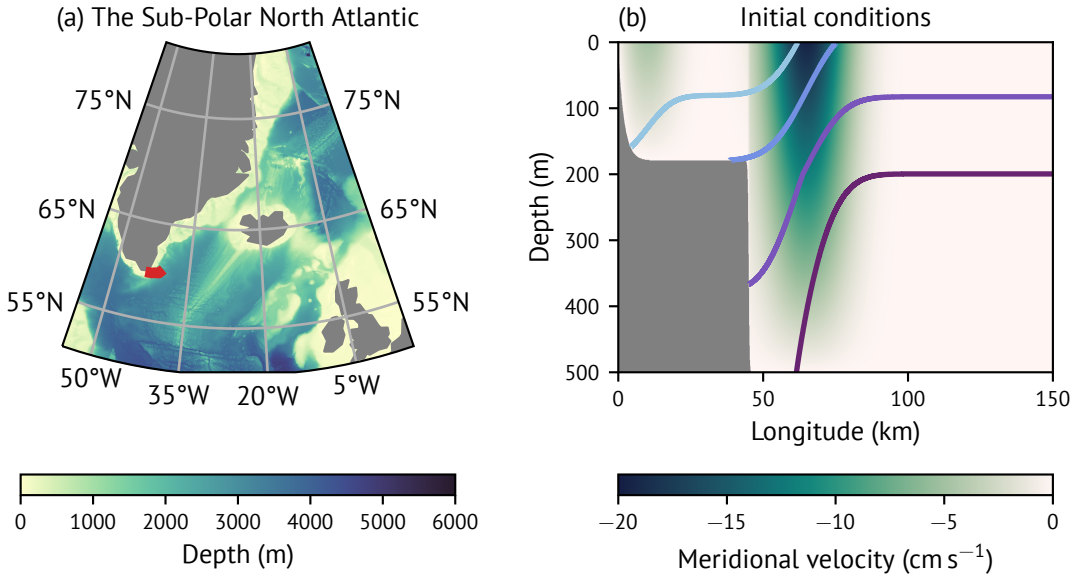


Figure 5.1: (a) The Sub-polar North Atlantic. The red line highlights the region where the observations which "inspired" the initial conditions used in the model were taken. (b) The meridional velocity used to instantiate model integrations, overlain with the isopycnals which denote the lower boundaries of each of the water mass classes we use in subsequent analysis (see figure 5.6 & table 5.1).

and a vertical grid spacing of 1 m. They force their models with a uniform meridional wind stress which is ramped up over seven days and then held constant for the remaining thirteen days of model integration. In their models, they observe an Ekman buoyancy flux that sets the potential vorticity to near zero, alongside baroclinic instability. These two processes together act to produce water mass transformations, with baroclinic instability greatly enhancing the transformation rates.

Other field and modelling campaigns have investigated the role of Ekman driven symmetric instability in various boundary current and frontal systems. Thomas et al. (2013) observed symmetric instability in the Gulf Stream under down front winds and found a competition between destratification of the mixed layer by convection and restratification resulting from symmetric instabilities. Similar effects

were observed by D'Asaro et al. (2011) in the Kuroshio, and conditions conducive to symmetric instability have been found in observations of the Antarctic Circumpolar Current (Taylor et al., 2018).

The work of Le Bras et al. (2022) raises questions about how much water mass transformation is driven by down front wind events, and whether these highly seasonal events could be a source of AMOC variability. These questions are incredibly difficult to answer with sparse observations, and so here we will use idealised models to fill observational gaps. Our results could also be used to form the basis of a parameterisation for mixing induced by down front wind events (although we will not attempt to do this here). The work of Spall and Thomas (2016) lays the foundations for addressing the above questions; however, their study design means it is only able to partially answer them. Their hydrostatic models are too coarse to provide a truly reliable estimate of the mixing induced by symmetric instability. A non-hydrostatic model with a higher resolution is required to resolve the secondary shear instabilities which are known to be important in generating mixing (Taylor and Ferrari, 2009).

Although Spall and Thomas (2016) set out to model the same barrier wind events investigated by Le Bras et al. (2022), they force their model with a wind stress which is held constant after the first seven days of model integration. This means both potential vorticity and buoyancy are constantly being extracted from the flow, meaning their models will not reach a steady state; rather, instability will constantly be excited. This means estimates of mixing at later times in their integrations may be either overestimates or underestimates, depending upon whether the pre-conditioning by the wind stress at earlier times enhances or suppresses subsequent mixing. To estimate the effect of a wind event on mixing, we must model it as just that — an isolated event, with a wind stress which is ramped up and down to some characteristic value over a characteristic period of time.

5.2 A two-dimensional model of the East Greenland current

In section 3.2.1 we used a two-dimensional model of the North Brazil Current to probe symmetric instability in a "clean" environment, free from the noise of baroclinic and barotropic instabilities. In this chapter, we will use similar two-dimensional models to explore symmetric instability in the East Greenland current.

We use a non-hydrostatic configuration of the MITgcm (Marshall et al., 1997) to integrate an idealised two-dimensional model of the East Greenland current that is symmetric (periodic) in the along-stream direction. The domain is 150 km wide in the horizontal cross-stream direction and 500 m deep. The horizontal and vertical grid spacings are set to 25 m and 1 m, respectively. The resolution is set to be high enough to ensure that the Richardson number is sufficiently small for Kelvin-Helmholtz instabilities to be resolved. This is because Kelvin-Helmholtz instabilities are known to be important for obtaining reliable estimates of the amount of diapycnal mixing that is occurring (Griffiths, 2003*b*; Yankovsky and Legg, 2019). The time step is set to 2 seconds and the model is integrated for a total of 21 days. The model is sited on an f-plane with f set to 1.26×10^{-4} s^{-1}, corresponding to a latitude of 60°N.

At the surface, a rigid lid boundary condition is employed, with the lateral and bottom boundaries set to be free-slip. The model has sloping bathymetry, which can be seen in figure 5.1b. The model is initialised in thermal wind balance, with the velocity field and density profiles shown in figure 5.1b. Both of these fields are based on observations from the OSNAP array (Le Bras et al., 2022).

The model is forced using a time-varying along stream wind stress. The stress

is spatially uniform and temporally Gaussian, taking the form

$$\tau_y = \tau_0 e^{-(t-t_{mid})^2/2\delta_t^2}, \tag{5.1}$$

where τ_0 is the maximum wind stress, t_{mid} is the time at which the wind stress peaks and δ_t is the duration of the wind event. For the reference integration, $\tau_0 = -0.5\,\mathrm{N\,m^{-2}}$ and $\delta_t = 2.5$ days. For each of the model integrations t_{mid} is set to 10.5 days. The along-front wind stress leads to a steepening of isopycnals and reduction in potential vorticity which may eventually lead to the excitement of symmetric instability, and in extreme cases, pure gravitational instability. To investigate how different wind forcing affects water mass formation and transformation rates, we also integrate an ensemble of simulations using ten different values of τ_0 ranging linearly from $0\,\mathrm{N\,m^{-2}}$ to $-0.75\,\mathrm{N\,m^{-2}}$ and five different values of δ_t ranging linearly from 0 days to 5 days. This gives a total of 37 different ensemble members.

As in the previous models, a linear equation of state is used, with a reference density of $1{,}027\,\mathrm{kg\,m^{-3}}$, a thermal expansion coefficient of $2 \times 10^{-4}\ \mathrm{K^{-1}}$ and no salinity tracer. The thermal diffusion coefficient is set to $1 \times 10^{-5}\ \mathrm{m^2\,s^{-1}}$. A second order-moment Prather advection scheme with a flux limiter is employed (Prather, 1986). Momentum dissipation is provided by an adaptive biharmonic lateral Smagorinsky viscosity and a vertical Laplacian viscosity of $4 \times 10^{-4}\ \mathrm{m^2\,s^{-1}}$ (Smagorinsky, 1963; Griffies and Hallberg, 2000).

5.3 The reference integration

For the reference integration τ_0 is set to $-0.5\,\mathrm{N\,m^{-2}}$ and δ_t to 2.5 days. Figure 5.5a shows how the wind stress in the model evolves. This wind stress is lower than the typical peak wind stresses seen over the East Greenland Current during Wintertime (typically around $-2\,\mathrm{N\,m^{-2}}$) but is not atypical for less extreme wind events

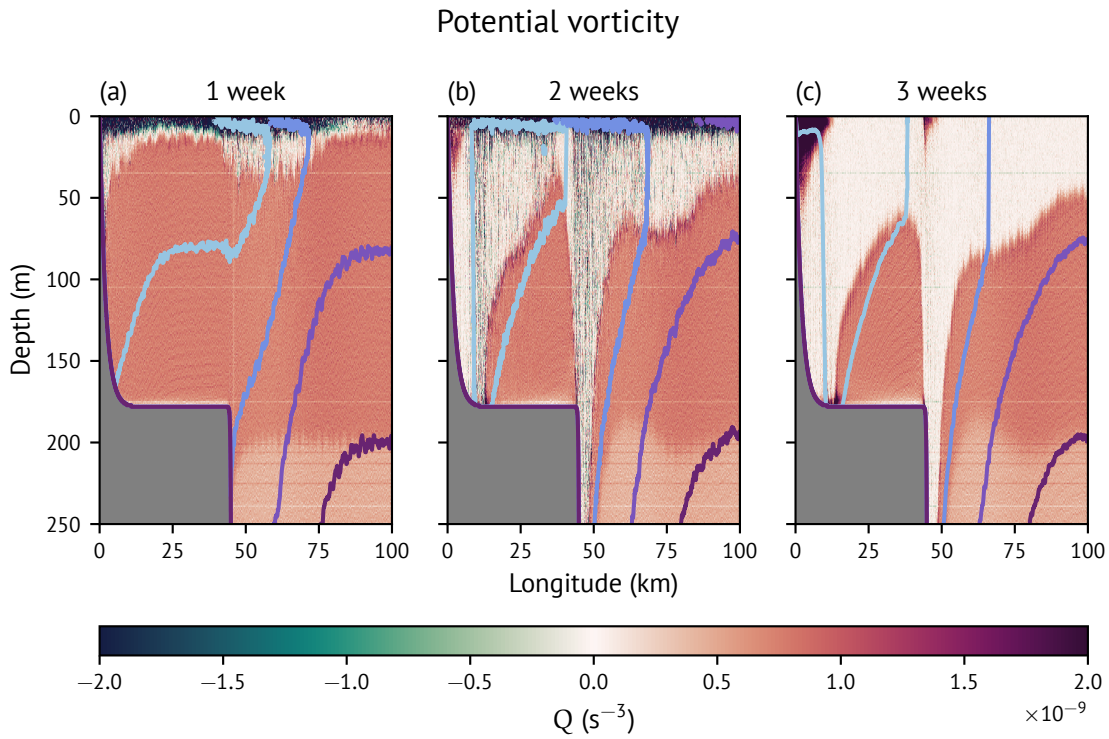


Figure 5.2: Potential vorticity after (a) 1 week, (b) 2 weeks and (c) 3 weeks of model integration in the reference integration, overlain with isopycnals corresponding to the lower boundaries of density classes 0 to 3 (see figure 5.6 & table 5.1).

(Moore et al., 2008; Harden and Renfrew, 2012; Le Bras et al., 2022). The duration is similar to the wind events seen in observations. Wind stresses in the ensemble of models considered here were not increased above -0.75 N m^{-2} as the model time-step required to ensure stability made the integrations too computationally intensive to perform.

Figure 5.2 shows the potential vorticity in the reference integration, overlain with isopycnal contours after one week, two weeks and three weeks of model runtime. In panel (a) we see how the down front wind stress has induced an Ekman transport of surface waters towards the shelf, leading to a steepening of isopycnals and generating unstable stratification at the surface (where dense isopycnals lie over lighter ones). This will generate strong mixing in the region of unstable

stratification and some weaker mixing directly below it.

A week later, several days after the wind-forcing has peaked, we see a region of low potential vorticity now stretches to the bottom of the inner coastal shelf. Some negative potential vorticity remains, meaning the flow has not yet fully equilibrated. Between around 20 m and 50 m of depth, the isopycnals become very steep. These waters are stable to gravitational instability but have small magnitude negative potential vorticity arising from the strong shear and baroclinicity of the flow. These waters are susceptible to symmetric instability and produce mixing in the waters below the convectively mixed layer.

Finally, after three weeks, we see near zero potential vorticity throughout the upper 75 m of the shelf and shelf-break region. The majority of the negative potential vorticity has now gone, implying the flow has equilibrated following the wind event and reached a new (almost) steady state. Note how vertical the isopycnals are in the low potential vorticity layer, well below the convectively mixed surface layer.

The net effect of the winds, the gravitational instability[1] and the symmetric instability is to set the potential vorticity of the flow to zero by modifying its stratification — this effect was first demonstrated by Haine and Marshall (1998). Figure 5.3 shows snapshots of the vertical buoyancy gradient over time. We can see how regions of low vertical stratification in figure 5.3c line up remarkably well with the regions of low potential vorticity in 5.2c. In figures 5.3a and b, we see a shallow reservoir of gravitationally unstable waters towards the surface of the model; however, waters outside this region possess near zero stratification after two weeks of integration and almost exactly zero stratification after three weeks. Initially, Ekman transport leads to a reduction in the stratification by steepening the isopycnals. Upon becoming sufficiently steep symmetric instability is excited.

[1] which is really just an extreme case of symmetric instability as we saw in chapter 2

The excitement of symmetric instability leads to slantwise convection — overturning along isopycnals. This, in turn, leads to the excitement of Kelvin Helmholtz instability in the across-stream plane, which produces diapycnal mixing. This mixing reduces the isopycnal slope until the potential vorticity is approximately zero. Due to the high latitude, isopycnals can become very steeply sloping before becoming symmetrically unstable[2], which means the vertical stratification ($\partial_z b$) of the zero potential vorticity state is very low, an effect also demonstrated by Haine and Marshall (1998). Furthermore, the billows generated by Kelvin Helmholtz instability can become susceptible to further gravitational instabilities which act to erode the vertical stratification further.

That the instability sets the vertical stratification to zero contrasts with studies of the Kuroshio and Gulf Stream, where it is found that symmetric instability acts to restratify the water column (D'Asaro et al., 2011; Thomas et al., 2013). The finding, however, is consistent with observations from the Sub-polar North Atlantic (Le Bras et al., 2022) and the theory of Haine and Marshall (1998). We hypothesise that these differences stem from the differences in planetary vorticity at high and mid latitudes, and the gravitational instability of the Kelvin Helmholtz billows we resolve here. Further work is required to confirm this is indeed the case.

In all, this makes discerning the contributions to mixing from the different "flavours" of symmetric instability and its secondary instabilities difficult. Taylor and Ferrari (2010), and Yu et al. (2021) talk of low potential vorticity layers with near zero potential vorticity but non-zero stratification being generated by wind events such as these — the low potential vorticity layer being distinct from, and deeper than the convectively mixed layer. The horizontal model resolution of Taylor and Ferrari (2010) is a factor of ten higher than ours, allowing them to bet-

[2] If we assume $Q \approx f\partial_z b - (\partial_x b)^2/f$, take $f \sim 10^{-4}$ and $\partial_z b \sim 10^6$, and note that $\tan \Phi_{iso} = \partial_x b / \partial_z b$, we can show Φ_{iso} must be greater than approximately 5° for symmetric instability to occur at this latitude. This is a 1 in 10 gradient which is incredibly steep in oceanic terms.

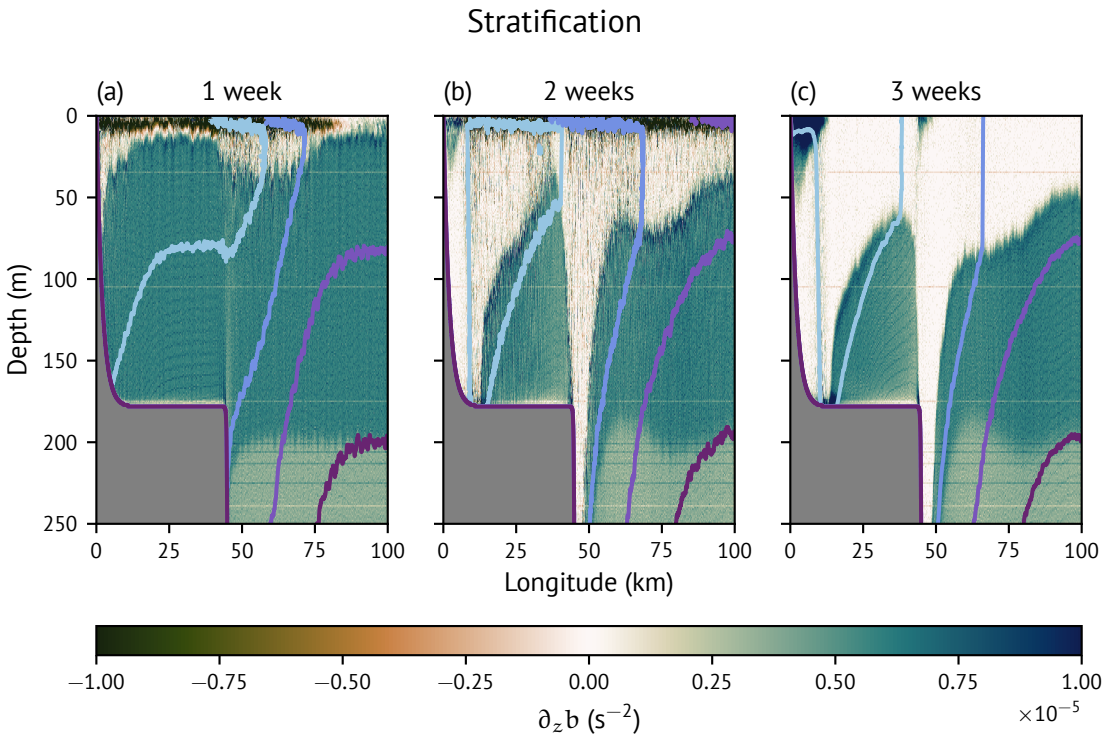


Figure 5.3: Stratification ($\partial_z b$) in the reference integration after (a) 1 week, (b) 2 weeks and (c) 3 weeks of model integration, overlain with isopycnals corresponding to the lower boundaries of density classes 0 to 3 (see figure 5.6 & table 5.1).

ter resolve the steeply slanted isopycnals which give a small but non-zero vertical stratification. A key limitation of our model (and the ensemble) is that it struggles to differentiate the low potential vorticity layer from the convectively mixed layer, with both having near-zero stratification.

Despite it being difficult to separate the low potential vorticity layer from the convectively mixed layer, we can still try to distinguish between the regions where gravitational instability and symmetric instability dominate the dynamics. Figure 5.4 shows the total number of grid points susceptible to gravitational and symmetric instabilities as a function of depth and time in the reference integration. We see that gravitational instability is dominant in the surface layers. From around 20 m and lower, symmetric instability is more active. This ties in well with our inter-

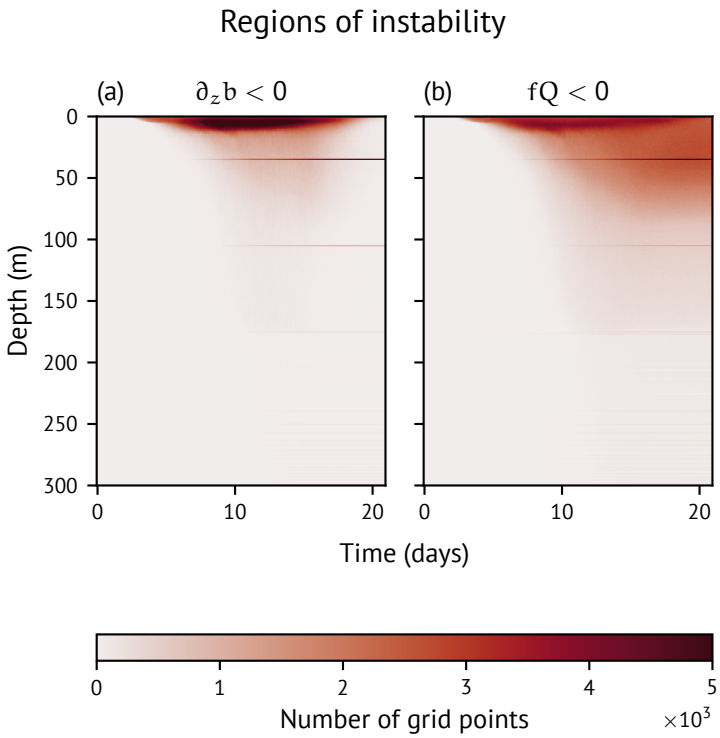


Figure 5.4: Plot showing the total number of grid cells susceptible to (a) gravitational instability and (b) symmetric instability as a function of depth and time.

pretation of the potential vorticity and the density contours seen in figure 5.2.

We will now consider the effect of both symmetric and gravitational instabilities on the depth of the well-mixed layer. We will define the mixed layer depth as the depth at which the density drops by 0.05 kg m^{-3} relative to the value at the surface. This layer typically includes both the upper convectively mixed layer and the deeper low potential vorticity layer. Whenever we refer to the mixed layer hereafter, we mean this well-mixed region. Figure 5.5b shows how the mean (solid orange line) and the maximum (dashed orange line) mixed layer depth evolves. We see that the maximum mixed layer depth increases almost monotonically, reaching the base of the model after around 11 days. This suggests it may have been useful to increase the model's maximum depth; however, this was not possible due to computational constraints. The mean mixed layer depth also undergoes a net

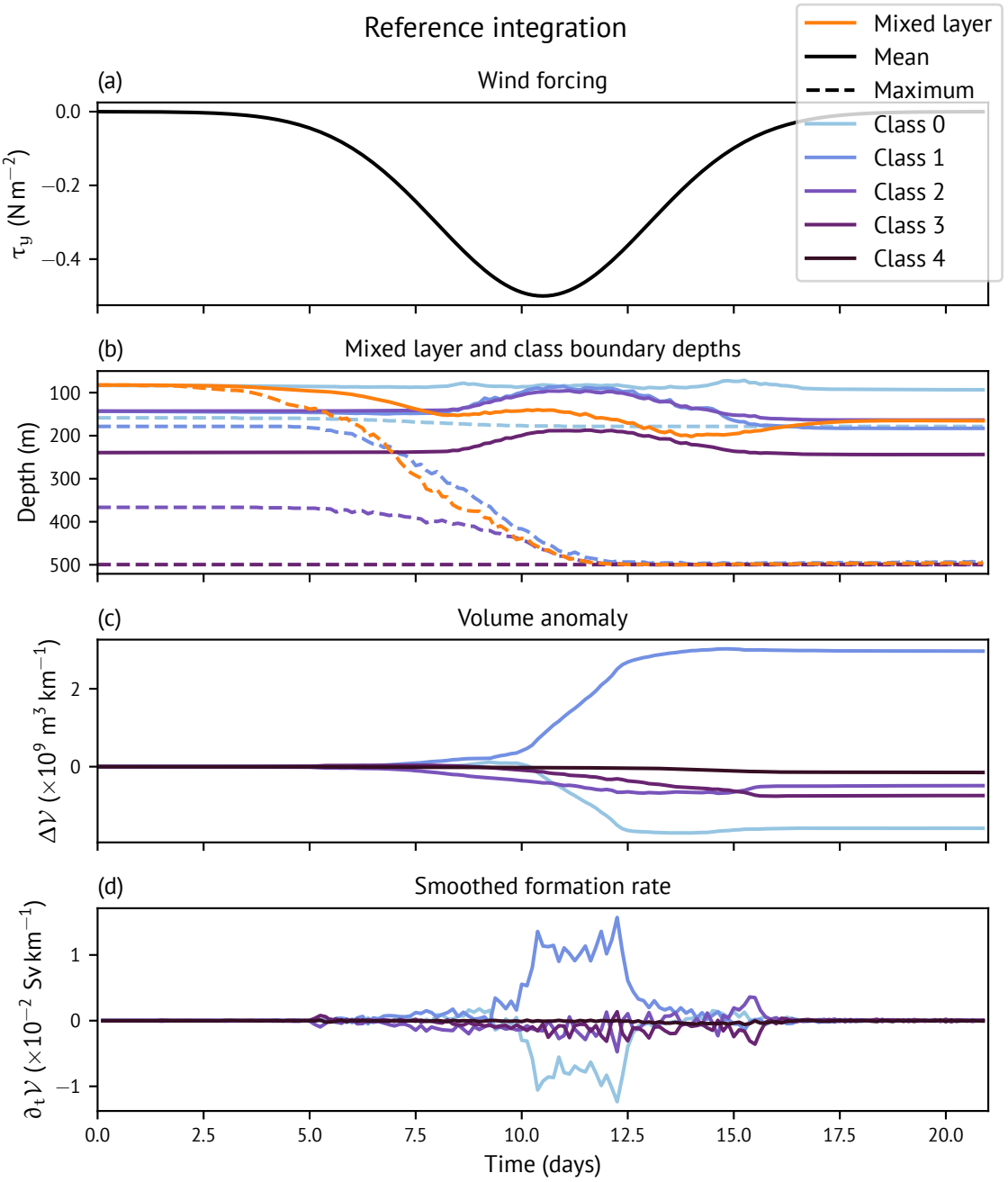


Figure 5.5: Time series of (a) Wind forcing, (b) mixed layer depth (orange) and the lower boundary of water mass class depths (shades of blue), (c) volume anomaly and (d) water mass formation rates from the reference integration. Solid lines in panel (b) represent zonally averaged depths, and dashed lines represent maximum depths. Shades of blue correspond to water mass classes.

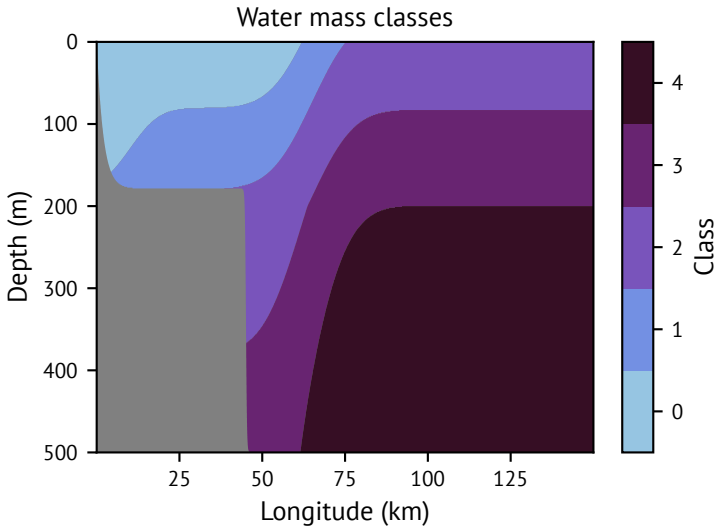


Figure 5.6: Water mass classes at model instantiation.

deepening, from around 95 m to 150 m.

The definition of the mixed layer depth employed here is somewhat arbitrary and so in figure 5.5b, we show the mean and maximum depths of several isopycnals over time. They are labelled as classes 0 to 3 and correspond to the lower boundaries of the different water mass classes shown in figure 5.6 and defined in table 5.1. We see that for classes 1 & 2 there is a large change in the maximum depth, with these isopycnals now reaching the base of the model; however, The changes in the mean depths are much more modest. Focussing on the mean depth of classes 1 & 2 we see there is a shallowing of the isopycnal depth as the wind event gets underway, followed by isopycnal deepening. This is caused by Ekman transport forcing the upwelling of waters within these classes. The isopycnals then return to slightly deeper depths following the wind event as a result of diapycnal mixing altering the density structure.

The effect of mixing on the different water mass classes can be examined through an analysis of the model's volume budget. Figure 5.5c shows the change in volume of each water mass class over time. We see that there is a huge increase in the

amount of class 1 shelf-break waters and a decrease in the volume of waters in classes 0, 2 & 3. We can see that the increase in class 2 waters is largely driven by densification of the lightest waters, and to some extent the lightening of dense waters that sit below. The class 4 deep waters remain relatively unmixed. An attempt was made to calculate the instantaneous rate of change of the volumes in each class (the water mass formation rate); however, the time series were too noisy to be able to draw any meaningful conclusions. Instead, in figure 5.5d we show the formation rate calculated by differentiating the volume anomaly over time, giving a much smoother signal. We have expressed the units in $\mathrm{Sv\,km^{-1}}$ — this model is a two-dimensional model, so to get an estimate of the transformation rates across the whole length of the East Greenland Current, one should multiply the value by $\sim 10^2$ km.

We see that the water mass formation rates are greatest in classes 1 & 0 — this is unsurprising given they are in the closest proximity to the forcing. In the lightest two classes the formation rates first peak at a similar time to the wind-forcing, whereas in the deeper classes, there is a small lag of around a day or so. There is then a subsequent peak at around 12.5 days in the formation rates of the class 1 & 0 waters, produced by the delayed mixing with water masses in the densest classes. The message from the volume anomaly and formation rate time series is

Class	γ^n ($\mathrm{kg\,m^{-3}}$)		Name
	Lower boundary	Upper boundary	
0	26.92	None	shelf waters
1	26.98	26.92	shelf-break waters
2	27.05	26.98	upper intermediate waters
3	27.1211	27.05	lower intermediate waters
4	None	27.1211	deep waters

Table 5.1: Density bands use to define water mass classes 0 to 4. Water mass class definitions are based on the areas they occupy at model instantiation.

clear, however — symmetric instability and subsequent secondary instabilities are leading to densification of shelf waters and lightening of intermediate waters by mixing them with shelf-break waters. This leads to an increase in the volume of waters in the shelf-break density class.

Given that Spall and Thomas (2016) show that baroclinic instability enhances the water mass transformation produced by symmetric instability, it is pertinent to question how reliable the water mass transformation calculations presented here are, with two-dimensional models unable to represent baroclinic instability. The ensemble of simulations is too computationally expensive to run over a fully three-dimensional domain; however, in future work, it would be interesting to examine the water mass transformation rates in a three-dimensional configuration of the reference integration.

5.4 An ensemble of model simulations

The ensemble of model simulations is forced with wind stresses ranging in strength from 0 $\mathrm{N\,m^{-2}}$ to -0.75 $\mathrm{N\,m^{-2}}$ and with a duration of between 0 days and 5 days. It is useful to define the time-integrated wind stress which is given by

$$\tau_{\mathrm{int}} = \int_{t=0}^{t_{\mathrm{end}}} \tau_y(t;\tau_0,\delta_t)\mathrm{d}t \tag{5.2}$$

and has units of $\mathrm{N\,s\,m^{-2}}$. This is a measure of the total wind-forcing experienced by an ensemble member and combines the original two dependent variables into a single scalar.

For each ensemble member, we calculated the change in the mean mixed layer depth[3] between the start and end of the integration. This is plotted as a function

[3]Defined as before, as the depth at which the density changes by 0.05 $\mathrm{kg\,m^{-3}}$ relative to the surface density.

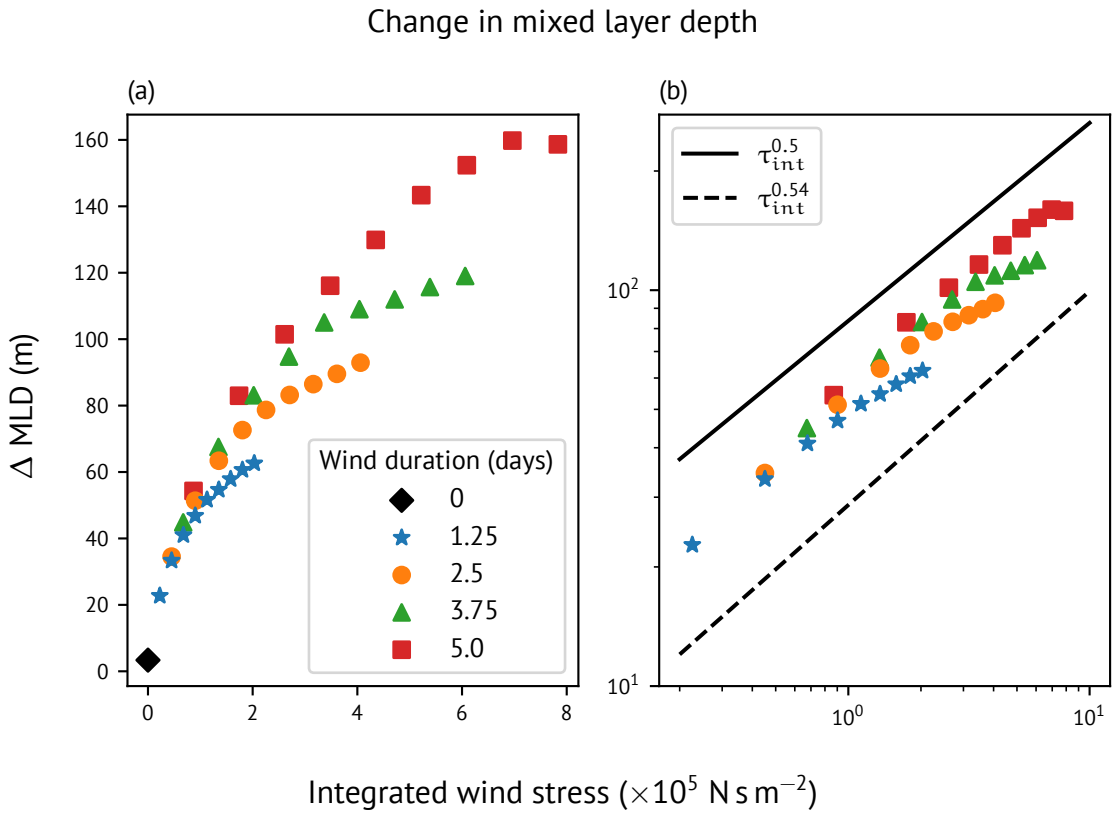


Figure 5.7: (a) Change in the mixed layer depth from the start to the end of each model integration, plotted as a function of integrated wind stress. Shapes and colours of markers identify the duration of the wind event. (b) As for panel (a), but plotted on logarithmic axes. Solid line shows $\tau_{int}^{0.5}$ (the theoretical power law) and dashed line $\tau_{int}^{0.54}$ (the power law found by least-square regression)

of the time-integrated wind stress in figure 5.7a. Changes in the mixed layer depth behave largely as expected — the larger the integrated wind stress the deeper the mixed layer. Interestingly, the change in mixed layer depth depends on both the maximal wind stress and the wind event duration. There are signs that for a given wind event duration there is a limit on the change in mixed layer depth, with increasing wind strengths leading to no further changes. This suggests the duration of a wind event is a primary control of how deep mixing can occur. Verification of this requires modelling with even larger wind stresses, which is computationally

challenging. Furthermore, with the mixed layer often stretching to the model floor (see e.g. figure 5.5b), bathymetry may be affecting the relationship.

Taylor and Ferrari (2010) propose a scaling for the depth of the low potential vorticity layer generated during down front wind events. Assuming the only forcing comes from winds and that the initial depth of the low potential vorticity layer is zero, the scaling can be summarised as

$$\frac{dH^2}{dt} \propto B_{wind} \tag{5.3}$$

where H is the depth of the low potential vorticity layer and B_{wind} is the Ekman buoyancy flux induced by the down front winds, and is given by

$$B_{wind} = -\frac{\tau_y \partial_x b}{\rho_0 f} . \tag{5.4}$$

Integrating equation 5.3 we find that

$$H(t = t_{end}) \propto \tau_{int}^{1/2} . \tag{5.5}$$

As noted already, the low potential vorticity layer in our models is almost indistinguishable from the mixed layer, due to the low stratification of the low potential vorticity layer. If we assume the change in mixed layer depth is a result of the expansion of the low potential vorticity layer we would expect changes in mixed layer depth to scale with the square root of the integrated wind stress. In figure 5.7b we show the change in mixed layer depth plotted against the integrated wind stress on logarithmic axes. Performing a least squares regression on the ensemble data, we find that the change in mixed layer depth scales with τ_{int} to the power of 0.54, which is remarkably close to the value of 0.5 predicted by idealised theory. Lines showing the 0.5 and 0.54 power laws are also shown on the axes.

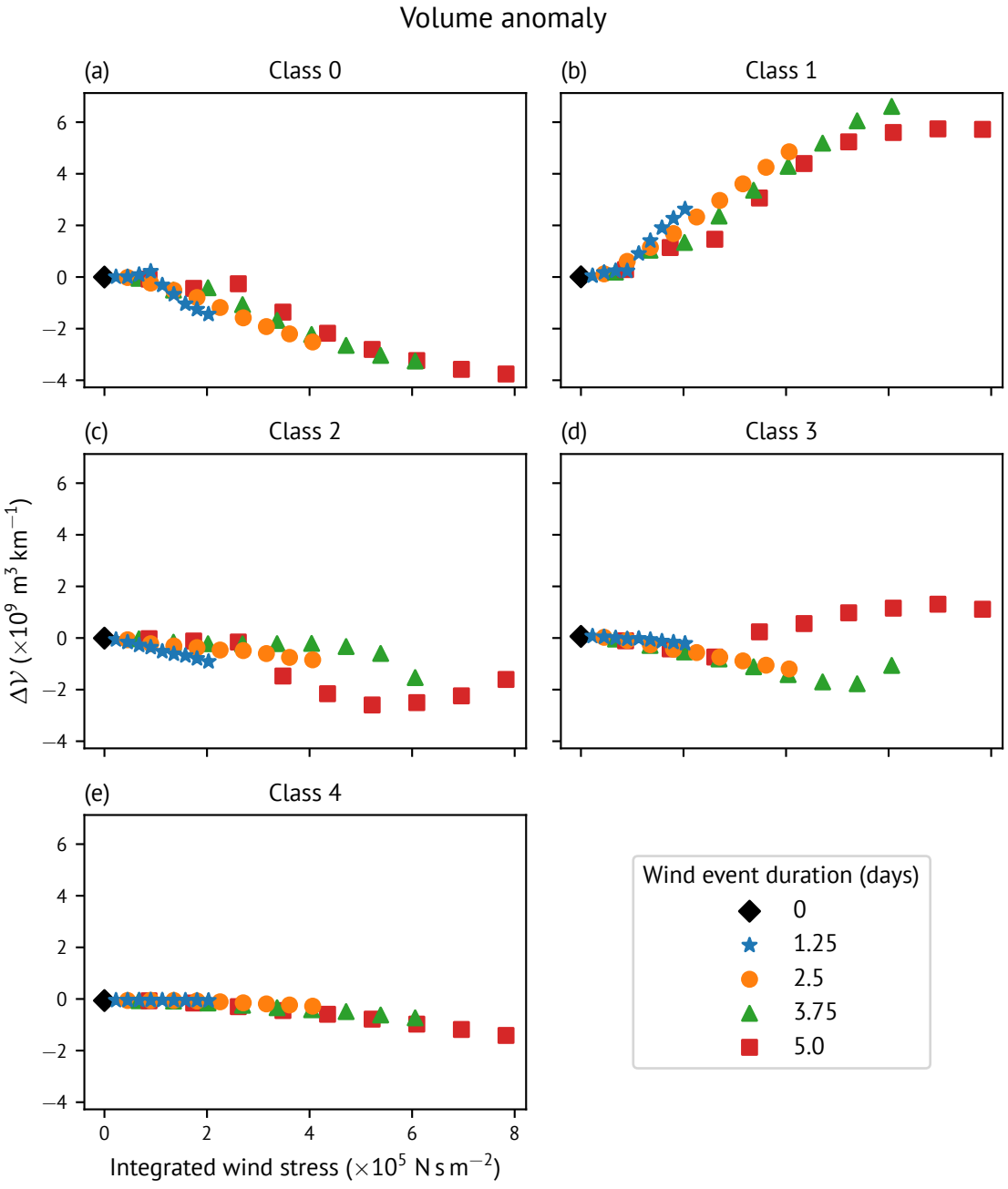


Figure 5.8: Volume anomaly at the end of each model integration for water mass classes 0 to 4 (a) to (e), plotted as a function of integrated wind stress. Shapes and colours correspond to different wind durations.

Next, we look at the volume anomaly in each of the previously defined water mass classes at the end of each model integration — figure 5.8 shows this plotted as a function of the time-integrated wind stress. We can see that, generally, the integrated wind stress is a reasonable predictor of the volume anomaly in each class. The primary exceptions to this are the high-stress five-day wind events. During these events, the volume anomalies in classes 2 & 3 deviate from the patterns seen in the shorter duration wind events. The longer wind events produce deeper mixing, which means the winds generate more mixing between the denser (and deeper) class 2 & class 3 water masses.

In figure 5.9, we plot the maximum and minimum water mass formation rate as a function of the time-integrated wind stress, for each water mass class in each ensemble member. The colours and shapes of the markers indicate the duration of the wind events, with filled markers corresponding to maximal formation rates and unfilled markers corresponding to minimal formation rates. In class 0 the maximum formation rate is approximately zero. For integrated wind stresses of above $2\,\mathrm{N\,s\,m^{-2}}$, in classes 0 and 1, the minimum and maximum formation rates, respectively, saturate at around $1.5 \times 10^{-2}\,\mathrm{Sv\,km^{-1}}$. This implies a maximum mixing rate between these two water mass classes exists. In class 1, the minimum formation rate is approximately zero for all integrated wind stresses. The exception to this is for large wind stresses during five-day wind events. During these events, the minimum formation rate becomes large and negative, and there is a similar uptick in the maximum formation rate of class 2 waters. This implies that during longer wind events there is a transformation between the class 1 & 2 waters, reinforcing the idea that longer wind events lead to the mixing of deeper waters.

In general, formation rates of class 2 waters are much more modest, as would be expected given their reduced proximity to the source of the buoyancy forcing. The main exception to this is the negative formation rate at high integrated

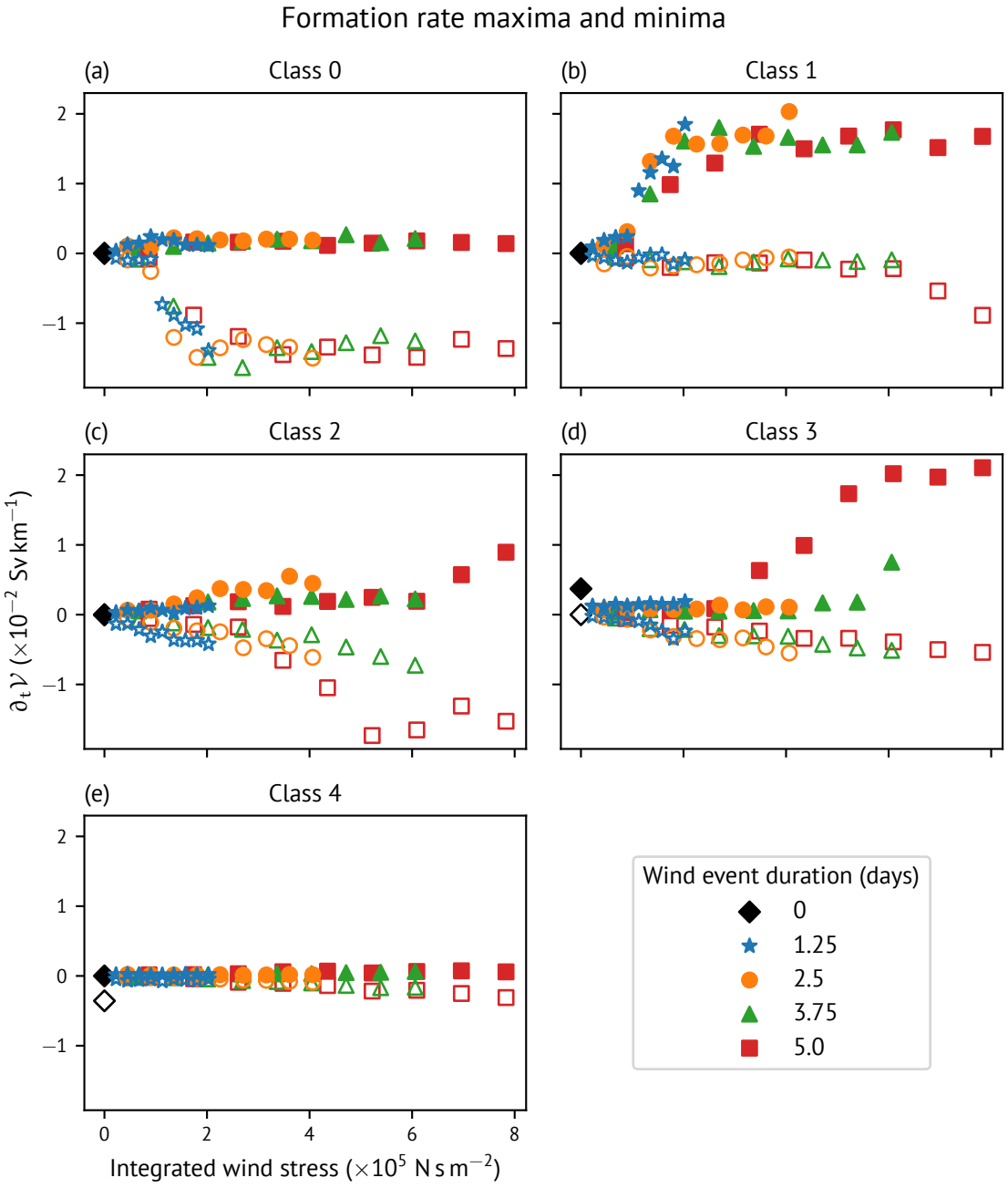


Figure 5.9: Maximum and minimum water mass formation rates for water mass classes 0 to 4 (a) to (e) plotted as a function of integrated wind stress. Filled shapes give maximum and unfilled shapes give minimum water mass formation rates. The duration of the winds is given by the shape and colour of the points.

wind stresses, balanced by the formation of class 1 & class 3 waters. At high wind stresses during the longer wind events, there are large formation rates of class 3 waters, which saturate at approximately 2×10^{-2} Sv km^{-1}. Regardless of wind stress, the formation rates of class 4 waters are close to zero, as expected for deep waters.

It is hard to discern patterns in the density classes at which waters are formed or destroyed. We suspect it is to do with which isopycnals outcrop and which do not, and where the isopycnals outcrop relative to the regions of negative absolute vorticity. For instance in figure 5.2 we see the class 1 isopycnal outcrops directly over the region of negative absolute vorticity where symmetric instability is enhanced. The mixing entrains waters from calsses 0 and class 2 leading to the net formation of class 1 waters. Calculating water mass transformations in density space would help to better ascertain if this is the case or not. We would then be able to identify isopycnals with convergent water mass transformation rates and track their outcroppinng locations relative to regions of negative absolute vorticity.

5.5 Open questions

5.5.1 Can the effect of the instability be effectively parameterised?

In figure 5.2 we see that the regions of enhanced mixing resulting from symmetric instability have a horizontal length scale of around 25 km. As such it makes little sense to attempt to parameterise the process in models with a lower resolution than this. The next generation of coupled climate models with have resolutions of around 5 km to 10 km, however, will be unable to directly resolve the mxing induced by symmetric instability resulting from down front winds and so in these models parameterisations will be required (Chang et al., 2020). Bachman et al. (2017) propose a parameterisation which uses a vertical viscosity to mix mo-

mentum, buoyancy and tracers; a vertical buoyancy flux to represent mixed layer deepening; and a turbulent tracer diffusivity to represent along isopycnal mixing in frontal regions destabilised by down front winds. They find their parameterisation compares favourably with the KPP parameterisation which does not take into account shear instabilities (Large et al., 1994). A limitation of their parameterisation is its reliance on resolving fronts well enough to infer the destabilising Ekman buoyancy flux induced by the wind stress. In the high latitudes where the Rossby deformation radius is minimal, it's not clear that a 10 km or even 5 km resolution model will adequately resolve the East Greenland buondary current and frontal system. Future work should aim to ascertain at what resolution the parameterisation of Bachman et al. (2017) is able to reproduce the effect of symmetric instability in fronts at high latitudes, if it is able to reproduce them at all. It is not clear that the parameterisation will work, having been designed to represent the restratifying effects of symmetric instability, whereas here we see symmetric instability destratifying the water column.

5.5.2 How do symmetric and baroclinic instabilities interact?

This work has shown that although down front winds can lead to substantial mixing over short timescales, when averaged out over the course of a year the mixing may become insignificant. However, that isn't to say that the mixing can be neglected. We hypothesise that symmetric instability dominates the frontal dynamics in the East Greenland Current during down front wind events. Following these events we hypothesise there is a slower response, resulting from baroclinic instability. The short timescale response to the wind events is the production of a deep mixed layer with almost zero stratification. The surface waters, however, remain highly baroclinic with strong lateral buoyancy gradients. This may precondition the mixed layer, making it susceptible to baroclinic instability which will act over

longer timescales. In particular this may enhance the export of freshwaters away from the shelf into the interior of the basin (with the exchange potentially restratifying waters both in the boundary and interior of the basin), and lateral mixing rates of temperature and salinity. This slow response may be relevant over seasonal timescales, however, relies on the initial preconditioning of the mixed layer by the action of symmetric instability. The idealised, unforced simulations of Stamper and Taylor (2017) support the idea of there existing a short timescale symmetric and long timescale baroclinic response to down front wind events, with the added possibility of hybrid mixed symmetric and baroclinic instabilities growing over intermediate timescales, with growth rates comparable to the "pure" symmetric or baroclinic modes.

To investigate this hypothesis further, we are currently performing simulations using a 200 m resolution, meridionally periodic, but fully three-dimensional variation of the two-dimensional model presented here. We integrate this model for twelve weeks and subject it to either the winds used in the reference integration or no winds at all. The three-dimensional setup enables the generation of baroclinic instability (Stone, 1966) and allows us to compare the action of the baroclinic instability with and without mixed layer preconditioning by symmetric instability. Key variables that will be examined are eddy kinetic energy and (turbulent) salinity fluxes, as well as those anlysed in the study presented here. Understanding interactions between symmetric and baroclinic instabilities is key to building a clearer picture of the processes at play both during and following these wind events and their wider role in the current systems of the North Atlantic.

5.6 Summary

The East Greenland Current is the western boundary current of the Irminger Sea, which is one of the key regions where North Atlantic Deep Waters are formed (Lozier et al., 2019). There is observational evidence of symmetric instability being excited in the current when strong northerly winds blow along it (Le Bras et al., 2022). These winds induce an Ekman Transport which acts to steepen isopycnals, making the potential vorticity negative (e.g. Straneo et al., 2002).

Observations show the development of a deep low potential vorticity layer below the convectively mixed layer (Le Bras et al., 2022); however, water mass formation rates are particularly challenging to diagnose from spatially sparse mooring observations. In this chapter we used an ensemble of idealised two-dimensional models of the East Greenland Current to diagnose the changes in the mixed layer depth, changes in the volume of different water mass classes, and the rate of water mass formation within these classes. We forced each ensemble member with temporally Gaussian wind stresses of different durations and peak stresses. The resolution of the models was set to 25 m to ensure the adequate resolution of secondary Kelvin-Helmholtz instabilities which are known to be important in producing irreversible mixing (Griffiths, 2003*b*; Yankovsky and Legg, 2019). A two-dimensional model was employed to keep the computational resources required by the models affordable[4].

In a reference integration, we saw the effect of down front winds on the isopycnal and potential vorticity structure of the current. In the surface 20 m, we saw the formation of a convectively mixed layer with zero stratification. Below this, a low potential vorticity layer formed, which extended much deeper. Due to the high latitude, the stratification in a zero potential vorticity flow is close to zero which

[4]The ensemble required around 60 kCUs to run on the Archer2 HPC facility. A typical annual allocation of resources is around 25 kCUs for individual users.

makes distinguishing between the convectively mixed layer and the zero potential vorticity layer difficult. Due to the dominant effect of symmetric instability on the stratification it may be that existing mixed layer parameterisations of gravitational instability, such as KPP, are sufficient to adequately reproduce the density structure formed by unresolved instabilities and mixing in coarse resolution models (Large et al., 1994). Comparing the results of high-resolution symmetric instability resolving models with coarser models using KPP or symmetric instability specific parameterisations (e.g. Bachman et al. (2017); Yankovsky et al. (2021)) would be a good first step in assessing whether this approach is feasible. One limitation of the symmetric instability specific parameterisations may be that they tend to restratify the mixed layer, whereas here we have found symmetric instability can also have destratifying effects (Bachman et al., 2017).

Across all integrations in the ensemble, we saw how large volume anomalies in the surface water mass classes could be generated by instantaneous water mass formation rates of up to around 1 Sv when integrated along a 100 km long stretch of the current. The wind events causing these large water mass formation rates are, however, highly seasonal and only occur several times a year during winter and spring. When averaged out over a year, these formation rates will be much less substantial. This leads to the question of how significant these water mass formation rates are. We suggest that they may be important in explaining some high-frequency variability in the AMOC during winter and spring times.

Haine and Marshall (1998) demonstrate how symmetric instability can precondition the mixed layer such that it is more susceptible to baroclinic instabilities. As such, we hypothesise that the deepening of the mixed layer by barrier wind events may be important in pre-conditioning it before waters undergo subsequent density transformations resulting from the action of baroclinic instability.

We have seen how under some circumstances the time-integrated wind stress

can act as a good predictor for the water mass formation rates in different density classes, as well as the volume anomalies within these classes. The deepening of the mixed layer generated by symmetric instability was found to scale with the integrated wind stress to the power of 0.54, which is remarkably close to the value of 0.5 theoretically predicted by Taylor and Ferrari (2010). Despite this close agreement, the deepening of the mixed layer deviates from it at when the maximum wind stress of an event is large. The deepening of the mixed layer is found to saturate for large wind stresses and the duration of the wind event then becomes the dominant control — in other words, longer wind events produce a deeper mixed layer for a given integrated wind stress. This result is also reflected in the ensemble volume anomalies and water mass formation rates. A more appropriate predictor than the time-integrated wind stress may be the time-integrated Ekman buoyancy flux (the Ekman buoyancy flux is given by equation 5.4) We have not used this measure here due to the increased computational cost of including the time dependence of the horizontal buoyancy gradient term.

The finding that baroclinic instability plays an important role in generating mixing during down front wind events over currents similar to the East Greenland Current (Spall and Thomas, 2016) remains a real limitation on the conclusions we have just drawn: baroclinic instability cannot be resolved in two-dimensional models, such as those used in this study. Our setup, however, differed from that of Spall and Thomas (2016) as we used time-varying rather than constant winds to force our models. We hypothesise that during (short) wind events, symmetric instability is the predominant driver of mixing and restratification in the surface mixed layer. This leads to the generation of a deep mixed layer in which $\partial_z b$ is near-zero and $\partial_x b$ is large. The pre-conditioning of the mixed layer in this way creates a density structure in which the growth rate of baroclinic instability is greatly enhanced (Eady, 1949; Haine and Marshall, 1998). OSNAP observations coupled with

further idealised modelling efforts would be well suited evaluate the importance of subsequently generated baroclinic instabilities.

Chapter 6

Conclusions

You live and learn. At any rate, you live.

Douglas Adams

This thesis set out to investigate the role of symmetric instability in different western boundary current systems, which act as important pathways for waters participating in the basin-scale AMOC. In particular, we focussed on the North Brazil Current and the Deep Western Boundary Current as they cross the equator, and the East Greenland Current during winter and spring-time barrier wind events.

In chapter 1, we examined the importance of the AMOC and saw how mixing in its many constituent currents is of fundamental importance to its large-scale dynamics. We learnt how symmetric instability can be an efficient way to generate submesoscale motions capable of mixing buoyancy, momentum, potential vorticity and other tracers of interest in currents with potential vorticity opposite in sign to that of the planetary vorticity. We outlined how this mixing may go some way towards solving the "cross-equatorial flow problem". The crux of this problem is that in order for large-scale interhemispheric water exchanges to occur, there must exist a process capable of changing the sign of the potential vorticity of waters crossing the equator (Csanady, 1985; Nof, 1990; Killworth, 1991). The conservation of potential vorticity, however, places limits on the kinds of processes which

may modify potential vorticity and requires the mechanism to move velocity and buoyancy gradients towards dissipative scales (Haynes and McIntyre, 1987). The AMOC's climatic importance is partly derived from its role in facilitating the interhemispheric transport of waters and so solving this problem is of fundamental importance. Away from the equator, we saw how observations of symmetric instability in the East Greenland Current show that the instability is capable of producing significant deepening of the mixed layer there, but that these observations leave questions about the amount of diapycnal mixing the instability can generate unanswered.

This leads us to chapter 2, where we took an in-depth look at symmetric instability and its properties. We explored two different ways of exciting it — by either changing the sign of the planetary vorticity or changing the sign of the potential vorticity of a fluid parcel. The first mechanism for generating symmetric instability is unique to currents which cross the equator. A water parcel stable to symmetric instability in one Hemisphere will not be stable to symmetric instability in the opposing Hemisphere. This instability can be generated outside the surface and bottom boundary layers where potential vorticity forcing occurs, making symmetric instability generated in this way distinct from instability generated by buoyancy or momentum forcing.

We then examined how Ekman buoyancy forcing by down front wind events can generate anomalous potential vorticity and hence symmetric instability (although alternate methods of generating anomalous potential vorticity exist). Geostrophically balanced currents have outcropping isopycnals. When the wind blows along these currents, the surface waters experience Ekman transport perpendicular to the wind, which can act to steepen the isopycnals. If the winds are sufficiently strong this can lead to a change in sign of the potential vorticity. This mechanism has been observed to be at play in the East Greenland Current.

In the following sections we explored where the symmetric instability criterion comes from, examined the orientation of the overturning cells generated by the instability, and looked at gravitational and inertial instabilities as limiting cases of symmetric instability — symmetric instability can be interpreted as inertial instability along isopycnals or gravitational instability along vortex tubes. This led us to an examination of the energetics of the instability, which in turn informed a discussion of the "classical" and "energetic" definitions of symmetric instability. In this thesis, we employed the classical definition of symmetric instability, in which gravitational, inertial and slantwise convective instabilities are different "flavours" of symmetric instability.

These previous results were derived by considering a symmetric Eady type problem, that of a parallel shear flow (Eady, 1949; Ooyama, 1966; Stone, 1966; Hoskins, 1974). We then looked at the axisymmetric problem, which to first order, models the behaviour of symmetric instability in eddies. We saw how rotation modifies the instability criterion, with the cores of anticyclonic eddies being stabilised by the additional centrifugal forces (Buckingham et al., 2021*a*). Having reviewed the established theory of symmetric instability, we broke new ground, applying linear stability analyses to both the North Brazil Current and its rings and the Deep Western Boundary Current as they cross the equator. We used these results to make predictions about the timescales at play and the structures we may see when these currents cross the equator. Although some strong assumptions were made in the application of theory to these real-world currents, the theory's predictions were invaluable in identifying symmetric instability in the more complex numerical models subsequently presented. We see great potential in the use of simple numerical models, like those developed here, in diagnosing symmetric instability in observations and more-realistic General Circulation Model outputs. Using linear theory we were also able to challenge the assumption that the complete Coriolis force

would modify the properties of symmetric instability in flows such as the North Brazil Current as they cross the equator. Building on the work of Zeitlin (2018) we identified a new measure of the influence of the complete Coriolis force on symmetrically unstable flows which takes into account the flow's direction. We also defined a class of forces that leave the structure and growth rates of symmetric instabilities unchanged, leading to a more comprehensive understanding of the kinds of forces that can be neglected when studying symmetric instabilities.

In chapter 3, we examined symmetric instability in the North Brazil Current, investigating the instability's role in ridding the current of anomalous potential vorticity originating in Southern Hemisphere waters and in generating diapycnal mixing. Through the use of high-resolution modelling, we were able to demonstrate the effect of symmetric instability in setting the absolute vorticity of the flow to zero. Most General Circulation Models neutralise the anomalous potential vorticity of Southern Hemisphere Waters as they cross the equator through lateral dissipation provided by an eddy viscosity (Edwards and Pedlosky, 1998*a*). That the effect of the instability is to set the absolute vorticity of the flow to zero suggests that, to first order, such a viscosity may parameterise the process adequately within coarse resolution models.

That said, care should be taken when applying such parameterisation. It is known that upon crossing the equator, the northward propagation of Southern Hemisphere waters is limited by the rate at which their potential vorticity is modified (Killworth, 1991). This means to get the correct interhemispheric mass exchange, the viscous vorticity tendencies must be the same as those resulting from symmetric instability. In a low resolution ocean model with a high eddy viscosity, it is not clear whether there would be an over or under estimation of the interhemispheric mass exchange. The high viscosity would likely lead to a large vorticity tendency whereas the coarse resolution would eliminate the vorticity gradients

on which the viscosity would act. Furthermore, a viscous model would have more sluggish western boundary currents leading to a reduction in cross-equatorial transport. Further research is necessary to determine which of these biases is dominant, as currently most ocean models (knowingly or not) employ a viscous parameterisation of the effects of symmetric instability. Interhemispheric water exchange has a direct effect on the AMOC's strength, interhemispheric heat transport and the position of the Inter Tropical Convergence Zone. These key diagnostics are frequently reported by climate models. Biases in these quantities may modify modelled atmosphere-ocean feedbacks, leading to errors in projections of the climate response to anthropogenic greenhouse gas emissions. A caveat to this is that our model is likely underestimating water mass transformation rates which affect the density structure. This is due to the resolution being too coarse to resolve secondary Kelvin-Helmholtz instabilities which are known to be important in the generation of water mass transformations by symmetric instability (e.g. Griffiths, 2003*b*; Taylor and Ferrari, 2009; Yankovsky and Legg, 2019). Despite this limitation, our models still show symmetric instability can produce a large amount of mixing, with up to 2 Sv worth of transformation between surface and intermediate waters and between 2 Sv and 4 Sv of transformation between intermediate and deep waters. Due to the nature of symmetric instability in cross-equatorial western boundary currents, this transformation is occurring continuously, meaning symmetric instability may be important in transforming surface waters into deep waters in the Tropical Atlantic. The water mass transformation rates, as opposed to the formation rates, will give a more reliable assessment of the importance of symmetric instability in generating mixing, however, these calculations are more computationally expensive to perform. It would also be interesting to investigate these rates in more realistic models of the Tropical Atlantic such as the GIGATL

(Gula et al., 2021) and MITgcm LLC4320 (Forget et al., 2015) models[1].

In chapter 4 we examined the excitement of symmetric instability in the Deep Western Boundary Current as it crossed the equator. We showed that despite the growth rate of symmetric instability in the current being very small (due to the smallness of both the planetary vorticity and the relative vorticity of the current) symmetric instability is still excited and sets the potential vorticity of the flow to zero. If this prediction of the presence of symmetric instability in the Deep Western Boundary Current is borne out by observations, it will be one of the first examples of symmetric instability occurring away from either the surface or bottom boundary layers of the ocean. This work also predicted the latitudes at which we expect the instability to be most active, which may aid in searching for observational evidence of its excitement. We also demonstrated that symmetric instability (or any other overturning instability in a stratified flow) can lead to the generation of density staircases. A clear next step in searching for observational evidence of symmetric instability in the Deep Western Boundary Current would be to analyse existing CTD casts in the region which may show step-like features with a length scale of between approximately 10 m to 250 m. Seismic imaging may also be able to detect these staircases over larger geographic regions (e.g. Fer et al., 2010).

The linear theory of chapter 2 demonstrated the link between the vertical step height of the staircase (set by the height of the overturning cells) and the rate at which secondary instabilities dissipate momentum — as parameterised by a vertical viscosity. Applying the linear theory to observed currents as an inverse-type model would enable an estimation of the viscosity which is best used for parameterising the secondary shear instabilities which equilibrate unstable flows. Such a viscosity may serve as a crude first-order parameterisation of Kelvin-Helmholtz in-

[1] We did attempt to do this in 2020, however, were beset by problems accessing a small subset of the large quantities of data these models produce. Significant progress has been made since then though — see for example the Poseidon project (Haine et al., 2021) and proposals from the Pangeo project (Uchida et al., 2022) which aim to address these issues.

stability in general circulation models of sufficient resolution to permit symmetric instability. The finding in chapter 4 that symmetric instability is occurring much closer to the equator (around 25 km away) in the Deep Western Boundary Current than in the North Brazil Current (around 400 km away) is a great vindication of the power of linear theory. Simple scaling arguments were able to predict these numbers before any modelling had taken place.

Finally, in chapter 5 we investigated the role of Ekman driven symmetric instability in the East Greenland Current. We showed that strong down front wind events have a significant impact on the depth of the upper convectively mixed layer and the deeper low potential vorticity layer through the excitement of symmetric instability, and the subsequent diapycnal mixing it generates. The deepening of the mixed layer was found to scale with the integrated wind stress to the power of 0.54, which is in close agreement with theoretical predictions, which suggest it should scale with the square root of the integrated wind stress (Taylor and Ferrari, 2010). There were however signs that this relationship begins to break down for wind events with a high maximum wind stress, at which point the duration of the wind event becomes a more powerful control on the mixed layer deepening. Furthermore, the mixed layer deepening contrasts with many other studies of symmetric instability during down front wind events, which typically are thought to restratify the mixed layer. We hypothesise the mixed layer deepening is a result of the large planetary component of vorticity at high latitudes meaning the zero potential vorticity state must also correspond to a low stratification state.

That down front winds can generate up to 2 Sv of mixing (when integrated over the length of the East Greenland Current) suggests that symmetric instability may explain some short timescale overturning variability seen in AMOC observations at the OSNAP East array. Despite the significant amounts of instantaneous diapycnal mixing generated by down front wind events in our model, it is clear that the

wind events themselves are not frequent enough for the amount of diapycnal mixing generated to account for more than a few tenths of a Sverdrup of deep water formation when integrated over the length of the current and a 12-month period. However, this is not to say that the process is insignificant. The deepening of the mixed layer during these wind events may be important in pre-conditioning surface waters, ready for other processes to transform them into North Atlantic Deep Waters — this should be investigated further. In particular, the role of baroclinic instability in producing further mixing should be looked into, with Gelderloos et al. (2011) finding that eddies play an important role in restratifying the mixed layer in the Labrador Sea following deep convection. Baroclinic instability was not present in the idealised models presented here.

Significantly, chapter 5 suggests that a simple mixed layer parameterisation of gravitational instability, such as KPP, may adequately represent the mixing produced by Ekman induced symmetric instability in the East Greenland Current. This is due to the high latitude meaning the zero potential vorticity state is very close to a zero stratification state. The effectiveness of such a parameterisation should be evaluated and compared to the results we present here, as should the effectiveness of parametrisations specifically targeted at representing the effects of symmetric instability. The KPP parameterisation is already implemented in many climate and general circulation models, meaning minimal work would be required to ensure we are adequately representing the mixing induced by down front wind events.

This thesis has examined the role of symmetric instability in three very different currents — the surface intensified North Brazil Current, the much slower Deep Western Boundary Current as it crosses the equator, and the highly baroclinic East Greenland Current. Symmetric instabilities are often seen as sitting on a spectrum, with gravitational instability at one end and inertial instability at the other. We have explored both extremes of the spectrum in this work and, I

hope, demonstrated how a classical definition of symmetric instability aids in understanding this class of overturning instabilities. We have seen how symmetric instability plays a role in the mixing of buoyancy, momentum and potential vorticity in each of these currents. These three currents, however, are only a small subset of those which combine to form the AMOC. The role of submesoscale instability in many other currents which contribute to this global scale circulation is yet to be examined. Our understanding of the interior cross-equatorial pathways in the Tropical Atlantic remains incomplete — in part due to the difficulty in making observations resulting from the breakdown of geostrophy (e.g. Vianna and de Menezes, 2003). Our understanding of deep water formation sites and processes in the Sub-polar North Atlantic is increasing year-on-year, with unprecedented observations from the ONSAP array revealing the complexity of the circulations in the Sub-polar North Atlantic. In short, theory and models still have a way to go to provide a complete description of the AMOC. It is only by utilising observations when developing theory (as in chapter 5) or by utilising theory to inform observations (as we hope to with the staircases seen in chapter 4) that we will be able to answer the most pressing questions in the field of AMOC science.

It is imperative that we both understand, and are able to adequately model the ocean's response to anthropogenic climate change. Small-scale processes are key to determining the amount of heat and carbon the ocean will take up (de Lavergne et al., 2022), while the large-scale circulation will determine how these tracers are redistributed across the globe (Buckley and Marshall, 2016). Parameters in climate models are often tuned to reproduce globally integrated metrics (for example diapycnal mixing rates), however, this often results in climate models producing the "right answer for the wrong reasons" — a classic example of this is the AMOC's overturning stream function which can be reliably reproduced despite the fact that deep water formation occurs, predominantly, in the wrong sea (Lozier et al., 2019;

Hirschi et al., 2020). Correcting such spatial biases is imperative to ensuring climate models are able to make reliable predictions about future climate. This requires a three-pronged approach — observations are needed to discover where these biases occur, theory and idealised modelling are required to explain observations, and finally parameterisations are required to correct the biases.

Software & data

This work was made possible by several open-source pieces of software. These include cartopy (Elson et al., 2022), dask (Dask Development Team, 2016; Matthew Rocklin, 2015), matplotlib (Hunter, 2007), MITgcm (Campin et al., 2022), numpy (Harris et al., 2020), scipy (Virtanen et al., 2020), xarray (Hoyer and Hamman, 2017), xmitgcm (Abernathey et al., 2021) and zarr (Miles et al., 2022).

The codes used to produce all figures and run all model integrations are available in Goldsworth (2022*a*,*b*,*c*,*d*). Selected model outputs are archived in Goldsworth (2022*e*).

List of symbols

Greek letters

α_T	Thermal expansion coefficient
β	Meridional gradient of planetary vorticity
Γ	The non-traditionality parameter
γ^n	Neutral density
δ_b	Bickley jet width
$\Delta\psi$	Net volume flux out of a region
ζ	Absolute vorticity
θ	Latitude
κ	Buoyancy diffusion coefficient
λ	Vertical wavelength
λ^*	Vertical wavelength which maximises σ for a given A_r
ξ	Relative vorticity, $\boldsymbol{\nabla} \times \mathbf{u}$
ξ, ξ_y	Vertical and meridional components of relative vorticity
Π	Geopotential pressure
ρ, ρ_0	Density and reference density
σ	A growth rate
τ	$\tan\Phi$

τ_e	e-folding timescale
τ_y	Meridional wind stress
Φ	Angle of disturbance to the horizontal
Φ_{iso}	Isopycnal slope
χ	Angle of coastline to a meridian
ψ	An overturning stream function
$\hat{\psi}$	The horizontal component of a separable overturning stream function
ω	An oscillatory frequency, or growth rate if imaginary

Latin letters

A_r	Vertical viscosity
b	Buoyancy
d	An advective length scale
D_t	Material (advective) derivative
$\partial_{t'}$	$\partial_t - A_r \partial_{zz}^2$
E_k	Kinetic energy
$\mathbf{f}$	Planetary vorticity vector
f	Coriolis parameter, the vertical component of planetary vorticity
f_0	Planetary vorticity on an f-plane
f'	Modified Coriolis parameter, $f + 2\,V_\phi / r$
F_{NT}	The meridional or non-traditional component of planetary vorticity.
$\mathcal{F}_x, \mathcal{F}_z$	Zonal and meridional components of a force
$\mathcal{F}$	Water mass formation rate
g	Gravitational acceleration
G	Diapycnal volume flux
H	A vertical length scale

k	A horizontal wavenumber or wavenumber magnitude
L	A horizontal length scale
m	A vertical wavenumber
N^2, M^2	Vertical and horizontal derivatives of buoyancy
P	Geopotential pressure
Q	Ertel potential vorticity
r	Pearson correlation coefficient
r, ϕ, z	Cylindrical polar coordinates
Sv	Sverdrup — unit of 1×10^6 m^3 s^{-1}
t	time
T, T_0	Temperature, reference temperature
u, v, w	Cartesian components of velocity
v_r, v_ϕ, w	Cylindrical polar components of velocity
$\mathcal{V}$	Volume enclosed by two isopycnals
x, y, z	Cartesian coordinates

References

Abernathey, R., Dussin, R., Smith, T., Fenty, I., Bourgault, P., Jones, S., Bot, S., Doddridge, E., Goldsworth, F., Losch, M., Almansi, M., Uchida, T., Cimatoribus, A., Schneider, A. D., Leskis, A., Quintana, A., Ponte, A., Rose, B., Balwada, D., Sérazin, G. and Brannigan, L. (2021), "MITgcm/xmitgcm: V0.5.2". Software, published on *zenodo*.
doi: *10.5281/zenodo.5139886*

Abernathey, R., Gnanadesikan, A., Pradal, M.-A. and Sundermeyer, M. A. (2022), *Chapter 9 - Isopycnal mixing*, Elsevier, pp. 215–256.
doi: *10.1016/B978-0-12-821512-8.00016-5*

Aguedjou, H. M., Dadou, I., Chaigneau, A., Morel, Y. and Alory, G. (2019), "Eddies in the Tropical Atlantic Ocean and Their Seasonal Variability", *Geophysical Research Letters* **46**(21), 12156–12164.
doi: *10.1029/2019GL083925*

Akuetevi, C. and Wirth, A. (2015), "Dynamics of turbulent western-boundary currents at low latitude in a shallow-water model", *Ocean Science* **11**(3), 471–481.
doi: *10.5194/os-11-471-2015*

Allen, J. S. and Newberger, P. A. (1996), "Downwelling Circulation on the Oregon Continental Shelf. Part I: Response to Idealized Forcing", *Journal of Physical Oceanography* **26**(10), 2011–2035.
doi: *10.1175/1520-0485(1996)026<2011:DCOTOC>2.0.CO;2*

AMS (2022), "Ozmidov scale", *AMS glossary of meteorology*
url: *https://glossary.ametsoc.org/wiki/Ozmidov_scale*

Argo (2022), "Argo float data and metadata from global data assembly centre (argo GDAC)". Dataset.
doi: *10.17882/42182*

Arhan, M., Mercier, H., Bourlès, B. and Gouriou, Y. (1998), "Hydrographic sections across the Atlantic at 7°30N and 4°30S", *Deep Sea Research Part I: Oceanographic Research Papers* **45**(6), 829–872.
doi: *10.1016/S0967-0637(98)00001-6*

Bachman, S. D., Fox-Kemper, B., Taylor, J. R. and Thomas, L. N. (2017), "Parameterization of Frontal Symmetric Instabilities. I: Theory for Resolved Fronts", *Ocean Modelling* **109**, 72–95.
doi: *10.1016/j.ocemod.2016.12.003*

Bachman, S. D. and Taylor, J. R. (2014), "Modelling of partially-resolved oceanic symmetric instability", *Ocean Modelling* **82**, 15–27.
doi: *10.1016/j.ocemod.2014.07.006*

Balmforth, N. J., Llewellyn Smith, S. G. and Young, W. R. (1998), "Dynamics of interfaces and layers in a stratified turbulent fluid", *Journal of Fluid Mechanics* **355**, 329–358.
doi: *10.1017/S0022112097007970*

Barnier, B., Reynaud, T., Beckmann, A., Böning, C., Molines, J.-M., Barnard, S. and Jia, Y. (2001), "On the seasonal variability and eddies in the North Brazil Current: Insights from model intercomparison experiments", *Progress in Oceanography* **48**(2-3), 195–230.
doi: *10.1016/S0079-6611(01)00005-2*

Boccaletti, G., Ferrari, R. and Fox-Kemper, B. (2007), "Mixed layer instabilities and restratification", *Journal of Physical Oceanography* **37**(9), 2228–2250.
doi: *10.1175/JPO3101.1*

Bosse, A., Testor, P., Damien, P., Estournel, C., Marsaleix, P., Mortier, L., Prieur, L. and Taillandier, V. (2021), "Wind-Forced Submesoscale Symmetric Instability around Deep Convection in the Northwestern Mediterranean Sea", *Fluids* **6**(3), 123.
doi: *10.3390/fluids6030123*

Bourlès, B., Gouriou, Y. and Chuchla, R. (1999), "On the circulation in the upper layer of the western equatorial Atlantic", *Journal of Geophysical Research: Oceans* **104**(C9), 21151–21170.
doi: *10.1029/1999jc900058*

Bower, A., Lozier, S., Biastoch, A., Drouin, K., Foukal, N., Furey, H., Lankhorst, M., Rühs, S. and Zou, S. (2019), "Lagrangian Views of the Pathways of the Atlantic Meridional Overturning Circulation", *Journal of Geophysical Research: Oceans* **124**(8), 5313–5335.
doi: *10.1029/2019JC015014*

Boyer, T. P., Garcia, H. E., Locarnini, R. A., Zweng, M. M., Mishonov, A. V., Reagan, J. R., Weathers, K. A., Baranova, O. K., Seidov, D. and Smolyar, I. V. (2018), "World ocean atlas 2018. Temperature and salinity". Dataset
url: *https://www.ncei.noaa.gov/archive/accession/NCEI-WOA18*

Brannigan, L. (2016), "Intense submesoscale upwelling in anticyclonic eddies", *Geophysical Research Letters* **43**(7), 3360–3369.
doi: *10.1002/2016GL067926*

Brannigan, L., Marshall, D. P., Naveira-Garabato, A. C., George Nurser, A. and Kaiser, J. (2017), "Submesoscale instabilities in mesoscale eddies", *Journal of Physical Oceanography* pp. JPO–D–16–0178.1.
doi: *10.1175/JPO-D-16-0178.1*

Brannigan, L., Marshall, D. P., Naveira-Garabato, A. and George Nurser, A. J. (2015), "The seasonal cycle of submesoscale flows", *Ocean Modelling* **92**, 69–84.
doi: *10.1016/j.ocemod.2015.05.002*

Bryden, H. L., Johns, W. E., King, B. A., McCarthy, G., McDonagh, E. L., Moat, B. I. and Smeed, D. A. (2020), "Reduction in ocean heat transport at 26°N since 2008 cools the eastern subpolar gyre of the North Atlantic Ocean", *Journal of Climate* **33**(5), 1677–1689.
doi: *10.1175/JCLI-D-19-0323.1*

Buckingham, C. E., Gula, J. and Carton, X. (2021*a*), "The Role of Curvature in Modifying Frontal Instabilities. Part I: Review of Theory and Presentation of a Nondimensional Instability Criterion", *Journal of Physical Oceanography* **51**(2), 299–315.
doi: *10.1175/JPO-D-19-0265.1*

Buckingham, C. E., Gula, J. and Carton, X. (2021*b*), "The role of curvature in modifying frontal instabilities. part ii: Application of the criterion to curved density fronts at low richardson numbers", *Journal of Physical Oceanography* **51**(2), 317–341.
doi: *10.1175/JPO-D-20-0258.1*

Buckley, M. W. and Marshall, J. (2016), "Observations, inferences, and mechanisms of the Atlantic Meridional Overturning Circulation: A review", *Reviews of Geophysics* **54**, 5–63.
doi: *10.1002/2015RG000493*

Callies, J. and Ferrari, R. (2013), "Interpreting Energy and Tracer Spectra of Upper-Ocean Turbulence in the Submesoscale Range (1–200 km)", *Journal of Physical Oceanography* **43**(11), 2456–2474.
doi: *10.1175/JPO-D-13-063.1*

Callies, J. and Ferrari, R. (2018), "Dynamics of an Abyssal Circulation Driven by Bottom-Intensified Mixing on Slopes", *Journal of Physical Oceanography* **48**(6), JPO–D–17–0125.1.
doi: *10.1175/JPO-D-17-0125.1*

Campin, J.-M., Heimbach, P., Losch, M., Forget, G., edhill3, Adcroft, A., amolod, Menemenlis, D., dfer22, Hill, C., Jahn, O., Scott, J., stephdut, Mazloff, M., Fox-Kemper, B., Doddridge, E., antnguyen13, Fenty, I., Bates, M., Eichmann, A., Smith, T., mitllheisey, Martin, T., Lauderdale, J., Abernathey, R., Khatiwala, S., Wang, O., dngoldberg, hongandyan and Deremble, B. (2022), "MITgcm/MITgcm: Checkpoint68i". Software, published on *zenodo*.
doi: *10.5281/zenodo.6498956*

Castelão, G. P. and Johns, W. E. (2011), “Sea surface structure of North Brazil Current rings derived from shipboard and moored acoustic Doppler current profiler observations”, *Journal of Geophysical Research: Oceans* **116**(1).
doi: *10.1029/2010JC006575*

Chang, P., Zhang, S., Danabasoglu, G., Yeager, S. G., Fu, H., Wang, H., Castruccio, F. S., Chen, Y., Edwards, J., Fu, D., Jia, Y., Laurindo, L. C., Liu, X., Rosenbloom, N., Small, R. J., Xu, G., Zeng, Y., Zhang, Q., Bacmeister, J., Bailey, D. A., Duan, X., DuVivier, A. K., Li, D., Li, Y., Neale, R., Stössel, A., Wang, L., Zhuang, Y., Baker, A., Bates, S., Dennis, J., Diao, X., Gan, B., Gopal, A., Jia, D., Jing, Z., Ma, X., Saravanan, R., Strand, W. G., Tao, J., Yang, H., Wang, X., Wei, Z. and Wu, L. (2020), “An Unprecedented Set of High-Resolution Earth System Simulations for Understanding Multiscale Interactions in Climate Variability and Change”, *Journal of Advances in Modeling Earth Systems* **12**(12), e2020MS002298.
doi: *10.1029/2020MS002298*

Chelton, D. B., Deszoeke, R. A., Schlax, M. G., El Naggar, K. and Siwertz, N. (1998), “Geographical variability of the first baroclinic Rossby radius of deformation”, *Journal of Physical Oceanography* **28**(3), 433–460.
doi: *10.1175/1520-0485(1998)028<0433:GVOTFB>2.0.CO;2*

Cimoli, L., Mashayek, A., Johnson, H. L., Marshall, D. P., Naveira Garabato, A. C., Whalen, C., Vic, C., de Lavergne, C., Alford, M. H., MacKinnon, J. A. and Talley, L. D. (2022), “Significance of diapycnal mixing within the Atlantic Meridional Overturning Circulation”. Preprint.
doi: *10.1002/essoar.10512257.1*

Cruz-Gómez, R. and Salcedo-Castro, J. (2013), “Analysis of horizontal and vertical ring structure based on analytical model and satellite data: Application to the North Brazil Current Rings”, *Ocean Science Journal* **48**(2), 161–172.
doi: *10.1007/s12601-013-0013-2*

Csanady, G. T. (1985), “Zero potential vorticity model of the North Brazilian coastal current.”, *Journal of Marine Research* **43**(3), 553–579.
doi: *10.1357/002224085788440321*

D’Asaro, E., Lee, C., Rainville, L., Harcourt, R. and Thomas, L. N. (2011), “Enhanced turbulence and energy dissipation at ocean fronts”, *Science* **332**(6027), 318–322.
doi: *10.1126/science.1201515*

Dask Development Team (2016), “Dask: Library for dynamic task scheduling”. Software
url: *https:// dask.org*

de Jong, M. F. and de Steur, L. (2016), “Strong winter cooling over the Irminger Sea in winter 2014–2015, exceptional deep convection, and the emergence of anomalously low SST”, *Geophysical Research Letters* **43**(13), 7106–7113.
doi: *10.1002/2016GL069596*

de Lavergne, C., Groeskamp, S., Zika, J. and Johnson, H. L. (2022), Chapter 3 — The role of mixing in the large-scale ocean circulation, *in* M. Meredith and A. Naveira Garabato, eds, “Ocean Mixing”, Elsevier, pp. 35–63.
doi: *10.1016/B978-0-12-821512-8.00010-4*

Dengler, M., Schott, F. A., Eden, C., Brandt, P., Fischer, J. and Zantopp, R. J. (2004), “Break-up of the Atlantic deep western boundary current into eddies at 8° S”, *Nature* **432**(7020), 1018–1020.
doi: *10.1038/nature03134*

Deremble, B., Dewar, W. K. and Chassignet, E. P. (2017), "Vorticity dynamics near sharp topographic features", *Journal of Marine Research* **74**(6), 249–276.
doi: *10.1357/002224016821744142*

D'Orgeville, M., Hua, B. L., Schopp, R. and Bunge, L. (2004), "Extended deep equatorial layering as a possible imprint of inertial instability", *Geophysical Research Letters* **31**(22), 1–5.
doi: *10.1029/2004GL020845*

Eady, E. T. (1949), "Long Waves and Cyclone Waves", *Tellus* **1**(3), 33–52.
doi: *10.1111/j.2153-3490.1949.tb01265.x*

Eden, C. and Willebrand, J. (1999), "Neutral density revisited", *Deep Sea Research Part II: Topical Studies in Oceanography* **46**(1-2), 33–54.
doi: *10.1016/S0967-0645(98)00113-1*

Edwards, C. A. and Pedlosky, J. (1998*a*), "Dynamics of nonlinear cross-equatorial flow. Part I: Potential vorticity transformation", *Journal of Physical Oceanography* **28**(12), 2382–2406.
doi: *10.1175/1520-0485(1998)028<2382:DONCEF>2.0.CO;2*

Edwards, C. A. and Pedlosky, J. (1998*b*), "Dynamics of Nonlinear Cross-Equatorial Flow. Part II: The Tropically Enhanced Instability of the Western Boundary Current", *Journal of Physical Oceanography* **28**(12), 2407–2417.
doi: *10.1175/1520-0485(1998)028<2407:DONCEF>2.0.CO;2*

Elson, P., de Andrade, E. S., Lucas, G., May, R., Hattersley, R., Campbell, E., Dawson, A., Raynaud, S., scmc72, Little, B., Snow, A. D., Donkers, K., Blay, B., Killick, P., Wilson, N., Peglar, P., lbdreyer, Andrew, Szymaniak, J., Berchet, A., Bosley, C., Davis, L., Filipe, Krasting, J., Bradbury, M., Kirkham, D., stephenworsley, Clément, Caria, G. and Hedley, M. (2022), "SciTools/cartopy: V0.21.0". Software, published on *zenodo*.
doi: *10.5281/zenodo.7065949*

Emanuel, K. A. (1994), Slantwise convection, *in* "Atmospheric Convection", Oxford University Press, Oxford, pp. 392–417

Ertel, H. (1942), "Ein neuer hydrodynamischer Erhaltungssatz", *Naturwissenschaften* **30**(36), 543–544.
doi: *10.1007/BF01475602*

Evans, D. G., Frajka-Williams, E. E., Naveira Garabato, A. C., Polzin, K. L. and Forryan, A. (2020), "Mesoscale eddy dissipation by a 'zoo' of submesoscale processes at a western boundary", *Journal of Geophysical Research: Oceans* pp. 1–25.
doi: *10.1029/2020jc016246*

Evans, D. G., Holliday, N. P., Bacon, S. and Le Bras, I. (2022), "Mixing and air-sea buoyancy fluxes set the time-mean overturning circulation in the subpolar north atlantic", *EGUsphere* **2022**, 1–36.
doi: *10.5194/egusphere-2022-1059*

Fer, I., Nandi, P., Holbrook, W. S., Schmitt, R. W. and Páramo, P. (2010), "Seismic imaging of a thermohaline staircase in the western tropical North Atlantic", *Ocean Science* **6**(3), 621–631.
doi: *10.5194/os-6-621-2010*

Ferrari, R., Mashayek, A., McDougall, T. J., Nikurashin, M. and Campin, J. M. (2016), "Turning Ocean Mixing Upside Down", *Journal of Physical Oceanography* **46**(7), 2239–2261.
doi: *10.1175/JPO-D-15-0244.1*

Foldvik, A., Aagaard, K. and Tørresen, T. (1988), "On the velocity field of the East Greenland Current", *Deep Sea Research Part A. Oceanographic Research Papers* **35**(8), 1335–1354.
doi: *10.1016/0198-0149(88)90086-6*

Fonseca, C. A., Goni, G. J., Johns, W. E. and Campos, E. J. (2004), "Investigation of the North Brazil Current retroflection and North Equatorial Countercurrent variability", *Geophysical Research Letters* **31**(21).
doi: *10.1029/2004GL020054*

Forget, G., Campin, J. M., Heimbach, P., Hill, C. N., Ponte, R. M. and Wunsch, C. (2015), "ECCO version 4: An integrated framework for non-linear inverse modeling and global ocean state estimation", *Geoscientific Model Development* **8**(10), 3071–3104.
doi: *10.5194/gmd-8-3071-2015*

Forryan, A., Naveira Garabato, A. C., Vic, C., Nurser, A. J. and Hearn, A. R. (2021), "Galápagos upwelling driven by localized wind–front interactions", *Scientific Reports* **11**(1), 1–12.
doi: *10.1038/s41598-020-80609-2*

Fox-Kemper, B. and Ferrari, R. (2008), "Parameterization of Mixed Layer Eddies. Part II: Prognosis and Impact", *Journal of Physical Oceanography* **38**(6), 1166–1179. Publisher: American Meteorological Society Section: Journal of Physical Oceanography,
doi: *10.1175/2007JPO3788.1*

Fox-Kemper, B., Ferrari, R. and Hallberg, R. (2008), "Parameterization of Mixed Layer Eddies. Part I: Theory and Diagnosis", *Journal of Physical Oceanography* **38**(6), 1145–1165. Publisher: American Meteorological Society Section: Journal of Physical Oceanography,
doi: *10.1175/2007JPO3792.1*

Fratantoni, D. M., Johns, W. E., Townsend, T. L. and Hurlburt, H. E. (2000), "Low-Latitude Circulation and Mass Transport Pathways in a Model of the Tropical Atlantic Ocean", *Journal of Physical Oceanography* **30**(8), 1944–1966.
doi: *10.1175/1520-0485(2000)030<1944:LLCAMT>2.0.CO;2*

Fratantoni, D. M. and Richardson, P. L. (2006), "The evolution and demise of North Brazil Current rings", *Journal of Physical Oceanography* **36**(7), 1241–1264.
doi: *10.1175/JPO2907.1*

Fučkar, N. S., Xie, S. P., Farneti, R., Maroon, E. A. and Frierson, D. M. (2013), "Influence of the extratropical ocean circulation on the intertropical convergence zone in an idealized coupled general circulation model", *Journal of Climate* **26**(13), 4612–4629.
doi: *10.1175/JCLI-D-12-00294.1*

Garzoli, S. L., Ffield, A. and Yao, Q. (2003), North Brazil Current rings and the variability in the latitude of retroflection, *in* G. J. Goni and P. Malanotte-Rizzoli, eds, "Interhemispheric Water Exchange in the Atlantic Ocean", Elsevier, Amste, pp. 357–373.
doi: *10.1016/S0422-9894(03)80154-X*

GEBCO Compilation Group (2020), "GEBCO 2020 grid". Dataset.
doi: *10.5285/a29c5465-b138-234d-e053-6c86abc040b9*

Gelderloos, R., Katsman, C. A. and Drijfhout, S. S. (2011), "Assessing the roles of three eddy types in restratifying the Labrador Sea after deep convection", *Journal of Physical Oceanography* **41**(11), 2102–2119.
doi: *10.1175/JPO-D-11-054.1*

Gnanadesikan, A. (1999), "A Simple Predictive Model for the Structure of the Oceanic Pycnocline", *Science* **283**(5410), 2077–2079.
doi: *10.1126/science.283.5410.2077*

Goes, M. P., Marshall, D. P. and Wainer, I. (2009), "Eddy Formation in the Tropical Atlantic Induced by Abrupt Changes in the Meridional Overturning Circulation", *Journal of Physical Oceanography* **39**(11), 3021–3031.
doi: *10.1175/2009JPO4004.1*

Goldsworth, F. (2022*a*), "Fraserwg/dwbc-proj: V1.1". Software, published on *zenodo*.
doi: *10.5281/zenodo.7145228*

Goldsworth, F. (2022*b*), "Fraserwg/irminger-proj: V1.0". Software, published on *zenodo*.
doi: *10.5281/zenodo.7145225*

Goldsworth, F. (2022*c*), "Fraserwg/nbc-proj: V1.0". Software, published on *zenodo*.
doi: *10.5281/zenodo.7145227*

Goldsworth, F. (2022*d*), "Fraserwg/symmetric-instability-proj: V1.0". Software, published on *zenodo*.
doi: *10.5281/zenodo.7145223*

Goldsworth, F. W. (2022*e*), "Data for 'Symmetric instability in the Atlantic Meridional Overturning Circulation"'. Dataset, published on *zenodo*.
doi: *10.5281/zenodo.7148573*

Goldsworth, F. W., Johnson, H. L. and Marshall, D. P. (2022), "Density staircases generated by symmetric instability in a cross-equatorial deep western boundary current", *Geophysical Research Letters* **49**(22), e2022GL100961.
doi: *10.1029/2022GL100961*

Goldsworth, F. W., Marshall, D. P. and Johnson, H. L. (2021), "Symmetric instability in cross-equatorial western boundary currents", *Journal of Physical Oceanography* **51**(6), 2049–2067.
doi: *10.1175/JPO-D-20-0273.1*

Griffies, S. M. and Hallberg, R. W. (2000), "Biharmonic friction with a Smagorinsky-like viscosity for use in large-scale eddy-permitting ocean models", *Monthly Weather Review* **128**(8), 2935–2946.
doi: *10.1175/1520-0493(2000)128<2935:bfwasl>2.0.co;2*

Griffiths, S. D. (2003*a*), "The nonlinear evolution of zonally symmetric equatorial inertial instability", *Journal of Fluid Mechanics* **474**, 245–273.
doi: *10.1017/S0022112002002586*

Griffiths, S. D. (2003*b*), "Nonlinear vertical scale selection in equatorial inertial instability", *Journal of the Atmospheric Sciences* **60**(7), 977–990.
doi: *10.1175/1520-0469(2003)060<0977:NVSSIE>2.0.CO;2*

Grisouard, N. (2018), "Extraction of potential energy from geostrophic fronts by inertial-symmetric instabilities", *Journal of Physical Oceanography* **48**(5), 1033–1051.
doi: *10.1175/JPO-D-17-0160.1*

Groeskamp, S., Abernathey, R. P. and Klocker, A. (2016), "Water mass transformation by cabbeling and thermobaricity", *Geophysical Research Letters* **43**(20).
doi: *10.1002/2016GL070860*

Groeskamp, S., Griffies, S. M., Iudicone, D., Marsh, R., Nurser, A. J. and Zika, J. D. (2019), "The water mass transformation framework for ocean physics and biogeochemistry", *Annual Review of Marine Science* **11**, 271–305.
doi: *10.1146/annurev-marine-010318-095421*

Gula, J., Taylor, J., Shcherbina, A. and Mahadevan, A. (2022), Submesoscale processes and mixing, *in* "Ocean Mixing", Elsevier, pp. 181–214.
doi: *10.1016/B978-0-12-821512-8.00015-3*

Gula, J., Theetten, S., Cambon, G. and Roullet, G. (2021), "Description of the GIGATL simulations". Software, published on *zenodo*.
doi: *10.5281/zenodo.4948523*

Haine, T. W., Gelderloos, R., Jimenez-Urias, M. A., Siddiqui, A. H., Lemson, G., Medvedev, D., Szalay, A., Abernathey, R. P., Almansi, M., Hill, C. N. and Haine, T. W. (2021), "Is computational oceanography coming of age?", *Bulletin of the American Meteorological Society* **102**(8), E1481–E1493.
doi: *10.1175/BAMS-D-20-0258.1*

Haine, T. W. N. and Marshall, J. (1998), “Gravitational, Symmetric, and Baroclinic Instability of the Ocean Mixed Layer”, *Journal of Physical Oceanography* **28**(4), 634–658.
doi: *10.1175/1520-0485(1998)028<0634:gsabio>2.0.co;2*

Harden, B. E. and Renfrew, I. A. (2012), “On the spatial distribution of high winds off southeast Greenland”, *Geophysical Research Letters* **39**(14).
doi: *10.1029/2012GL052245*

Harris, C. R., Millman, K. J., van der Walt, S. J., Gommers, R., Virtanen, P., Cournapeau, D., Wieser, E., Taylor, J., Berg, S., Smith, N. J., Kern, R., Picus, M., Hoyer, S., van Kerkwijk, M. H., Brett, M., Haldane, A., del Río, J. F., Wiebe, M., Peterson, P., Gérard-Marchant, P., Sheppard, K., Reddy, T., Weckesser, W., Abbasi, H., Gohlke, C. and Oliphant, T. E. (2020), “Array programming with NumPy”, *Nature* **585**(7825), 357–362.
doi: *10.1038/s41586-020-2649-2*

Haynes, P. H. and McIntyre, M. E. (1987), “On the Evolution of Vorticity and Potential Vorticity in the Presence of Diabatic Heating and Frictional or Other Forces”, *Journal of the Atmospheric Sciences* **44**(5), 828–841.
doi: *10.1175/1520-0469(1987)044<0828:OTEOVA>2.0.CO;2*

Hirschi, J., Baehr, J., Marotzke, J., Stark, J., Cunningham, S. and Beismann, J.-O. (2003), “A monitoring design for the Atlantic meridional overturning circulation”, *Geophysical Research Letters* **30**(7).
doi: *10.1029/2002GL016776*

Hirschi, J. J., Barnier, B., Böning, C., Biastoch, A., Blaker, A. T., Coward, A., Danilov, S., Drijfhout, S., Getzlaff, K., Griffies, S. M., Hasumi, H., Hewitt, H., Iovino, D., Kawasaki, T., Kiss, A. E., Koldunov, N., Marzocchi, A., Mecking, J. V., Moat, B., Molines, J. M., Myers, P. G., Penduff, T., Roberts, M., Treguier, A. M., Sein, D. V., Sidorenko, D., Small, J., Spence, P., Thompson, L. A., Weijer, W. and Xu, X. (2020), "The Atlantic Meridional Overturning Circulation in High-Resolution Models", *Journal of Geophysical Research: Oceans* **125**(4), 1–35.
doi: *10.1029/2019JC015522*

Hoskins, B. J. (1974), "The role of potential vorticity in symmetric stability and instability", *Quarterly Journal of the Royal Meteorological Society* **100**(425), 480–482.
doi: *10.1002/qj.49710042520*

Hoyer, S. and Hamman, J. J. (2017), "Xarray: N-D labeled Arrays and Datasets in Python", *Journal of Open Research Software* **5**, 1–6.
doi: *10.5334/jors.148*

Hua, B. L., Moore, D. W. and Le Gentil, S. (1997), "Inertial nonlinear equilibration of equatorial flows", *Journal of Fluid Mechanics* **331**, 345–371.
doi: *10.1017/S0022112096004016*

Hunter, J. D. (2007), "Matplotlib: A 2D graphics environment", *Computing in Science & Engineering* **9**(3), 90–95.
doi: *10.1109/MCSE.2007.55*

Jackson, L. C., Kahana, R., Graham, T., Ringer, M. A., Woollings, T., Mecking, J. V. and Wood, R. A. (2015), "Global and European climate impacts of a slowdown of the AMOC in a high resolution GCM", *Climate Dynamics* **45**(11-12), 3299–3316.
doi: *10.1007/s00382-015-2540-2*

Jakoboski, J., Todd, R. E., Owens, W. B., Karnauskas, K. B. and Rudnick, D. L. (2022), "Potential Vorticity and Instability in the Pacific Equatorial Undercurrent West of the Galápagos Archipelago", *Journal of Physical Oceanography* .
doi: *10.1175/JPO-D-21-0124.1*

Jochum, M. and Malanotte-Rizzoli, P. (2003), "On the generation of North Brazil Current rings", *Journal of Marine Research* **61**(2), 147–173.
doi: *10.1357/002224003322005050*

Johannessen, O. M. and Lee, O. S. (1974), "A deep stepped thermo-haline structure in the Mediterranean", *Deep Sea Research and Oceanographic Abstracts* **21**(8), 629–639.
doi: *10.1016/0011-7471(74)90047-3*

Johns, W. E., Lee, T. N., Beardsley, R. C., Candela, J., Limeburner, R. and Castro, B. (1998), "Annual cycle and variability of the North Brazil current", *Journal of Physical Oceanography* **28**(1), 103–128.
doi: *10.1175/1520-0485(1998)028<0103:ACAVOT>2.0.CO;2*

Johnson, G. C. (1993), "A deep inertial jet on a sloping bottom near the equator", *Deep Sea Research Part I: Oceanographic Research Papers* **40**(9), 1781–1792.
doi: *10.1016/0967-0637(93)90032-X*

Johnson, H. L., Cessi, P., Marshall, D. P., Schloesser, F. and Spall, M. A. (2019), "Recent Contributions of Theory to Our Understanding of the Atlantic Meridional Overturning Circulation", *Journal of Geophysical Research: Oceans* **124**(8), 5376–5399.
doi: *10.1029/2019jc015330*

Josey, S. A., de Jong, M. F., Oltmanns, M., Moore, G. K. and Weller, R. A. (2019), "Extreme Variability in Irminger Sea Winter Heat Loss Revealed by Ocean Observatories Initiative Mooring and the ERA5 Reanalysis", *Geophysical Research Letters* **46**(1), 293–302.
doi: *10.1029/2018GL080956*

Joshi, M. (1994), Orographic Infliuences in the Atmosphere of Mars, PhD thesis, University of Oxford

Killworth, P. D. (1991), "Cross-equatorial Geostrophic Adjustment", *Journal of Physical Oceanography* **21**(10), 1581–1601.
doi: *10.1175/1520-0485(1991)021<1581:CEGA>2.0.CO;2*

Kloosterziel, R. C., Carnevale, G. F. and Orlandi, P. (2017), "Equatorial inertial instability with full Coriolis force", *Journal of Fluid Mechanics* **825**, 69–108.
doi: *10.1017/jfm.2017.377*

Lambert, R. B. and Sturges, W. (1977), "A thermohaline staircase and vertical mixing in the thermocline", *Deep Sea Research* **24**(3), 211–222.
doi: *10.1016/S0146-6291(77)80001-5*

Large, W. G., McWilliams, J. C. and Doney, S. C. (1994), "Oceanic vertical mixing: A review and a model with a nonlocal boundary layer parameterization", *Reviews of Geophysics* **32**(4), 363–403.
doi: *10.1029/94RG01872*

Le Bras, I. A. A., Callies, J., Straneo, F., Biló, T. C., Holte, J. and Johnson, H. L. (2022), "Slantwise Convection in the Irminger Sea", *Journal of Geophysical Research: Oceans* **127**(10), e2022JC019071.
doi: *10.1029/2022JC019071*

Little, C. M., Hu, A., Hughes, C. W., McCarthy, G. D., Piecuch, C. G., Ponte, R. M. and Thomas, M. D. (2019), "The Relationship Between U.S. East Coast Sea Level and the Atlantic Meridional Overturning Circulation: A Review", *Journal of Geophysical Research: Oceans* **124**(9), 6435–6458.
doi: *10.1029/2019JC015152*

Lozier, M. S., Li, F., Bacon, S., Bahr, F., Bower, A. S., Cunningham, S. A., de Jong, M. F., de Steur, L., deYoung, B., Fischer, J., Gary, S. F., Greenan, B. J. W., Holliday, N. P., Houk, A., Houpert, L., Inall, M. E., Johns, W. E., Johnson, H. L., Johnson, C., Karstensen, J., Koman, G., Le Bras, I. A., Lin, X., Mackay, N., Marshall, D. P., Mercier, H., Oltmanns, M., Pickart, R. S., Ramsey, A. L., Rayner, D., Straneo, F., Thierry, V., Torres, D. J., Williams, R. G., Wilson, C., Yang, J., Yashayaev, I. and Zhao, J. (2019), "A sea change in our view of overturning in the subpolar North Atlantic", *Science* **363**(6426), 516–521.
doi: *10.1126/science.aau6592*

Manfroi, A. J. and Young, W. R. (1999), "Slow evolution of zonal jets on the beta plane", *Journal of the Atmospheric Sciences* **56**(5), 784–800.
doi: *10.1175/1520-0469(1999)056<0784:SEOZJO>2.0.CO;2*

Marshall, D. P. and Pillar, H. R. (2011), "Momentum balance of the Wind-Driven and Meridional Overturning Circulation", *Journal of Physical Oceanography* **41**, 960–978.
doi: *10.1175/201*

Marshall, J., Adcroft, A., Hill, C., Perelman, L. and Heisey, C. (1997), "A finite-volume, incompressible navier stokes model for, studies of the ocean on parallel computers", *Journal of Geophysical Research: Oceans* **102**(C3), 5753–5766.
doi: *10.1029/96JC02775*

Marshall, J. and Schott, F. (1999), “Open-ocean convection: Observations, theory, and models”, *Reviews of Geophysics* **37**(1), 1–64.
doi: *10.1029/98RG02739*

Marshall, J. and Speer, K. (2012), “Closure of the meridional overturning circulation through Southern Ocean upwelling”, *Nature Geoscience* **5**(3), 171–180.
doi: *10.1038/ngeo1391*

Mashayek, A., Ferrari, R., Merrifield, S., Ledwell, J. R., St Laurent, L. and Garabato, A. N. (2017), “Topographic enhancement of vertical turbulent mixing in the Southern Ocean”, *Nature Communications* **8**(1), 14197.
doi: *10.1038/ncomms14197*

Matthew Rocklin (2015), Dask: Parallel Computation with Blocked algorithms and Task Scheduling, *in* K. Huff and James Bergstra, eds, “Proceedings of the 14th Python in Science Conference”, pp. 126–132.
doi: *10.25080/Majora-7b98e3ed-013*

McDougall, T. J. and Ferrari, R. (2017), “Abyssal Upwelling and Downwelling Driven by Near-Boundary Mixing”, *Journal of Physical Oceanography* **47**(2), 261–283.
doi: *10.1175/JPO-D-16-0082.1*

McWilliams, J. C. (2016), “Submesoscale currents in the ocean”, *Proceedings of the Royal Society A: Mathematical, Physical and Engineering Sciences* **472**(2189).
doi: *10.1098/rspa.2016.0117*

Melling, H., Lake, R., Topham, D. and Fissel, D. (1984), “Oceanic thermal structure in the western Canadian Arctic”, *Continental Shelf Research* **3**(3), 233–258.
doi: *10.1016/0278-4343(84)90010-4*

Merryfield, W. J. (2000), “Origin of Thermohaline Staircases”, *Journal of Physical Oceanography* **30**(5), 1046–1068.
doi: *10.1175/1520-0485(2000)030<1046:OOTS>2.0.CO;2*

Miles, A., Kirkham, J., Bussonnier, M., Moore, J., Fulton, A., Orfanos, D. P., Bourbeau, J., Lee, G., Patel, Z., Bennett, D., Rocklin, M., Abernathey, R., de Andrade, E. S., Durant, M., Schut, V., Dussin, R., Kristensen, M. R. B., Chaudhary, S., Barnes, C., Nunez-Iglesias, J., Williams, B., Mohar, B., Noyes, C., Bell, R., Zhang, H., shikharsg and Jelenak, A. (2022), “Zarr-developers/zarr-python: V2.13.0a2”. Software, published on *zenodo*.
doi: *10.5281/zenodo.7060059*

Moore, G. W. K., Pickart, R. S. and Renfrew, I. A. (2008), “Buoy observations from the windiest location in the world ocean, Cape Farewell, Greenland”, *Geophysical Research Letters* **35**(18).
doi: *10.1029/2008GL034845*

Morel, Y., Gula, J. and Ponte, A. (2019), “Potential vorticity diagnostics based on balances between volume integral and boundary conditions”, *Ocean Modelling* **138**, 23–35.
doi: *10.1016/j.ocemod.2019.04.004*

Muller, P., McWilliams, J. and Molemaker, J. (2005), Routes to Dissipation in the Ocean: The 2D/3D Turbulence Conundrum, *in* H. Baumert, J. Simpson and J. Sündermann, eds, “Marine Turbulence: Theories, Observations, and Models”, Cambridge University Press, Cambridge, pp. 397–405

Munk, W. H. (1966), “Abyssal recipes”, *Deep Sea Research and Oceanographic Abstracts* **13**(4), 707–730.
doi: *10.1016/0011-7471(66)90602-4*

Munk, W. and Wunsch, C. (1998), "Abyssal recipes II: Energetics of tidal and wind mixing", *Deep Sea Research Part I: Oceanographic Research Papers* **45**(12), 1977–2010.
doi: *10.1016/S0967-0637(98)00070-3*

Nof, D. (1990), "Why are some boundary currents blocked by the equator?", *Deep Sea Research Part A. Oceanographic Research Papers* **37**(5), 853–873.
doi: *10.1016/0198-0149(90)90010-S*

Nof, D. (1996), "Why are rings regularly shed in the western equatorial Atlantic but not in the western Pacific?", *Progress in Oceanography* **38**(4), 417–451.
doi: *10.1016/S0079-6611(97)00004-9*

Nof, D. and Pichevin, T. (1996), "The retroflection paradox", *Journal of Physical Oceanography* **26**(11), 2344–2358.
doi: *10.1175/1520-0485(1996)026<2344:TRP>2.0.CO;2*

Ooyama, K. (1966), "On the Stability of the Baroclinic Circular Vortex: A Sufficient Criterion for Instability", *Journal of the Atmospheric Sciences* **23**(1), 43–53.
doi: *10.1175/1520-0469(1966)023<0043:OTSOTB>2.0.CO;2*

Ozmidov, R. (1965), "On the turbulent exchange in a stably stratified ocean.", *Izvestiya Academy of Sciences USSR Atmospheric and Oceanic Physics* **1**, 861–871

Pickart, R. S., Spall, M. A., Ribergaard, M. H., Moore, G. W. K. and Milliff, R. F. (2003), "Deep convection in the Irminger Sea forced by the Greenland tip jet", *Nature* **424**(6945), 152–156.
doi: *10.1038/nature01729*

Plougonven, R. and Zeitlin, V. (2009), "Nonlinear development of inertial instability in a barotropic shear", *Physics of Fluids* **21**(10).
doi: *10.1063/1.3242283*

Prather, M. J. (1986), “Numerical advection by conservation of second-order moments”, *Journal of Geophysical Research: Atmospheres* **91**(D6), 6671.
doi: *10.1029/JD091iD06p06671*

Rahmstorf, S. and Ganopolski, A. (1999), “Long-term global warming scenarios computed with an efficient coupled climate model”, *Climatic Change* **43**(2), 353–367.
doi: *10.1023/A:1005474526406*

Rhein, M., Stramma, L. and Sond, U. (1995), “The Atlantic Deep Western Boundary Current: Water masses and transports near the equator”, *Journal of Geophysical Research: Oceans* **100**(C2), 2441–2457.
doi: *10.1029/94JC02355*

Ribstein, B., Zeitlin, V. and Tissier, A. S. (2014), “Barotropic, baroclinic, and inertial instabilities of the easterly Gaussian jet on the equatorial β-plane in rotating shallow water model”, *Physics of Fluids* **26**(5).
doi: *10.1063/1.4875030*

Richardson, P. L. and Fratantoni, D. M. (1999), “Float trajectories in the deep western boundary current and deep equatorial jets of the tropical Atlantic”, *Deep Sea Research Part II: Topical Studies in Oceanography* **46**(1-2), 305–333.
doi: *10.1016/S0967-0645(98)00100-3*

Rodwell, M. J. and Hoskins, B. J. (1995), “A Model of the Asian Summer Monsoon.Part II: Cross-Equatorial Flow and PV Behavior”, *Journal of the Atmospheric Sciences* **52**(9), 1341–1356.
doi: *10.1175/1520-0469(1995)052<1341:AMOTAS>2.0.CO;2*

Schmitt, R. W., Ledwell, J. R., Montgomery, E. T., Polzin, K. L. and Toole, J. M. (2005), "Enhanced diapycnal mixing by salt fingers in the thermocline of the tropical atlantic", *Science* **308**(5722), 685–688.
doi: *10.1126/science.1108678*

Schmitt, R. W., Perkins, H., Boyd, J. D. and Stalcup, M. C. (1987), "C-SALT: An investigation of the thermohaline staircase in the western tropical North Atlantic", *Deep Sea Research Part A. Oceanographic Research Papers* **34**(10), 1655–1665.
doi: *10.1016/0198-0149(87)90014-8*

Schott, F. A., Dengler, M., Zantopp, R., Stramma, L., Fischer, J. and Brandt, P. (2005), "The shallow and deep western boundary circulation of the South Atlantic at 5°-11°S", *Journal of Physical Oceanography* **35**(11), 2031–2053.
doi: *10.1175/JPO2813.1*

Schott, F., Fischer, J., Reppin, J. and Send, U. (1993), "On mean and seasonal currents and transports at the western boundary of the equatorial Atlantic", *Journal of Geophysical Research: Oceans* **98**(C8).
doi: *10.1029/93jc01287*

Simoes-Sousa, I. T., Silveira, I. C. A., Tandon, A. and Flierl, G. R. (2021), "The Barreirinhas Eddies: Stable Energetic Anticyclones in the Near-Equatorial South Atlantic", *Frontiers in Marine Science* **8**.
doi: *10.3389/fmars.2021.617011*

Smagorinsky, J. (1963), "General circulation experiments with the primitive equations", *Monthly Weather Review* **91**(3), 99–164.
doi: *10.1175/1520-0493(1963)091<0099:GCEWTP>2.3.CO;2*

Spall, M. A. and Thomas, L. N. (2016), “Downfront Winds over Buoyant Coastal Plumes”, *Journal of Physical Oceanography* **46**(10), 3139–3154.
doi: *10.1175/JPO-D-16-0042.1*

Spingys, C. P., Garabato, A. C. N., Legg, S., Polzin, K. L., Abrahamsen, E. P., Buckingham, C. E., Forryan, A. and Frajka-Williams, E. E. (2021), “Mixing and Transformation in a Deep Western Boundary Current: A Case Study”, *Journal of Physical Oceanography* **51**(4), 1205–1222.
doi: *10.1175/JPO-D-20-0132.1*

Srokosz, M., Baringer, M., Bryden, H., Cunningham, S., Delworth, T., Lozier, S., Marotzke, J. and Sutton, R. (2012), “Past, present, and future changes in the atlantic meridional overturning circulation”, *Bulletin of the American Meteorological Society* **93**(11), 1663–1676.
doi: *10.1175/BAMS-D-11-00151.1*

Stamper, M. A. and Taylor, J. R. (2017), “The transition from symmetric to baroclinic instability in the Eady model”, *Ocean Dynamics* **67**(1), 65–80.
doi: *10.1007/s10236-016-1011-6*

Stern, M. E. (1960), “The “Salt-Fountain” and Thermohaline Convection”, *Tellus* **12**(2), 172–175.
doi: *10.3402/tellusa.v12i2.9378*

Stewart, A. L. and Dellar, P. J. (2011), “The rôle of the complete Coriolis force in cross-equatorial flow of abyssal ocean currents”, *Ocean Modelling* **38**(3-4), 187–202.
doi: *10.1016/j.ocemod.2011.03.001*

Stone, P. H. (1966), “On Non-Geostrophic Baroclinic Stability”, *Journal of the Atmospheric Sciences* **23**(4), 390–400.
doi: *10.1175/1520-0469(1966)023<0390:ONGBS>2.0.CO;2*

Straneo, F., Kawase, M. and Pickart, R. S. (2002), “Effects of Wind on Convection in Strongly and Weakly Baroclinic Flows with Application to the Labrador Sea”, *Journal of Physical Oceanography* **32**(9), 2603–2618.
doi: *10.1175/1520-0485(2002)032<2603:EOWOCI>2.0.CO;2*

Tait, R. and Howe, M. (1968), “Some observations of thermo-haline stratification in the deep ocean”, *Deep Sea Research and Oceanographic Abstracts* **15**(3), 275–280.
doi: *10.1016/0011-7471(68)90005-3*

Talley, L. D., Pickard, G. L., Emery, W. J. and Swift, J. H. (2011*a*), Chapter 12 - Arctic Ocean and Nordic Seas, *in* L. D. Talley, G. L. Pickard, W. J. Emery and J. H. Swift, eds, “Descriptive Physical Oceanography (Sixth Edition)”, Academic Press, Boston, pp. 401–436.
doi: *10.1016/B978-0-7506-4552-2.10012-5*

Talley, L. D., Pickard, G. L., Emery, W. J. and Swift, J. H. (2011*b*), Chapter 9 - Atlantic Ocean, *in* L. D. Talley, G. L. Pickard, W. J. Emery and J. H. Swift, eds, “Descriptive Physical Oceanography (Sixth Edition)”, Academic Press, Boston, pp. 245–301.
doi: *10.1016/B978-0-7506-4552-2.10009-5*

Taylor, J. R., Bachman, S., Stamper, M., Hosegood, P., Adams, K., Sallee, J.-B. and Torres, R. (2018), “Submesoscale rossby waves on the antarctic circumpolar current”, *Science Advances* **4**(3), eaao2824.
doi: *10.1126/sciadv.aao2824*

Taylor, J. R. and Ferrari, R. (2009), "On the equilibration of a symmetrically unstable front via a secondary shear instability", *Journal of Fluid Mechanics* **622**, 103–113.
doi: *10.1017/S0022112008005272*

Taylor, J. R. and Ferrari, R. (2010), "Buoyancy and Wind-Driven Convection at Mixed Layer Density Fronts", *Journal of Physical Oceanography* **40**(6), 1222–1242.
doi: *10.1175/2010JPO4365.1*

Thomas, L. N. and Lee, C. M. (2005), "Intensification of ocean fronts by down-front winds", *Journal of Physical Oceanography* **35**(6), 1086–1102.
doi: *10.1175/JPO2737.1*

Thomas, L. N., Tandon, A. and Mahadevan, A. (2008), Submesoscale processes and dynamics, *in* M. W. Hecht and H. Hasumi, eds, "Ocean Modeling in an Eddying Regime", Vol. 177 of *Geophysical Monograph Series*, American Geophysical Union, Washington, D. C., pp. 17–38.
doi: *10.1029/177GM04*

Thomas, L. N., Taylor, J. R., Ferrari, R. and Joyce, T. M. (2013), "Symmetric instability in the Gulf Stream", *Deep Sea Research Part II: Topical Studies in Oceanography* **91**, 96–110.
doi: *10.1016/j.dsr2.2013.02.025*

Uchida, T., Le Sommer, J., Stern, C., Abernathey, R. P., Holdgraf, C., Albert, A., Brodeau, L., Chassignet, E. P., Xu, X., Gula, J., Roullet, G., Koldunov, N., Danilov, S., Wang, Q., Menemenlis, D., Bricaud, C., Arbic, B. K., Shriver, J. F., Qiao, F., Xiao, B., Biastoch, A., Schubert, R., Fox-Kemper, B., Dewar, W. K. and Wallcraft, A. (2022), "Cloud-based framework for inter-comparing submesoscale-permitting realistic ocean models", *Geoscientific Model Development* **15**(14), 5829–5856.
doi: *10.5194/gmd-15-5829-2022*

Vianna, M. and de Menezes, V. (2003), A seasonal and interannual study of the western equatorial Atlantic upper thermocline circulation variability, *in* "Interhemispheric Water Exchange in the Atlantic Ocean", 1st ed. ed., Vol. 68 of *Elsevier Oceanography Series*, Elsevier, Amsterdam, pp. 137–173.
doi: *10.1016/S0422-9894(03)80145-9*

Virtanen, P., Gommers, R., Oliphant, T. E., Haberland, M., Reddy, T., Cournapeau, D., Burovski, E., Peterson, P., Weckesser, W., Bright, J., van der Walt, S. J., Brett, M., Wilson, J., Millman, K. J., Mayorov, N., Nelson, A. R. J., Jones, E., Kern, R., Larson, E., Carey, C. J., Polat, İ., Feng, Y., Moore, E. W., VanderPlas, J., Laxalde, D., Perktold, J., Cimrman, R., Henriksen, I., Quintero, E. A., Harris, C. R., Archibald, A. M., Ribeiro, A. H., Pedregosa, F., van Mulbregt, P. and SciPy 1.0 Contributors (2020), "SciPy 1.0: Fundamental algorithms for scientific computing in python", *Nature Methods* **17**, 261–272.
doi: *10.1038/s41592-019-0686-2*

Walin, G. (1982), "On the relation between sea-surface heat flow and thermal circulation in the ocean", *Tellus* **34**(2), 187–195.
doi: *10.3402/tellusa.v34i2.10801*

Weatherly, G. L. and Martin, P. J. (1978), “On the structure and dynamics of the oceanic bottom boundary layer”, *Journal of Physical Oceanography* **8**(4), 557–570.
doi: *10.1175/1520-0485(1978)008<0557:OTSADO>2.0.CO;2*

Weijer, W., Cheng, W., Drijfhout, S. S., Fedorov, A. V., Hu, A., Jackson, L. C., Liu, W., McDonagh, E. L., Mecking, J. V. and Zhang, J. (2019), “Stability of the Atlantic Meridional Overturning Circulation: A Review and Synthesis”, *Journal of Geophysical Research: Oceans* **124**(8), 5336–5375.
doi: *10.1029/2019JC015083*

Wenegrat, J. O. and Thomas, L. N. (2020), “Centrifugal and symmetric instability during Ekman adjustment of the bottom boundary layer”, *Journal of Physical Oceanography* **50**(6), 1793–1812.
doi: *10.1175/JPO-D-20-0027.1*

Williams, R. G. and Follows, M. J. (2011), Integral Frameworks, *in* “Ocean Dynamics and the Carbon Cycle”, Cambridge University Press, Cambridge, pp. 329–353.
doi: *10.1017/CBO9780511977817.014*

Xu, Q. and Clark, J. H. E. (1985), “The Nature of Symmetric Instability and Its Similarity to Convective and Inertial Instability”, *Journal of the Atmospheric Sciences* **42**(24), 2880–2883.
doi: *10.1175/1520-0469(1985)042<2880:TNOSIA>2.0.CO;2*

Yankovsky, E. and Legg, S. (2019), “Symmetric and baroclinic instability in dense shelf overflows”, *Journal of Physical Oceanography* **49**(1), 39–61.
doi: *10.1175/JPO-D-18-0072.1*

Yankovsky, E., Legg, S. and Hallberg, R. (2021), "Parameterization of Submesoscale Symmetric Instability in Dense Flows Along Topography", *Journal of Advances in Modeling Earth Systems* **13**(6), 1–28.
doi: *10.1029/2020MS002264*

Yu, X., Garabato, A. C. N., Martin, A. P. and Marshall, D. P. (2021), "The Annual Cycle of Upper-Ocean Potential Vorticity and Its Relationship to Submesoscale Instabilities", *Journal of Physical Oceanography* **51**(2), 385–402.
doi: *10.1175/JPO-D-20-0099.1*

Yu, X., Naveira Garabato, A. C., Martin, A. P., Gwyn Evans, D. and Su, Z. (2019), "Wind-Forced Symmetric Instability at a Transient Mid-Ocean Front", *Geophysical Research Letters* **46**(20), 11281–11291.
doi: *10.1029/2019GL084309*

Zeitlin, V. (2018), "Letter: Symmetric instability drastically changes upon inclusion of the full Coriolis force", *Physics of Fluids* **30**(6), 061701.
doi: *10.1063/1.5031099*

Zhang, D., Msadek, R., McPhaden, M. J. and Delworth, T. (2011), "Multidecadal variability of the North Brazil Current and its connection to the Atlantic meridional overturning circulation", *Journal of Geophysical Research: Oceans* **116**(C4), 1–9.
doi: *10.1029/2010jc006812*

Zhang, R. and Delworth, T. L. (2005), "Simulated tropical response to a substantial weakening of the Atlantic thermohaline circulation", *Journal of Climate* **18**(12), 1853–1860.
doi: *10.1175/JCLI3460.1*

Zhang, R., Sutton, R., Danabasoglu, G., Kwon, Y. O., Marsh, R., Yeager, S. G., Amrhein, D. E. and Little, C. M. (2019), "A Review of the Role of the Atlantic Meridional Overturning Circulation in Atlantic Multidecadal Variability and Associated Climate Impacts", *Reviews of Geophysics* **57**(2), 316–375.
doi: *10.1029/2019RG000644*

Zharkov, V. and Nof, D. (2010), "Why does the north brazil current regularly shed rings but the brazil current does not?", *Journal of Physical Oceanography* **40**(2), 354–367.
doi: *10.1175/2009JPO4246.1*

Zhou, H., Dewar, W., Yang, W., Liu, H., Chen, X., Li, R., Liu, C. and Gopalakrishnan, G. (2022), "Observations and modeling of symmetric instability in the ocean interior in the Northwestern Equatorial Pacific", *Communications Earth & Environment* **3**(1).
doi: *10.1038/s43247-022-00362-4*